

ISTANBUL TECHNICAL UNIVERSITY ★ GRADUATE SCHOOL OF SCIENCE
ENGINEERING AND TECHNOLOGY

**DEVELOPMENT OF POROUS CERAMICS FOR WASTEWATER
PURIFICATION**



Ph.D. THESIS

Damla ZEYDANLI

Department of Chemistry
Chemistry Programme

MAY 2019

ISTANBUL TECHNICAL UNIVERSITY ★ GRADUATE SCHOOL OF SCIENCE
ENGINEERING AND TECHNOLOGY

**DEVELOPMENT OF POROUS CERAMICS FOR WASTEWATER
PURIFICATION**



Ph.D. THESIS
Damla ZEYDANLI
(509122013)

Department of Chemistry
Chemistry Programme

Thesis Advisor: Prof. Dr. Süleyman AKMAN
Co-adviser: Assoc. Prof. Dr. Çekdar Vakıf AHMETOĞLU

MAY 2019

İSTANBUL TEKNİK ÜNİVERSİTESİ ★ FEN BİLİMLERİ ENSTİTÜSÜ

**ATIK SU FİLTRELENMESİ İÇİN GÖZENEKLİ SERAMİKLERİN
GELİŞTİRİLMESİ**

**DOKTORA TEZİ
Damla ZEYDANLI
(509122013)**

**Kimya Anabilim Dalı
Kimya Programı**

**Tez Danışmanı: Prof. Dr. Süleyman AKMAN
Eş Danışman: Doç. Dr. Çekdar Vakıf AHMETOĞLU**

MAYIS 2019

Damla Zeydanlı, a Ph.D. student of İTÜ Graduate School of Science Engineering and Technology student ID 509122013, successfully defended the dissertation entitled “DEVELOPMENT OF POROUS CERAMICS FOR WASTE WATER PURIFICATION”, which she prepared after fulfilling the requirements specified in the associated legislations, before the jury whose signatures are below.

Thesis Advisor : **Prof. Dr. Süleyman AKMAN**
İstanbul Technical University

Co-advisor : **Assoc. Prof.Dr. Çekdar V. AHMETOĞLU**
İzmir Institute of Technology

Jury Members : **Prof. Dr. Mustafa ÖZCAN**
İstanbul Technical University

Prof. Dr. Birsen ÖZTÜRK
İstanbul Technical University

Dr. Ferah ÇALIŞIR
İstanbul Technical University

Assoc. Prof. Dr. Aslı BAYSAL
İstanbul Aydın University

Prof. Dr. Dilek BAKIRCIOĞLU
Trakya University



FOREWORD

I would like to express my gratitude to my advisors Prof. Dr. Süleyman AKMAN and Assoc. Prof. Dr. Çekdar Vakıf AHMETOĞLU. Their valuable insights and supports gave me vital guidance to complete the research and write this thesis. I will never forget what a great chance it is for me to work with them. I would also like to thank my committee members, Prof. Dr. Mustafa ÖZCAN, Prof. Dr. Birsen ÖZTÜRK and Assoc. Prof. Dr. Aslı BAYSAL for their brilliant comments and suggestions.

I am extremely grateful to my dear friends Hande TINAS, Deniz KAVRAR and Kübra İLGÜN for their understanding even when it was an impossible job to cheer me up or even bear with me. I should express my appreciations to my colleagues Dr. Nil ÖZBEK, Serter LÜLEBURGAZ and Zeynep KALAYCIOĞLU for their kind support.

I owe to my family exclusive thanks. Words cannot express how much I am grateful and thank you all for your steady support. I am grateful for my father Ahmet ZEYDANLI's endless trust and strong presence, for my mother Nurdan DEMİRER to unrequited love. I would like to thank my sister Ferda ZEYDANLI and my brother Uğur ZEYDANLI for being a great support in most difficult and important moments during this thesis process. I would also like to thank my aunts Meriç Aydın and Zülal ZEYDANLI for backing me up every time I need. To my other family members Melodi AYDIN, Demet KARABACAK, Hüma ÜLGEN and Kocaman I am thankful for your valuable patience and love. A special thank you to my nephew, Alp ZEYDANLI for his beautiful energy and joy.

March 2019

Damla ZEYDANLI
(Chemist)



TABLE OF CONTENTS

	<u>Page</u>
FOREWORD	vii
TABLE OF CONTENTS	ix
ABBREVIATIONS	xi
LIST OF TABLES	xiii
LIST OF FIGURES	xv
SUMMARY	xix
OZET	xxi
1. INTRODUCTION	1
2. EXPERIMENTAL	5
2.1 Materials and Method	5
2.1.1 Reagents.....	5
2.1.2 Instruments.....	6
2.2 Manufacture of SiOC	7
2.2.1 Porous SiOC foams.....	7
2.2.2 SiOC beads.....	7
2.2.2.1 ‘Oil-in-water’ emulsion	8
2.2.2.2 ‘Water-in-oil-in-water’ emulsion.....	8
2.2.3 HF etching of SiOC	9
2.3 Manufacture of CSH/CS	9
2.3.1 CSH powder.....	9
2.3.2 CS/CSH monolith	13
2.3.2.1 Gelation.....	13
2.3.2.2 HAPES.....	14
2.4 Zeolite Coating.....	15
2.4.1 Zeolite coating of CSH	16
2.4.2 Zeolite coating of SiOC	16
2.5 Removal of Pollutants from Aqueous Solution	17
2.5.1 Batch adsorption	17
2.5.2 Maximum adsorption capacities	17
2.5.2.1 Metals.....	18
2.5.2.2 Dyes	19
2.5.3 Dye mixture	20
2.5.4 Regeneration of SiOC	20
2.5.5 Industrial wastewater	20
2.5.6 Characterization of saturated SiOC	21
3. RESULTS	23
3.1 Characterization of SiOC	23
3.1.1 SiOC foams.....	23
3.1.2 SiOC beads.....	30

3.2 Characterization CSH/CS	32
3.2.1 CSH powder.....	32
3.2.2 Monolithic CSH/CS.....	42
3.2.2.1 Gelation.....	42
3.2.2.2 HAPES.....	43
3.3 Characterization of Zeolite Coated Samples.....	46
3.3.1 Characterization of zeolite coated CSH/CH	46
3.3.2 Characterixation of zeolite coated SiOC.....	49
3.4 Removal of Pollutants from Aqueous Solution	53
3.4.1 Removal of dyes	53
3.4.1.1 Regeneration of SiOC.....	56
3.4.1.2 Adsorption of dye mixture.....	58
3.4.1.3 Characterization of the saturated SiOC.....	59
3.4.2 Removal of metals	62
3.4.3 Industrial wastewater purification.....	65
4. DISCUSSION	67
4.1 Silicon Oxy-Carbide Samples.....	67
4.2 Calcium Silicate Samples	67
4.3 Adsorption Studies.....	67
4.4 Regeneration	70
4.5 Industrial Wastewater	70
5. CONCLUSION AND RECOMMENDATIONS.....	73
REFERENCES.....	75
CURRICULUM VITAE.....	83

ABBREVIATIONS

AAS	: Atomic Absorption Spectroscopy
BET	: Brunauer-Emmet-Teller Technique
CS	: Calcium-silicate
CSH	: Calcium-silicate-hydrate
CT	: Computed Tomography
CV	: Crystal Violet
DABCO	: Diazobicyclo octane
DI	: Deionized
FT-IR	: Fourier Transform-Infrared Spectroscopy
HAPES	: High Alkane Phase Emulsified Suspensions
HF	: Hydrofluoric
Hg-por.	: Mercury Porosimetry
HZC-PDC	: Hydrothermal Zeolite Coating-Polymer Derived Ceramic
HZC-XT	: Hydrothermal Zeolite Coating-Xonotlite
LDH	: Hydrotalcite
MB	: Methylene Blue
Na-Alg	: Sodium-Alginate
NMR	: Nuclear Magnetic Resonance
PDMS	: Poly-dimethyl-siloxane
PHMS	: Poly-methylhydrosiloxane
PVA	: Polyvinyl alcohol
RB	: Rhodamine B
SEM/EDX	: Scanning Electron Microscope/Energy Dispersive X-ray
SiOC	: Silicon-oxy-carbide
SLS	: Sodium lauryl sulphate
SSA	: Specific surface area
TEOS	: Tetraethyl orthosilicate
TGA	: Thermogravimetric Analysis
TMTVS	: Tetra methyl tetravinly cyclotetrasiloxane
TPAOH	: Tetrapropylammonium hydroxide
Tween-20	: Poly-oxyethylene sorbitan monolaurate
UV-Vis	: UltraViolet-Visible Spectroscopy
XRD	: X-Ray Diffractometer



LIST OF TABLES

	<u>Page</u>
Table 2.1 : Quantities of chemicals used in the production of L series samples.	7
Table 2.2 : Details for thermoset siloxane beads samples produced with O/W emulsion method.	8
Table 2.3 : Details for thermoset siloxane beads samples produced with W/O/W emulsion method.	9
Table 2.4 : The detail of recycled glass.	10
Table 2.5 : Details of the process used to produce CSH powders.	11
Table 2.6 : The amount of chemicals used for the monolith ‘Alginate’ samples produced by the gelation method.	13
Table 2.7 : The amount of chemicals used for the monolith ‘HAPES’ samples.	14
Table 2.8 : Details of the process used to produce HZC-XT samples.	16
Table 2.9 : Details of the process used to produce HZC-PDC samples.	17
Table 3.1 : Chemical shift peaks of the sample L1 and L3.	24
Table 3.2 : Data before and after pyrolysis in L series samples.	25
Table 3.3 : The N ₂ adsorption test results of SiOC samples.	29
Table 3.4 : The results of mercury porosimetry of zeolite coated sample CSH.	46
Table 3.5 : The N ₂ ads./des. results of commercial CSH and HZC-XT samples.	48
Table 3.6 : N ₂ ads./des. results of samples HZC-PDC and their substrates.	50
Table 3.7 : Pore character information of HZC-PDC samples and substrates measured by mercury porosimetry.	52
Table 3.8 : Results of Langmuir and Freundlich isotherms for all samples.	56
Table 3.9 : The results of regeneration studies with heat treatment (400 °C) and EtOH.	57
Table 3.10 : Adsorption percentage of the mixture of three dyes onto sample L3-HF at different contact time.	58
Table 3.11 : The elemental ratio from the EDX analysis of L3HF and after the dye loaded the same sample.	61
Table 3.12 : The results of Langmuir and Freundlich isotherms for all samples	65
Table 3.13 : Adsorption of pollutant tested onto L3HF from actual wastewater.	66
Table 4.1 : Comparison of samples produced and common adsorbent material studied in the literature.	68
Table 4.2 : Comparison of samples produced and common adsorbent material studied in the literature.	69



LIST OF FIGURES

	<u>Page</u>
Figure 2.1 : a) ball mill mortar used to grind recycling glass, b) various sieves and sieved recycling glasses.....	10
Figure 2.2 : a and b) Preparing HAPES samples with using the overhead stirrer, c) images of moulded and green HAPES sample.....	15
Figure 2.3 : Static autoclave systems.....	15
Figure 2.4 : Structure of the a) MB, b) CV, and c) RB.	19
Figure 3.1 : Digital photographs from a) the bottom side of the thermoset, b) the upper side of the thermoset c) the bottom side of the pyrolyzed, and d) the upper side of the pyrolyzed sample L1.....	23
Figure 3.2 : ²⁹ Si MAS-NMR spectra of L1 and L3.	24
Figure 3.3 : SEM images of, a) pores from the upper side, b) cross section of channels c) channel strut, d) surface detail, and d) higher magnification of pore surface of the pyrolyzed L1 sample	25
Figure 3.4 : Tomographic 2D images of radial (R)and (A) slices at the top,center and bottom of L1,L2 and L3samples.	26
Figure 3.5 : Pore diameter distributions of radial tomographic slices of L3 sample.....	27
Figure 3.6 : Average channel diameters from the top, centre and bottom of samples L1-L3.....	28
Figure 3.7 : Mercury porosimetry results of the SiOC samples.	28
Figure 3.8 : Samples L1-L3 a) N ₂ adsorption/desorption isotherms and b) pore size distribution curves.	29
Figure 3.9 : The SEM images of sample L1 a) before and b) after HF etching.	30
Figure 3.10 : a) The optical microscope image (100 μm scale), b) SEM image of non-porous beads produced by o/w emulsion method.	30
Figure 3.11 : SEM images are taken from SiOC bead sample a-b) before the etching and c-d) after the etching.....	31
Figure 3.12 : SiOC bead samples produced with W/O/W method (before and after etching) a) XRD, b) FT-IR and, c) RAMAN results.	32
Figure 3.13 : XRD plots of the samples produced a) without ball mill b) with ball mill 10h/250 rpm.	33
Figure 3.14 : a) TG and b) DTA plots of XRG41 and XRG42.....	33
Figure 3.15 : a) TG and b) DTA plots of XRG43-44.....	34
Figure 3.16 : a) TG and b) DTA plots of XRG71-74.....	34
Figure 3.17 : SEM images of sample XRG41 with different magnifications.....	35
Figure 3.18 : SEM images of sample XRG42 with different magnifications.....	36
Figure 3.19 : SEM images of sample XRG43, a) low magnification, b) and c) higher magnification, d) flake-like structure detail.	36
Figure 3.20 : SEM images of sample XRG44, a) low magnification, b) and c) higher magnification, d) flake-like structure detail.	37
Figure 3.21 : SEM images of sample XRG71, a) low magnification, b) and c) higher magnification, d) EDS results from agglomerate and fibre structure. ...	38

Figure 3.22 : SEM images of sample XRG72, a) low magnification, b and c) higher magnification, d) EDS results from flake-like and thin lath structures..	39
Figure 3.23 : SEM images of sample XRG73, a) low magnification, b and c) higher magnification, d) EDS results from laths structure.	40
Figure 3.24 : SEM images of sample XRG74, a) low magnification, b and c) higher magnification, d) EDS results from pellet and thin lath structures.	41
Figure 3.25 : SEM image of samples produced with XRG71 a) Alginate1, b) Alginate2.	42
Figure 3.26 : SEM micrograph images from HAPES71-72, a) low magnification from green HAPES71 (produced with XRG71), b) higher magnification image taken from the same sample after heat treatment at 1000 °C, c) low magnification from HAPES72 (produced with XRG72), d) higher magnification from the same sample, e) low magnification image taken from the HAPES72 after heat treatment at 1000 °C and f) higher magnification from the same sample.....	43
Figure 3.27 : SEM images of commercial Xonotlite powder, a) general view, b) higher magnification of pellets c) and d) higher magnification of acicular structure.	44
Figure 3.28 : SEM images from the 25% HAPES sample made by using commercial CSH (Xonotlite) a) general view, b) detail of pores.	44
Figure 3.29 : SEM images from the 25% HAPES sample made by using commercial CSH (Xonotlite) powder after the heat treatment a) general view, b) from hallow, c) details of pores.	45
Figure 3.30 : SEM images of 35% solid loading HAPES sample made by using commercial CSH (xonotlite) a) general view, b) pore detail.	45
Figure 3.31 : The PSD curves results of commercial Xonotlite and sample HZC-XT-1 from the mercury porosimeter.	46
Figure 3.32 : The SEM images of sample HZC-XT-1(3 days reax. time) a) general view, b) higher magnification from the pellet, c, and d) the detail of zeolite crystals from the gap of between CSH particle	47
Figure 3.33 : The N ₂ adsorption/desorption isotherms curves from the commercial CSH and HZC-XT samples.	48
Figure 3.34 : SEM images of HZC-PDC-7 sample obtained by 3-day hydrothermal reaction using L1 sample as substrate a) general view b) higher magnification.	49
Figure 3.35 : a) The N ₂ adsorption/desorption isotherms and b) pore size distribution graphs of all HZC-PDC samples.....	51
Figure 3.36 : PSD curves of HZC-PDC-1,3,7,8 and L1-3 samples, plotted using results from the mercury porosimeter.....	52
Figure 3.37 : The retention graphs at different pH values, (a) L1 ve L3, MB, (b) L3, RB ve (c) L3, CV.....	53
Figure 3.38 : MB, CV, RB adsorption for samples; a) L1 and L1HF, (b) L3 and L3HF.....	54
Figure 3.39 : The adsorption capacities of the sample a) HZC-XT-3 and Xonotlite (commercial CSH) b) HZC-PDC and its substrate L3, and c) Alginate1.	55
Figure 3.40 : The re-sorption yield for sample L3HF.....	57
Figure 3.41 : The decolourization of three dyes mixture after 1-24 h contact time with sample L3-HF.....	58

Figure 3.42 : FTIR data of a) pure MB, CV and RB molecules, b) etched SiOC sample and after the dye loaded of sample.....	59
Figure 3.43 : a) The SEM and TEM figure of L3HF sample before the loaded with dye, the SEM images of L3HF loaded with b) MB, c) RB and, d) CV.	60
Figure 3.44 : The EDX results from the a) sample L3HF, b) MB loaded L3HF.	60
Figure 3.45 : L3HF sample before and after dye adsorption, a) N ₂ adsorption/desorption isotherms, b) pore size distribution graph.	61
Figure 3.46 : The retention percentage graphs taken at different pH values for samples, (a) L1, (b) L2, and (c) L3.	62
Figure 3.47 : Adsorption results for, a) L1 and L1HF b) L2 and L2HF (Cd(II), and Zn(II)), c) L3, d) L3HF samples (Cd(II), Zn(II), Cr(III), Pb(II), and Cu(II))......	63
Figure 3.48 : Adsorption results of the sample a) HZC-XT-3 and xonotlite (commercial CSH) and b) HZC-PDC and its substrate L3	63
Figure 3.49 : Adsorption results for Alginate 1.	64



DEVELOPMENT OF POROUS CERAMICS FOR WASTEWATER PURIFICATION

SUMMARY

In this thesis, ceramics with macro pores were produced, then the structure was transformed into a hierarchical structure containing both macro and micro/meso porosity by zeolite coating or hydrofluoric acid etching. The final material was tested for removing some pollutants from water.

The ceramics produced can be examined in two groups; silicon-oxy-carbide (SiOC) samples and calcium-silicate (CS). SiOC foam samples were produced using a mixture of three pre-ceramic polymers and a catalyst. These samples have axial-oriented channels using a simple one-way heat source for curing step. Another type of SiOC samples were also produced with pre-ceramic polymers via emulsion methods. Micron sized non-porous and macro-porous bead-shaped SiOC ceramics were obtained by using two or three phase emulsion methods. For the formation of CS ceramic samples, primarily calcium-silicate-hydrate (CSH) powders with different Ca/Si molar ratios was produced by using lime hydrate and recycled glass via hydrothermal reaction. Synthesized CSH powders with different crystal structures were used to produce porous monolithic structures.

The produced systems were characterized first by structural methods (X-Ray Diffractometer (XRD), Thermogravimetric Analysis (TGA), Fourier Transform-Infrared Spectroscopy (FT-IR), and Raman Spectroscopy (RAMAN)), then by scanning electron microscopy (SEM) for microstructure. Tomographic techniques (Computed Tomography, CT), mercury porosimetry (Hg-por.), and Brunauer-Emmet-Teller Technique (BET) were used for pore size, character and surface area determination. Following the manufacturing and characterization steps, the performance of the selected samples was evaluated for the removal of various pollutants (Cadmium, Copper, Zinc, Lead, Chromium, Methylene Blue, Rhodamine B, and Crystal Violet) from the water. The capacity of the selected filter systems was investigated by batch adsorption experiments. Atomic Absorption Spectroscopy (AAS) was used for the determination of metal contaminants, and Ultraviolet-Visible Spectroscopy (UV-Vis) was used for determination of dye concentrations.

Adsorption of metal ions with porous materials is a highly complex process depending on many parameters such as pore structure, total surface area, surface chemistry, ion diameter, and chemistry. A correlation between the specific surface area (SSA) and the maximum adsorption capacity of the porous samples was observed. The SiOC with a specific surface area of $4 \text{ m}^2/\text{g}$ adsorbed the zinc ions around 0.6 mg/g . When the same sample was etched with HF, the SSA was found to be $774 \text{ m}^2/\text{g}$, adsorption capacity increased up to 7.7 mg/g , and in some samples reached up to 14.8 mg/g . In experiments with Methylene Blue (MB), Rhodamine B (RB), and Crystal Violet (CV), the etched samples were exhibited much higher adsorption results compared to the untreated samples. The MB adsorption capacity of

the SiOC sample increased from 16 mg/g to 96 mg/g by etching. Two different SiOC samples with similar SSA areas (L1HF = 774 m²/g) (L3HF = 663 m²/g) showed similar adsorption capacities (96 and 104 mg / g MB, respectively).

The results revealed that all the manufactured materials have relatively limited capacity to filter the metal contaminants whereas they are successful in removing dye based compounds from aqueous solutions. The filtering capacities for compatibility were investigated with Langmuir and Freundlich isotherm models. In addition, regeneration tests were carried out. Even after the third cycle, retention efficiencies were above 97%. Final tests were conducted with industrial wastewater polluted by various dyes and the results demonstrated that the nano-micro filters successfully remove the dyes.



ATIK SU FİLTRELENMESİ İÇİN GÖZENEKLİ SERAMİKLERİN GELİŞTİRİLMESİ

ÖZET

Bu tezin kapsamında önce makro gözeneklere sahip seramikler üretilmiş, ardından mikro/mezo gözenekler eklenerek yani yapı, hem makro hem de mikro ve mezo gözeneklilik içeren hiyerarşik bir yapıya dönüştürülmüştür. Üretilen bu sistemlerin kirli suyu temizleme yönündeki denemeleri yapılmıştır. Gözenek miktarı arttırılan ya da kontrol edilebilen gözenekli seramik malzemelerin uygulama alanında da başarısı araştırılmıştır. Bu bağlamda gözenek yapısı ve miktarı hidroflorik asit dağlama ya da hidrotermal zeolite kaplama yöntemleri ile kontrol edilmeye çalışılmıştır. Test için bilimsel literatürde önemli yer teşkil eden kirleticiler seçilmiştir. Birden fazla yöntemle üretilen numuneler arasından, karakterizasyon işlemlerine göre en uygun bulunanları seçilerek denemeler gerçekleştirilmiştir. Çalışmada kullanılan tüm numuneler bu alanda ilk defa denendiği için alınan tüm sonuçlar numunelerin hem suyu arıtma hem de üretim aşamasındaki verimlerine göre karşılaştırılmıştır.

Üretilen numuneler iki grupta incelenebilir; silikon-oksi-karbür (SiOC) numuneler ve Kalsiyum-Silika-Hidrat/Kalsiyum Silikat (CSH/CS) numuneler. SiOC numuneler, seramiğimsi polimer karışımları kullanılarak üretilmiştir. Kullanılan seramiğimsi polimerlerden biri olan PDMS (poly-dimetil-siloksan) miktarları değiştirilerek yapının gözenekliliği kontrol edilmeye çalışılmıştır. Kurlama sırasında tek yönlü ısı kaynağı kullanılmasıyla, yapıdan uzaklaşan hidrojen gazı sayesinde aksiyal yönelimli kanallara sahip numuneler elde edilmiştir. Sonuçta, sıralı kanallara sahip, yüksek yüzey alanlı (121,9 m²/g), oldukça gözenekli (%83) ve yüksek geçirgenlik seviyesine sahip numuneler üretilmiştir. CS numunelerde ise öncelikle ticari CSH toz ve tablet (Xonolite) kullanılarak denemeler yapılmıştır. Daha sonra bu denemelerden alınan sonuçlar göz önünde bulundurularak, benzer özelliklere sahip CSH toz üretilmesi denenmiştir. Üretilen CSH tozlarında başlangıç Si kaynağı olarak geri dönüşümlü cam kullanılmıştır. Üretim gerçekleştirilirken Ca/Si mol oranı, değirmende öğütme süresi, NaOH eklentisi gibi kalsiyum-silikat sentez üretimi için temel parametreler araştırılmıştır. Elde edilen tüm numuneler detaylı karakterizasyonlara tabii tutulmuşlardır. Bu tozlardan yola çıkılarak farklı yöntemlerle (High Alkane Phase Emulsified Suspensions (HAPES), Sodyum-Alginate (Na-Alginate) jelleşme) üretilen monolitik yapılara uygulanan ısı işlem sonucunda makro gözenekli CS yapıları elde edilmiştir.

Üretilen sonuç CS ve SiOC numunelerinin gözenek iç duvarları düşük sıcaklıkta hidrotomal yöntemlerle zeolite kaplanarak yüzey aktifleştirilmeye çalışılmıştır. Makro gözenekli numunelerin, hidrotermal reaksiyon sonucunda gözenek iç yüzeylerinin zeolitlerle kaplanması denenmiştir. Tüm deney setlerinde numunenin içerisine koyulacağı bir reaksiyon çözeltisi (Tetrapropylammonium hydroxide (TPAOH) ve Tetraethyl orthosilicate (TEOS) karışımı) hazırlanmış sonra reakte edilecek yani zeolit ile kaplanacak numune bu çözeltiyi içeren otoklav sisteminde

150°C’de belirli sürelerde bekletilmiştir. Zeolit kaplanan numunelerin yapısal analiz sonuçlarına göre hem CS hem de SiOC numunelerde de ortalama gözenek boyutunda ve toplam gözenek miktarında düşüş gözlenmiştir. Bu düşüşün sebebi yeni oluşan bu zeolitlerin numunelerde var olan gözenek iç çeperlerini kaplayarak gözeneklerde kapanmaya ya da küçülmeye sebep olmasıdır. Ayrıca SiOC numunelerinin içinde belli bölgeler tamamen zeolit kaplanırken kimi bölgelerde kaplamanın seyrek olduğu gözlemlenmiştir.

Gözenek yapısı ve miktarını kontrol edebilmek üzere denenen bir başka yöntem de hidroflorik (HF) asit dağlama işlemidir. SiOC numuneler HF çözeltisiyle muamele edilerek dağlanmasının ardından yüzey alanı (BET), ortalama gözenek boyutu ve izotermeleri incelendiğinde; dağlanmadan önce farklı gözenekliliğe sahip numunelerde dağlandıktan sonra benzer gözeneklilik ortaya çıktığı gözlemlenmiştir. Dağlandıktan sonra tüm numuneler 700 m²/g ve üzerinde yüzey alanı göstermişlerdir, ayrıca hepsinin ortalama gözenek çapı 3-5 nm aralığına yaklaşmıştır. Bu numunelerde önce PDMS’nin pirolize sonucunda yok edilmesi ile mezo, ardından da silika yoğun faz bölgelerinin dağlanması sonucunda, yeni mezo (2-50 nm) ve daha düşük çaplı mikro (< 2 nm) gözenekler oluşmuştur. Yeni ortaya çıkarılan mikro ve mezo boyutlarda gözenek eklentisi ile yüksek yüzey alanlı bu numuneler, yüksek geçirgenlikte ve düşük geri basınçlı filtreleme araçlarına dönüştürülmüş ve karakterizasyon basamaklarını takiben, kirleticileri sudan uzaklaştırma performansları için incelenmiştir.

Üretilen numuneler, önce yapısal karakterizasyon metotları: XRD, TGA, FTIR ve RAMAN, taramalı elektron mikroskopu (SEM, mikro-yapısı) ile ardında ise gözenek boyutları ve miktarı için BET (yüzey alanı), tomografik teknikler (CT) ve cıva porozimetresi (Hg-por) ile incelenmiştir. Üretim ve karakterizasyon basamaklarından sonra tez kapsamı doğrultusunda, seçilen numunelerin sudaki kirleticileri (Kadmiyum, Bakır, Çinko, Kurşun, Krom, Metilen Mavisi, Rhodamin B ve Kristal Violet) sudan uzaklaştırma performansı değerlendirilmiştir.

Tüm bu numuneler, su arıtma testlerinde kullanılabilir seramik malzemelerdir. Seçilen numunelerin suyu temizleme performansı adsorpsiyon (adsorption) denemeleriyle araştırılmıştır. Adsorpsiyon denemelerinde, üretilen malzemelerden karakterizasyon basamaklarından sonra seçilenlerin adsorbent olarak kullanılmasına yönelik ön denemeler gerçekleştirilmiş. Belirlenen parametreler doğrultusunda metaller ve boyalar için ve her bir malzeme için ayrı ayrı optimum sonuç veren şartlarda adsorpsiyon denemeleri gerçekleştirilmiştir. İncelenen metal kirleticilerin analizleri için Atomik Adsorpsiyon Spektrometrisi (AAS) ve boyaların konsantrasyon tayini için de UV-Vis spektrometre kullanılmıştır. Üretilen numunelerin filtreleme kapasiteleri başta Langmuir ve Freundlich izoterm modelleri olmak üzere, farklı izoterm modellerine uygunluk yönünden araştırılmıştır. Tüm numunelerden adsorpsiyon deneyleri sonucunda elde edilen veriler Langmuir izoterm modeliyle uyumluluk göstermiştir. Numunelerin maksimum adsorplama kapasiteleri bu izoterm modeli kullanılarak hesaplanmıştır.

Metal iyonlarının gözenekli malzemeler ile adsorbe edilmesi, gözenek yapısı, toplam yüzey alanı, yüzey kimyası, yüzey yükü, metal iyon çapı ve kimyası gibi birçok parametreye bağlı karmaşık bir süreçtir. Üretilen gözenekli numunelerde numunenin spesifik yüzey alanı ile maksimum adsorplama kapasitesi arasında bir bağlantı gözlenmektedir. Spesifik yüzey alanı 4 m²/g olan SiOC numunesi çinko iyonlarını yaklaşık 0,6 mg/g emilim değerinde tutarken, asit ile dağlandıktan sonra SSA değeri 774 m²/g olan aynı numune için bu değer 7,7 mg/g’a kadar yükselmiştir ve bazı numunelerde 14,8 mg/g mertebesine ulaşmıştır.

Test edilen MB, CV ve RB boylarına yönelik yapılan deneylerde, metal kirleticileri uzaklařtırmak üzere yapılan deneylerdeki sonuçlara benzer şekilde numunelerin asit ile dađlanmıř halleri, dađlanmamıř hallerine kıyasla çok daha yüksek emilim göstermiřtir. Örneđin yüzey alanı 4 m²/g olan SiOC numunesinin MB'yi adsorplama kapasitesi dađlama iřlemi ile 16 mg/g'dan 96 mg/g'a kadar yükselmiřtir. Yüzey alanları birbirine yakın olan iki farklı SiOC numunesi ise (L1HF = 774 m²/g ve L3HF = 663 m²/g) benzer adsorplama kapasiteleri (sırasıyla 96 ve 104 mg/g MB) göstermiřlerdir.

Zeolit kaplama iřleminde sonra ise test edilen metal iyonları için, numuneler substratlarına göre %50'ye yakın oranlarda daha düşük adsorplama kapasitesi gösterirken bu deđerler boylar söz konusu olduđunda %35 ile %85 düşüş göstermiřtir.

Adsorpsiyon denemelerinde kullanılan adsorbent maddenin başarı kriterlerinden biri de malzemenin tekrar kullanılabilirliđidir. Malzemenin tekrar kullanılabilirliđi, adsorplanan analitin malzemenin uzaklařtırılabilmesine ve bu iřlem yapılırken malzemenin fiziksel ve kimyasal yapısının deđiřtirilmeden kalabilmesine bađlıdır. Bu bilgiler ışığında iki farklı prosedür takip edilerek tekrar kullanılabilirlik denemeleri gerçekleştirilmiřtir. Birinci sistemde kimyasal ekstraksiyon ile numunelerin yüzeyinde emilen boya molekülleri malzemenin uzaklařtırmaya çalışılmıřtır. İkinci sistemde ise literatürde sıklıkla kullanılan bir yöntem olan termal rejenerasyon yani yüklü malzemeyi belli sıcaklıklara maruz bırakarak boyların dekompoze olması denenmiřtir. Isıl iřlem ile yapılan denemelerde alıkonma verimi üçüncü döngü sonunda dahi %99 oranındayken boya moleküllerini ekstrakte etmek için etanol kullanıldıđında bu deđer %97'ye kadar düşmüřtür.

Üretilen malzemelerin kirliliklerden herhangi biri için ayırt edici bir adsorplama başarısı gösterip göstermediđini arařtırmak için bilinen konsantrasyonlarda üç boya da içeren karıřım hazırlanmıř ve aynı şekilde adsorpsiyon testlerine tabii tutulmuřtur. Bu üç boyanın da adsorplanma yüzdeleri birbirine benzerlik göstermiř, ayırt edici bir adsorpsiyon yüzdesi kaydedilememiřtir. Sekiz saatin sonunda her üç boyada da %98 oranında alıkonma görülmüřtür. Bu bağlamda test edilen numunenin herhangi bir boyaya karřı özel bir ilgisi (afinite) yoktur ancak 24 saatlik kontak süresi sonunda her üç boya da aynı anda %99 oranının üzerinde emebilme kapasitesine sahiptir. Yüksek miktarda boya adsorplayan bu numunelerin, adsorpsiyon iřleminde sonraki yapısı karakterizasyon metotları kullanılarak gözlemlenmeye çalışılmıřtır. Bu bağlamda SiOC numunesinin boya ile yüklendikten sonra BET yüzey alanının 700 m²/g'dan 500 m²/g civarına düřtüđü ölçülmüřtür. Aynı numune yine boya ile doyurulduktan sonra Taramalı Elektron Mikroskopu/ Enerji Dađılım Spektrometre (SEM-EDX) analizlerine tabii tutulmuř, yüzey gözeneklerinin kapandıđı ve yüzeyin görece pürüzsüz bir tabaka haline geldiđi burada da gözlemlenmiřtir. Yüzey alanındaki azalma, yüzey karakterindeki deđiřme ve gözenek dađılımındaki farklılıklar boyların malzemenin yüzeyine tutunduđunu gösteren bulgular olarak kabul edilebilir.

Tüm bahsi geçen denemeler sentetik olarak oluřturulan, kirlilikleri içeren sulu çözeltilerde gerçekleştirilmiřtir. Gerçek atık sularda çeřitli kirlilikler bir arada bulunmaktadır ve bu çeřitli girişimler ile filtreleme prosesini etkileyebilir. Bu etkiler ve boylar ve metallerin eşzamanlı olarak adsorplanma kapasitesinin arařtırılması için endüstriyel atık su arıtma merkezlerinden alınan gerçek atık su ile denemeleri yapılmıřtır. Kendi hazırladıđımız ve içerisinde sadece bir kirletici olan test sonuçlarına benzer şekilde çinko iyonunda en yüksek alıkonma gözlemlenmiřtir. Ancak bu denemelerde içinde birçok kirlilik özellikle askıda katı madde (AKM) de

olan endüstriyel atık su ile hiçbir ön işlem yapılmadan çalışılmıştır. Bir gram HF dağlanmış SiOC numunesi, yaklaşık 80 mg/L gibi yüksek bir konsantrasyondaki çinkoyu %30'u geçen bir başarı ile adsorplarken, bakır ve krom da %20 mertebesinin üzerinde alıkonabilmiştir. Yine kirleticilerden birini içerecek şekilde hazırlanan sulu çözeltilerdeki sonuçlara benzer olarak, numuneler metallere nazaran boyaları daha iyi adsorplamış ve her boya için de %70'lerin üzerinde uzaklaştırma başarısı göstermiştir.

Araştırılan kirleticileri sudan uzaklaştırma konusunda yapılan kapsamlı incelemeler, üretilen tüm malzemelerin çalışılan metalleri filtreleme konusunda sınırlı kapasiteye sahip olduğunu ancak seçilen boya bazlı kirleticileri sulu çözeltilerden uzaklaştırma konusunda başarılı olduğunu ortaya çıkarmıştır. Ayrıca tekrar kullanılabilirlik (rejenerasyon) testleri de gerçekleştirilmiş, üçüncü döngü sonunda dahi alıkonma verimi %97 mertebesinin altına düşmemiştir. Yine boya karışımları ve endüstriyel atık su arıtma merkezinden toplanan kirli suyla da performansı incelenen numuneler, benzer şekilde boyalara karşı oldukça başarılı nano-mikro filtreleme malzemeleridir.



1. INTRODUCTION

Access to clean water are recognized as basic human right. About three quarters of the Earth's surface is covered by water. However more than 97% of all water resources is saline water. Fresh water usable by humans is less than 0.01% of all water in the world [1]. Contamination of fresh water, the world's most limited natural resource, by human activities is a major problem. The main reasons behind the pollution of water resources are agricultural activities, industrial water usage and domestic consumptions.

Today, 18% of the world's population is not able to access clean water, while in 2030, the number of people facing severe water scarcity is expected to reach 50% of the total world population [2].

Contamination of water resources by physical, chemical, biological or radiological pollutants is a major problem in both developing and industrialized countries. Water resources are mostly polluted by the industrial and agricultural activities. Examples of water pollutants include metals and organic-synthetic chemicals (e.g. dyes). Health agencies such as World Health Organization (WHO) and American Public Health Association (APHA)[3] has determined threshold concentrations ranging from 5 $\mu\text{g/L}$ to 100 $\mu\text{g/L}$ for heavy metals that may be found in drinking water and which may have severe negative impact on human health [4]. As heavy metals have carcinogenic to human health and toxic effects to the environment, treatment of wastewaters containing zinc, cadmium, copper, lead and chromium has critical importance [5]. Although trace amounts of zinc, cadmium, and copper are necessary for human health, excessive exposure to these metals can cause serious health problems such as cramps, vomiting, skin irritations, vertigo, nausea, and anaemia. Chromium has two valance states; trivalent chromium (Cr(III)) and hexavalent chromium (Cr(VI)). Cr(VI) is more toxic than Cr(III) and has more severe impacts on the human health [4, 6]. Lead in wastewater mainly comes from battery manufacturing, dyeing, and printing industries. Lead poisoning can cause critical problems in the central nervous system such as headache, memory loss, irritability

and neuro-developmental abnormalities [7, 8]. The impact of these metals on human health shifts from positive to the negative impact with very low concentration differences. Therefore, trace metal removing from the wastewater resources has critical importance for human health.

As a result of industrial activities (e.g. textile, paper, plastics, printing, and leather industries waste products), many dyes such as methylene blue (MB), crystal violet (CV) and rhodamine B (RB) and the by-products formed as a result of the degradation of these dyes are sources of water pollution [9].

In this context, low cost and high efficiency wastewater purification is critically important for human and environmental health.

Coagulation, flotation, ion exchange, sedimentation, electrolysis, chemical oxidation, disinfection, precipitation and adsorption are the most used water treatment technologies [10-20]. Among these techniques, adsorption is an effective and widely used process for removing pollutants from wastewater. Adsorption-based methods become prominent due to their applicability to different types of pollutants with ease of design and production, in comparison to the above-mentioned methods [21-24]. Adsorption is defined as the increase in the concentration of the specific substances (adsorbate) on the surface of the adsorbent [25]. The base of removing contaminants with adsorption technique is adhering or bonding of pollutants in a liquid or gas phase onto a solid adsorbent (solid phase extraction). Adsorption is a surface phenomenon that can be identified under two headings; chemical and physical adsorption [26]. In physical adsorption, weak van der Waals' forces between atoms or molecules are involved and it is generally reversible. Instead, chemical adsorption is the result of stronger forces and usually irreversible [27, 28].

In general, contaminated waters include more than one type of pollutant. For this reason, the real success of water treatment technologies should be measured by simultaneous removal of different contaminants from the wastewater. Although membrane technologies (filtering, reverse osmosis, etc.) can offer solutions in this regard, their cost is a problem for their wide use. Adsorption, with high surface area and adsorption capacity adsorbents is an important alternative for water treatment as they offer more economical solution [29]. In spite of high number of studies on removal of impurities by adsorption method, there are very few materials and studies on focusing different pollutants simultaneously [30].

For the adsorption process, different materials such as activated carbon, porous minerals, ceramics, zeolites, polymeric materials have been used [31-36].

Activated carbon is the most widely used adsorbent [37-41]. Activated carbon used in water treatment is usually obtained by chemical or thermal processes. It can be produced by pyrolysis of organic materials (e.g. coconut shell[42, 43], fruit seeds[44, 45], and wood[46, 47]) followed by pyrolysis in an oxygen-free atmosphere at about 850 °C.

Activated carbon has irregular pore structure and after a period of use, these pores reach the saturation and the adsorption capacity is reduced. In addition, due to deposition during the treatment process, the pore size continuously reduces and this decrease is reflected in the system as an increase in the pressure drop. The chemical or thermal processes to solve this problem are costly and can cause irreversible damage in the material [41].

As an alternative to activated carbon, the carbon derived carbide (CDC) can be used and the surface area can be further increased by the subsequent activation. The form, pore size and surface area of the resulting CDC can be precisely adjusted according to the field of application [48-50].

Porous ceramics can be used in many applications due to their unique properties such as low density, high thermal shock resistance and high chemical stability. It is known that porous ceramics can be used in filtration (in diesel particulate, molten metal, and hot gas filtration), in construction of porous bio-implants and sensors [51-57]. Both chemical structure and pore character of the ceramic plays an important role in its use in different fields. Meso/macro pores provide function to the system according to the application.

Calcium silicate hydrates and zeolites with the high specific surface areas are other successful adsorbents for water purification processes [58]. However, it is very difficult to manufacture these materials with controlled pore structure and amount [59]. Kuwahara *et. al.*[60] synthesized calcium silicate adsorbent with different Ca/Si ratios by using blast furnace slag. The adsorption capacity of the material synthesized with the SSA, 219 m²/g and the total pore volume of 0.78 cm³/g, was 118.3 mg/g for Cu(II). In another study, wollastonite (a calcium silicate) was tested for removal of metals from contaminated water and yielded very successful results. However, in this study the possibility of hierarchical porous structure production was

completely ignored. The specific surface area and porosity for this material were found 1.1 m²/g and 23%, respectively [61].

Parameters such as pore size distribution (PSD), specific surface area (SSA), aligned, open, closed, increased porosity can greatly affect the function of ceramics in potential applications. For example, while the high surface area, micro (<2 nm) and meso (2-50 nm) porosity are preferred properties for many applications, macroporosity (for all pores larger than 50 nm) is an advantage for mass and heat transfer. Similarly, aligned porosity provides the advantage of axial permeability [62].

Porous ceramics with different pore sizes/shapes can be produced using pre-ceramic polymers. Polysiloxanes are among the most economical pre-ceramic polymers. They can be used under the open-air atmosphere and transformed into silicon-oxy-carbide (Si-O-C) ceramics when pyrolyzed at temperatures in between 800-1400 °C.

Porous ceramics can also be obtained by using mixtures of poly-methyl-silsesquioxane (PMS), poly-methyl-phenyl-silsesquioxane (PMPS) and poly-dimethyl-siloxane (PDMS) [63, 64]. The porosity of materials increases with the amount of PDMS. It is possible to control the pore size and amount of porosity (> 70%). The pore-forming effects of PDMS polymers with different molecular weights and different pyrolysis temperatures were given by *Blum et al* [65]. The mixture of PDMS, polyhydromethyl-siloxane (PHMS) and 2,4,6,8-tetravinyl-2,4,6,8-tetramethylcyclone tetra-siloxane (TMTVS) were used produce polymer-derived ceramics. Although ceramics obtained from pre-ceramic polymers were studied for the last forty years, the applications of these materials are inadequate [66-69].

The main objective of this study is to produce as mentioned porous calcium silicate and polymer derived ceramics to test for wastewater purification capabilities.

2. EXPERIMENTAL

2.1 Materials and Method

2.1.1 Reagents

Three types of polysiloxanes were used: a linear polymethylhydrosiloxane (Gelest, PHMS, MW~2100-2400, 30-45 cSt, CAS: 63148-57-2, Gelest, USA) having Si-H bonds, a vinyl-terminated polydimethylsiloxane (PDMS, MW:62700, 10000 cSt, CAS: 68083-19-2, Gelest, USA) and a cyclic 2,4,6,8-tetramethyl-2,4,6,8-tetravinylcyclotetrasiloxane (TMTVS 97%, Alfa Aesar, USA, CAS: 2554-06-5).

Platinum - divinyltetramethyldisiloxane complex, (Pt, CAS: 68478-92-2, Sigma-Aldrich, USA), Diazabicyclo (2.2.2) octane (DABCO, CAS: 280-57-9) and Tin(II) 2-ethylhexanoate (Tin, CAS: 301-10-0), (Sigma- Aldrich, USA) were used as catalyst for the curing reactions. Hydrotalcite, (LDH with a formula $(\text{Mg}_6\text{Al}_2(\text{CO}_3)(\text{OH})_{16}\cdot 4\text{H}_2\text{O})$, CAS: 11097-59-9, Sigma-Aldrich, USA) and $\text{Ca}(\text{OH})_2$ (TS EN 459-1 CL 90S) was used as received.

Xonotlite, (Promaxon-D, $\text{Ca}_6\text{Si}_6\text{O}_{17}(\text{OH})_2$, Promat, Belgium), (with average particle size 35-85 μm). The sodium alginate (Na-Alg, CAS:9005-38-3, Sigma-Aldrich, USA) sodium lauryl sulphate (SLS, $\text{CH}_3(\text{CH}_2)_{11}\text{SO}_4\text{Na}$, CAS: 151-21-3, BASF, USA) or poly-oxyethylenesorbitan monolaurate (Tween 20, Mw: 1228, CAS: 9005-64-5, Sigma Aldrich, USA) were used as surfactant. As a gelation agent polyvinyl alcohol (PVA, Mw:31.000, CAS: 9002-89-5, Sigma-Aldrich, USA) and as dispersion agent a carbonic acid based polyelectrolyte (Dolapix CE 64, Zschimmer & Schwarz GmbH, Germany) were used.

For hydrothermal reaction, Tetrapropylammonium hydroxide solution (TPAOH, $\text{C}_{12}\text{H}_{29}\text{NO}$, CAS: 4499-86-9) and Tetraethyl orthosilicate, (TEOS, $\text{Si}(\text{OC}_2\text{H}_5)_4$, 98%, CAS: 78-10-4) were used.

1000 mg/L standard solutions ($(\text{Cr}(\text{NO}_3)_3$ CAS: 13528-38-4), $(\text{Cd}(\text{NO}_3)_2$ CAS: 10325-94-7), $(\text{Pb}(\text{NO}_3)_2$ (CAS: 10099-74-8)), $(\text{Zn}(\text{NO}_3)_2$ CAS: 7779-88-6) and $(\text{Cu}(\text{NO}_3)_2$ CAS: 3251-23-8)) all analytical grade (Merck, Germany) were used to prepare the stock solutions. The dyes; Methylene Blue (MB, $\text{C}_{16}\text{H}_{18}\text{ClN}_3\text{S}$, CAS:

122965-43-9), Crystal Violet (CV, $C_{25}H_{30}ClN_3$, CAS: 548-62-9) and Rhodamine B (RB, $C_{28}H_{31}ClN_2O_3$, CAS: 81-88-9) (Merck, Germany), were used without further purification. For adjusting the pH of each solution, Sodium hydroxide (NaOH, CAS: 1310-73-2), nitric acid (HNO_3 , CAS: 7697-37-2) and hydrochloric acid (HCl, CAS: 7647-01-0), (Merck, Germany) were used.

2.1.2 Instruments

A ball mill (PM 100, Retsch, Germany), an overhead stirrer (MS3040, MTOPS, Republic of Korea), a magnetic stirrer and heater (Heidolph, Germany) and a tubular furnace (PROTERM PTF 16/75/450, Turkey) were used to manufacture and pyrolyze of the samples.

X-ray diffraction (XRD) measurements were carried out with an Italstructures (IPD3000/CPS 120) instrument equipped with a Cu anode source operating at 40 kV and 30 mA. ^{29}Si MAS NMR spectrum was collected with a Bruker 300WB nuclear magnetic resonance instrument (Bruker Instruments, Germany). The morphological features of samples were analyzed from fresh fracture surfaces using a scanning electron microscope (FEI-Philips XL30 ESEM-FEG, the Netherlands) after 10 nm Pt film deposition by sputtering were used for characterization. Samples were analyzed by nitrogen (N_2) gas adsorption/desorption at 77 K using Micromeritics ASAP 2010 sorption analyser (Norcross, GA). Specific surface area (SSA) was calculated from a BET (Brunauer, Emmet and Teller) analysis in the P/P_0 range of 0.05-0.30 with at least five data points. The pore size distributions in the mesopores range were obtained from the desorption branch of the isotherm through the BJH (Barret, Joyner and Halenda) analysis.

The WTW pH 340-A/SET2 pH meter (Weilheim, Germany) was used for adjust the pH of solutions. A TKA reverse osmosis and a TKA deionizer system (TKA, Germany) was used for obtain ultra-pure water with 18.2 $M\Omega$ cm resistivity. For separation of aqueous solution and materials, a MRC centrifuge (MRC Scientific Industries, UK) was used.

Quantitative determination of all metals was carried out by an Analytik Jena, ContrAA 700 high-resolution continuum called - source atomic absorption spectrometer (HR-CS AAS) with flame model, (Analytik Jena, Germany). Measurements were performed at 217.005 nm for Pb, 228.801 nm for Cd, 357.800 nm for Cr(III), 213.900 nm for Zn(II) and 324.800 nm for Cu (II). A Shimadzu UV-

2700, Ultraviolet–visible (UV-Vis) spectrometer (UV-2700, Shimadzu, Japan) was used for the determination of MB, CV, and RB at the wavelengths of 668, 589, and 555 nm, respectively.

2.2 Manufacture of SiOC

The production of SiOC samples can be divided into two parts. In the first part, the production of monolithic foam samples was explained and in the second part; micron sized beads were produced by emulsion method.

2.2.1 Porous SiOC foams

Mixture of PHMS, PDMS, cyclic TMTVS and LDH prepared at ratios given in Table 2.1 for each sample were mixed with a magnetic stirrer at 500 rpm. After 5 minutes, 0.71 g of catalyst (~Pt 2% in xylene) was added dropwise to the mixture and stirring was continued at the same condition for 20 minutes. The homogeneous mixture was poured into aluminium moulds. The blend was cured at 200 °C for 12 hours.

Table 2.1 : Quantities of chemicals used in the production of L series samples.

Sample Code	PHMS (g)	PDMS (g)	Cyclic TMTVS (g)	LDH (g)
L1	25.00	6.25	1.36	1.36
L2	25.00	12.50	1.36	1.36
L3	25.00	25.00	1.36	1.36
L4	25.00	0.00	1.36	1.36

2.2.2 SiOC beads

The following procedures were applied to produce micro-sized non-porous (oil in water, o/w) and macro-porous (water-in-oil-in-water, w/o/w) polymeric beads and their turn to SiOC.

2.2.2.1 ‘Oil-in-water’ emulsion

Two phases, oil phase and water phase, were used for these emulsion samples. The ‘water phase’ were prepared with mixture of DI water and surfactant (Tween-20), while PHMS, cyclic siloxane and the catalyst (one of the Pt, Tin or DABCO catalysts) were mixed for the oil phase. Both phases were prepared by mixing with magnetic stirrer at 500 rpm on borosilicate glass beakers.

The oil phase was added dropwise to the water phase, allowing the formation of micro-particles. After addition of the oil phase, stirring was continued for another 30 minutes at the room temperature. The emulsion was poured into a petri dish and kept 24 hours at 80 °C for crosslinking. The samples were then pyrolyzed in a tubular furnace at 1300 °C for 1 hour (heating rate was 2 ° C /min and N₂ gas flow was 0.2 L/min). Table 2.2 shows details for produced samples with three different catalysts.

Table 2.2 : Details for thermoset siloxane beads samples produced with O/W emulsion method.

Sample Code	DI (mL)	Tween 20 (g)	PHMS (g)	Cyclic (g)	% Pt Catalyst*	% Tin Catalyst*	% DABCO Catalyst*	O/W ratio
EP-PP-54	10.04	0.11	2.51	0.17	2.82	0.00	0.00	0.26
EP-PP-55	10.09	0.10	2.51	0.17	0.00	2.72	0.00	0.26
EP-PP-56	10.08	0.13	2.52	0.16	0.00	0.00	2.23	0.26
EP-PP-57	40.03	0.45	10.04	0.67	2.35	0.00	0.00	0.26

* Catalyst ratios were given with respect to PHMS.

2.2.2.2 ‘Water-in-oil-in-water’ emulsion

The first water phase and the oil phase are combined as described in section ‘2.2.2.1 Water-in-oil-emulsion method’. The second water phase was then prepared and slowly added to the stirred oil in water (details given in Table 2.3). The resulting mixture was stirred for 30 minutes in a magnetic stirrer. The mixture was poured in a petri dish and dried in an oven at 80 °C for 24 hours. The selected samples were pyrolyzed in tubular furnace at 1300 °C for 1 hour at maximum temperature (heating rate of 2 °C/min and 0.2 L N₂/min). Table 2.3 shows details for produced samples with three different catalysts.

Table 2.3 : Details for thermoset siloxane beads samples produced with W/O/W emulsion method.

Sample Code	DI 1.water phase (mL)	Tween 20 1.water phase (g)	PHM S (g)	Cyclic (g)	Pt Catalyst* (%)	DI 2. water phase (mL)	Tween 20 2.water phase (g)
EP-PP-51	10.03	0.14	2.51	0.17	2.82	40.03	0.42
EP-PP-52	10.03	0.14	2.51	0.17	9.38	40.03	0.42

* Catalyst ratios were given with respect to PHMS.

2.2.3 HF etching of SiOC

The samples were etched with hydrofluoric acid. Samples were treated at room temperature with a 48% v/v HF aqueous solution for 4 days and stirred every 12 hours, rinsed with water. Etched and rinsed samples were dried at oven at 65 ° C for 24 hours.

The characterization tests (XRD, BET, TGA) were performed for these samples before and after etching processes.

2.3 Manufacture of CSH/CS

CSH powders were produced and used for the formation of porous monolithic CS/CSH structures.

2.3.1 CSH powder

CSH powders with different Ca/Si molar ratios were synthesized by using hydrate lime (TS EN 459-1, CL 90S) and recycled glass. The chemical compositions of recycled glass and Ca(OH)₂ used in the production of CSH powder are given in Table 2.4.

Recycled glass was ground in a ball mill for 12 hours then sieved to 32-25 μm.

The ground glasses were passed through series of sieves consisting of different openings (mesh) (Figure 2.1). At the bottom of this system, there is 25 microns sieve with a 32 microns sieve above it, below this sieve all powder will be below 32 microns.

Table 2.4 : The detail of recycled glass.

Recycled glass	Lime hydrate
%	%
SiO ₂ : 71.59	Ca(OH) ₂ : 90.4
Al ₂ O ₃ : 1.23	Grain size: 90-200(μ)
Fe ₂ O ₃ : 0.082	
TiO ₂ : 0.047	
CaO: 8.73	
MgO: 4.17	
Na ₂ O: 13.63	
K ₂ O: 0.03	
SO ₃ : 0.22	



Figure 2.1 : a) ball mill mortar used to grind recycling glass, b) various sieves and sieved recycling glasses.

The milled recycled glass and Ca(OH)₂ were weighed according to the Ca/Si molar ratios given in Table 2.5. The mixture was milled at 250 rpm for 10 hours at the ball mill with the addition of DI water (20 mL of 0.1 N NaOH solution was added for sample XRG01-34) and stirred. The mixture was transferred to a beaker and homogenized with a magnetic stirrer at 500 rpm for 30 min. The homogenized mixture was put into a Teflon vessel and transferred into the autoclave for hydrothermal treatment. After hydrothermal reaction, the autoclave was cooled down the room temperature. The products were washed with DI and dried in an oven at 80 °C, overnight.

Table 2.5 : Details of the process used to produce CSH powders.

Sample	DI (ml)	0.1N NaOH (ml)	Molar ratio (CaO/SiO₂)	Ball mill (250 rpm) (h)	Hydrothermal reaction time (h)
XRG01	50.00	20	0.83	-	20
XRG02	50.00	20	1.13	-	20
XRG03	50.00	20	2.13	-	20
XRG04	50.00	20	3.12	-	20
XRG11	50.00	20	0.83	0.5	20
XRG12	50.00	20	1.13	0.5	20
XRG13	50.00	20	2.13	0.5	20
XRG14	50.00	20	3.12	0.5	20
XRG21	50.00	20	0.83	3	20
XRG22	50.00	20	1.13	3	20
XRG23	50.00	20	2.13	3	20
XRG24V	50.00	20	3.12	3	20
XRG31	50.00	20	0.83	10	20
XRG32	50.00	20	1.13	10	20
XRG33	50.00	20	2.13	10	20
XRG34	50.00	20	3.12	10	20
XRG41	70.00	-	0.83	-	20
XRG42	70.00	-	1.13	-	20
XRG43	70.00	-	2.13	-	20
XRG44	70.00	-	3.12	-	20

Table 2.5 (continued): Details of the process used to produce CSH powders.

Sample	DI (ml)	0.1N NaOH (ml)	Molar ratio (CaO/SiO₂)	Ball mill (250 rpm) (h)	Hydrothermal reaction time (h)
XRG51	70.00	-	0.83	0.5	20
XRG52	70.00	-	1.13	0.5	20
XRG53	70.00	-	2.13	0.5	20
XRG54	70.00	-	3.12	0.5	20
XRG61	70.00	-	0.83	3	20
XRG62	70.00	-	1.13	3	20
XRG63	70.00	-	2.13	3	20
XRG64	70.00	-	3.12	3	20
XRG71	70.00	-	0.83	10	20
XRG72	70.00	-	1.13	10	20
XRG73	70.00	-	2.13	10	20
XRG74	70.00	-	3.12	10	20
XRG02-1	50.00	20	1.13	-	4
XRG12-1	50.00	20	1.13	0.5	4
XRG22-1	50.00	20	1.13	3	4
XRG32-1	50.00	20	1.13	10	4
XRG42-1	70.00	-	1.13	-	4
XRG52-1	70.00	-	1.13	0.5	4
XRG62-1	70.00	-	1.13	3	4
XRG72-1	70.00	-	1.13	10	4

2.3.2 CS/CSH monolith

Porous CSH monoliths were produced with two different methods; gelation with sodium alginate and high alkane phase emulsified suspensions (HAPES).

2.3.2.1 Gelation

In order to produce porous CSH monolith, synthesized CSH (XRG71) was used. The sodium alginate (Na-Alg) relative to the powder was used as the gelation agent, SLS surfactant and PVA used as a stabilizer. Na-Alg solution was prepared by dissolving in 10 mL DI water. PVA was added to 10 mL DI water and heated 80 °C, stirred with a magnetic stirrer until the solution is clear.

The synthesized CSH was slowly added to 30 mL deionized water containing Dolapix CE 64 (1.5 wt% related to CSH) as a dispersion agent while mixing with the overhead stirrer. The ratios of the chemical used are given in Table 2.6. The Na-Alg solution and surfactant were added into the slurry and mixed for 3 min at 2000 rpm. PVA solution (if used) was added to the slurry and stirred 10 min at 2000 rpm. The suspensions were poured into the mould and dried for 48 hours at room temperature, sintered 1000 °C for 1 h.

Table 2.6 : The amount of chemicals used for the monolith ‘Alginate’ samples produced by the gelation method.

Sample	DI (mL)	Dolapix (g)	CSH (XRG71) (g)	SLS (g)	Tween-20 (g)	Na-Alg (g)	PVA Solution (wt%) (g)
Alginate1	30.00	0.16	10.00	0.05	-	1.00	1.30
Alginate2	30.00	0.16	10.00	0.05	-	0.50	1.30
Alginate3	30.00	0.16	10.00	0.05	-	1.00	2.60
Alginate4	30.00	0.16	10.00	0.05	0.3	1.00	1.30
Alginate5	30.00	0.16	10.00	0.10	0.3	1.00	1.30
Alginate6	30.00	0.16	10.00	0.05	0.3	0.50	1.30
Alginate7	30.00	0.16	9.00	0.05	0.3	0.50	-
Alginate8	30.00	0.16	9.00	0.10	0.3	0.50	-

2.3.2.2 HAPES

Produced CSH was mixed DI water, Dolapix, Decane, and SLS to produce porous monolithic structures. These raw materials are used to form alkane phase, and this system is called , high alkane phase emulsified suspensions, HAPES [70]. XRG41,42,43 and 44 synthesized powders were used for HAPES41,42,43 and 44 samples respectively, while XRG71,72,73 and 74 were used for HAPES71,72,73 and 74 samples, see Table 2.7.

Table 2.7 : The amount of chemicals used for the monolith ‘HAPES’ samples.

Sample	DI (ml)	CSH (wt%)	Dolapix CE-64 (wt%)	Decane (vol%)	SLS (vol%)
HAPES41	30.00	30.00	0.78	46.31	0.33
HAPES42	30.00	30.00	0.78	46.31	0.33
HAPES43	30.00	30.00	0.78	46.31	0.33
HAPES44	30.00	30.00	0.78	46.31	0.33
HAPES71	30.00	30.00	0.78	46.31	0.33
HAPES72	30.00	30.00	0.78	46.31	0.33
HAPES73	30.00	30.00	0.78	46.31	0.33
HAPES74	30.00	30.00	0.78	46.31	0.33

DI water and dolapix were mixed with a magnetic stirrer for 3 minutes at RT with 1250 rpm. An overhead stirrer was used to mix the suspension. While mixing speed was gradually increased to 2000 rpm, produced CSH (XRG) was slowly added. Decane and SLS were added to this mixture to form emulsion. The mixture was stirred for 15 minutes with the overhead stirrer to obtain a foam structure. The resulting mixture was poured into aluminium moulds and dried at RT for 48 hours. The heat treatment was applied to the selected samples for 1 hour at 1000 °C or 1200 °C in a muffle furnace, in an open atmosphere to obtain CS ceramics. The pictures of the used overhead stirrer and the green HAPES samples are shown in Figure 2.2.

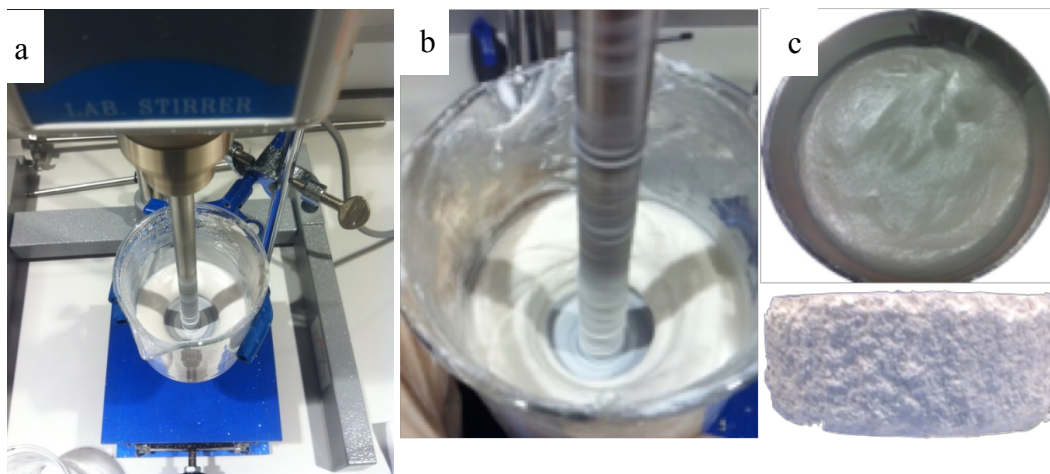


Figure 2.2 : a and b) Preparing HAPES samples with using the overhead stirrer, c) images of moulded and green HAPES sample.

2.4 Zeolite Coating

Macro-porous SiOC and CSH samples were intended to be coated by zeolite via hydrothermal reactions. In the case all zeolite coating experiments, a reaction solution (called SOL) was prepared in which the sample was placed in it. The whole system was kept in the autoclave to be coated at certain temperatures and durations. The hydrothermal zeolite coating process was carried out at 150 ° C, with 70% volumetric fill. The closed autoclave system (acid digestion bomb) is shown in Fig.2.3.



Figure 2.3 : Static autoclave systems.

2.4.1 Zeolite coating of CSH

The reaction solution (SOL1) was prepared from the mixture of TPAOH/H₂O/TEOS with molar ratios 0.1/10/0.1, was stirred for 15 minutes with a magnetic stirrer. In the coating process, which was carried out by using commercial blocks of calcium-silicate-hydrate (CSH, Xonotlite, Ca₆Si₅OH), blocks were weighed and put into the Teflon (PTFE) reaction vessels with the SOL1 solution. The teflon vessels were filled with the SOL1 solution (70% v/v) and was placed in the steel autoclave system and hydrothermal reaction was conducted at 150 °C. The proportions of the chemicals used are given in Table 2.8. The produced samples are coded HZC-XT (Hydrothermal Zeolite Coating- Xonotlite).

Table 2.8 : Details of the process used to produce HZC-XT samples.

Sample Code	DI (ml)	TEOS (g)	TPAOH (g)	CSH (commercial) (g)	Time (day)
HZC-XT-1	60.00	6.96	6.80	1.00	3
HZC-XT-1 (heat treated)	60.00	6.96	6.80	1.00	3
HZC-XT-1 (not heat treated)	60.00	6.96	6.78	1.56	3
HZC-XT-2	60.00	6.97	6.80	1.21	5
HZC-XT-3	60.00	6.97	6.79	1.32	7
HZC-XT-4	60.00	6.96	6.78	1.07	10

The hydrothermal reactors were locked and the reaction was carried out in the drying-oven set to 150 °C. At the end of the period, the hydrothermal reactors were cooled to RT. The samples were removed the hydrothermal reactors, washed several times with DI water and dried at 90 °C.

2.4.2 Zeolite coating of SiOC

The reaction solution (SOL2) was prepared from the mixture of TPAOH/H₂O/TEOS with molar ratios 0.16/30/1, was stirred for 15 minutes with a magnetic stirrer. The SiOC samples (L1 or L3) to be coated were weighed and taken to the teflon reaction vessel. The containers were filled to a maximum of 70% by volume with the SOL2 solution. The hydrothermal reactors were locked and the reaction was carried out in the oven set to 150 °C. The samples were removed from the hydrothermal reactors,

washed several times with DI water and dried at 90 °C. The proportions of the chemicals used are given in Table 2.9. The produced samples are coded HZC-PDC (Hydrothermal Zeolite Coating- Polymer Derived Ceramic).

Table 2.9 : Details of the process used to produce HZC-PDC samples.

Sample Code	DI (ml)	TEOS (g)	TPAOH (g)	Substrate Code	Time (day)
HZC-PDC-1	50.00	19.41	3.06	L3	3
HZC-PDC-3	50.00	19.46	3.06	L3	5
HZC-PDC-4	50.00	19.40	3.08	L3	7
HZC-PDC-5	50.00	19.40	3.09	L3	10
HZC-PDC-7	50.00	19.41	3.08	L1	3
HZC-PDC-8	50.00	19.42	3.08	L1	5
HZC-PDC-9	50.00	19.40	3.08	L1	7
HZC-PDC-10	50.00	19.40	3.08	L1	10

2.5 Removal of Pollutants from Aqueous Solution

2.5.1 Batch adsorption

The samples were dried and ground below 500 microns, sieved and ready to use in water treatment studies. For batch adsorption studies, the impact of initial solutions, pH, contact time and adsorbent dosage was investigated. The pH of initial solutions was set ranging from 2.0 to 10.0. The effect of adsorbent dosage from 1 g/L to 40 g/L and the contact time from 0.5 h to 72 h were examined.

Ground samples were weighed and combined with prepared aqueous solutions. It was ensured that the adsorption equilibrium was reached by shaking during the contact time. Once the equilibrium was reached, the solution and adsorbent were separated by centrifuging (6000 rpm, 15 mins). The concentration of metal ions remaining and initial solutions were measured by AAS. Initial and final concentrations of dye solutions were determined by UV-Vis.

2.5.2 Maximum adsorption capacities

To determine the maximum adsorption capacities, sorbent dosage, pH, and contact time were kept constant and dye or metal ion solutions at different initial

concentration were altered. Initial and final concentrations of pollutants were analyzed and the fitting to Langmuir and Freundlich isotherms were investigated. The maximum adsorption capacity values were calculated from these isotherm models.

The Langmuir isotherm model presume monolayer adsorption on a homogeneous adsorbent surface [71]. A basic assumption is that the adsorbent reached the saturation point at the equilibrium. The Langmuir isotherm model assumes that all the adsorption sites to be identical and each site retains one analyte molecule. The adsorbed amount per unit of adsorbent at equilibrium Q_e (mg/g) was calculated using the following expression given in equation 2.1. C_0 (mg/L) and C_e (mg/L) refer to adsorbate concentration in the initial and at the equilibrium, respectively. While V (mL) is denoted volume of the solution, m (g) is the amount of adsorbent used.

$$Q_e = \frac{(C_0 - C_e)}{m} * V \quad (2.1)$$

In the following equation, the linear form of Langmuir isotherm is given.

$$\frac{C_e}{Q_e} = \frac{1}{q_m * K_L} + \frac{1}{q_m} * C_e \quad (2.2)$$

Where K_L (L/mg) refers to the Langmuir constant and q_m (mg/g) is the maximum adsorption capacity. To calculate q_m and K_L , the curve of C_e against $\frac{C_e}{Q_e}$ is used from the linear form of equation.

Freundlich isotherm model may be used to model adsorption on a heterogeneous surface. The linear form of Freundlich isotherm model is given in equation 2.3. In this equation, K_f and n are the Freundlich constants.

$$\log Q_e = \log K_f + \frac{1}{n} \log C_e \quad (2.3)$$

To determine the constants K_f and n the linear form of equation can be used to produce a graph of $\log Q_e$ against $\log C_e$.

2.5.2.1 Metals

The pH adjusted initial metal ion solutions with concentration between 1 and 50 mg/L were prepared by diluting the 1000 mg/L stock solution. These initial solutions

at different metal concentrations were combined 5 g/L material and agitated a constant temperature for 2 hours. Once the adsorption reached equilibrium, final solutions and material were separated by centrifuging. The metal concentrations of the initial and final solutions were calculated by the results of the analyses performed with AAS. The suitability of the results to Langmuir and Freundlich isotherms were investigated.

2.5.2.2 Dyes

The pH adjusted initial dye solutions with concentrations between 5 and 500 mg/L were used. These solutions at different concentrations were combined with 0.5 g/L material and agitated at a constant temperature for 24 hours. Once the adsorption reached the equilibrium final solutions and material were separated by centrifuge. The amount of dye in the initial and final solutions was determined by UV-Vis spectrometer. The structure of the used dyes; MB ($C_{16}H_{18}ClN_3S$), CV ($C_{25}H_{30}ClN_3$), and RB ($C_{28}H_{31}ClN_2O_3$) are illustrated in Figure 2.4 [72].

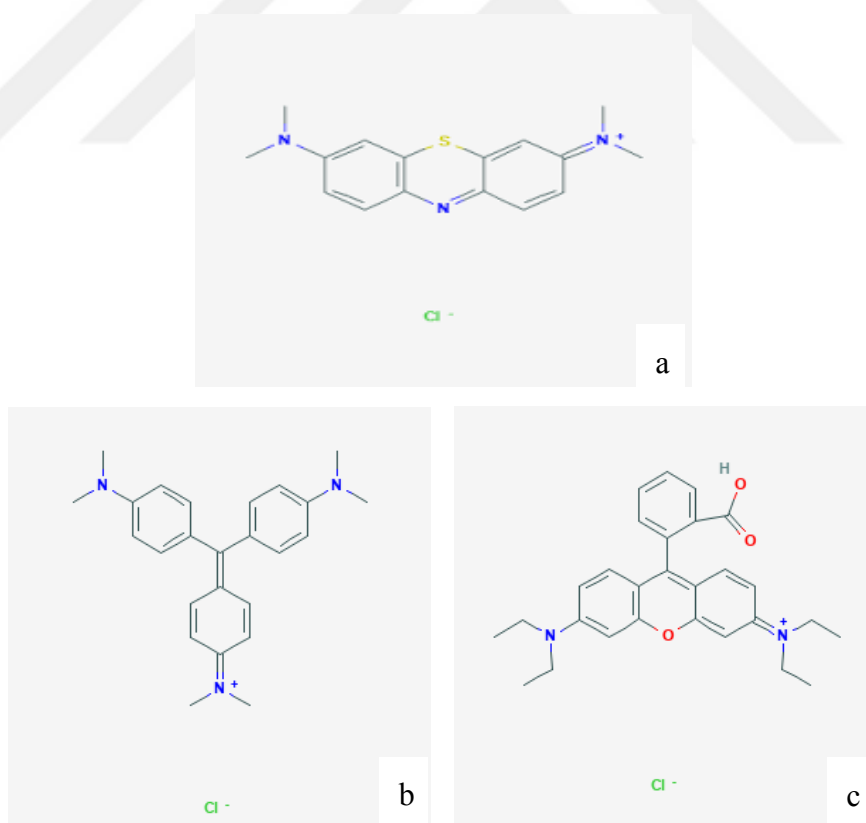


Figure 2.4 : Structure of the a) MB, b) CV, and c) RB.

2.5.3 Dye mixture

In order to understand whether the SiOC samples show selectivity in adsorption, a mixture of dyes was prepared so that the concentration of each dye (MB, CV, and RB) was set to 25 mg/L. 0.005 g of L3HF sample was weighed, 10 mL of the dye mixture was added and agitated for 1-24 h. The final solutions separated from the L3HF by centrifugation. Initial and final concentration of MB, CV, and RB in the mixture were analyzed and the adsorption yield values of L3HF were calculated.

2.5.4 Regeneration of SiOC

The regeneration of samples was tested both by thermal treatment and, by chemical extraction with ethanol. For both techniques 200 mg/L MB solution at pH 8 with 0.5 g/L L3-HF were used as described in section 2.5.2.2.

For the extraction of MB with solvent, ethanol at pH 2 was found to be comparing to ethanol at different pH values (2-10). To investigate the efficiency of ethanol regeneration, extracted and adsorbed MB amount was calculated. The regenerated L3HF was washed with 0.1 M NaOH solution, rinsed with DI water and dried at RT. The used samples were reloaded with MB solution under the same conditions (SiOC-HF dose 0.5g/L and MB solution concentration 200 mg/L at pH8) and regenerated again. This extraction and re-loading process were repeated 3 times.

For the thermal method, the MB loaded SiOCHF sample was heat treated at 400 °C for 20 minutes, the sample was washed with DI water and dried. The dried L3HF sample was stirred with MB solution for 24 hours. The adsorption/desorption process was repeated 3 times in both regeneration methods.

2.5.5 Industrial wastewater

To understand of adsorption behaviour of SiOC sample, actual wastewater was collected from the industrial wastewater treatment centre. 50 mg/L of each dye was added to wastewater which already contains high amount of suspended solids and heavy metals. The L3HF sample was weighed to be 5 g/L for metal absorption tests and 0.5 g/L for dye absorption. Initial solutions and sample were stirred (2 hours for metal contaminants and 24 hours for dyes) as applied in previous experiments. Initial and final solutions were separated and analyzed as described in batch adsorption assays.

2.5.6 Characterization of saturated SiOC

For the characterization of the dye loaded-SiOC, L3HF sample was agitated separately with dye solutions at 500 mg/L concentration at optimum pH. Samples both before and after the treatment with the dye were analyzed by FTIR, SEM and EDX.



3. RESULTS

3.1 Characterization of SiOC

3.1.1 SiOC foams

L1 sample before and after the pyrolysis can be seen in the Figure 3.1. It is clear from the images that sample exhibited high amount of shrinkage. Besides the top portion has bigger pores compared to bottom portion, such difference can be seen especially in thermoset sampels.

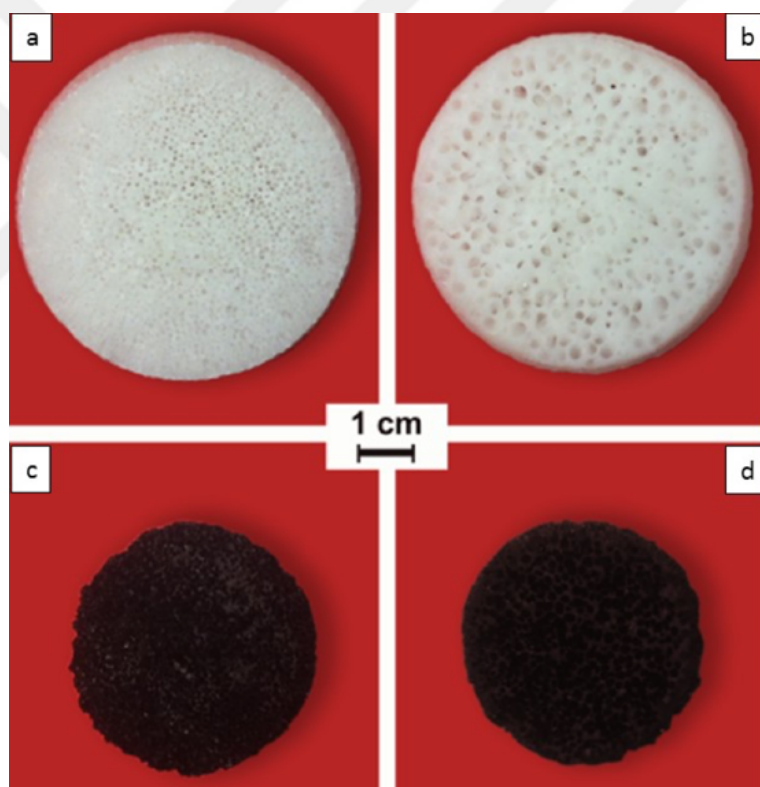


Figure 3.1 : Digital photographs from **a)** the bottom side of the thermoset, **b)** the upper side of the thermoset **c)** the bottom side of the pyrolyzed, and **d)** the upper side of the pyrolyzed sample L1.

Data from ^{29}Si NMR analysis applied to L1 and L3 samples are given in Table 3.1, whereas spectra are shown in Figure 3.2. Three main Si sites can be seen from the spectra. D site (at 22 ppm, C_2SiO_2) is due to the hydrosilylation reaction between the Si-H groups of PHMS. The D^{H} sites (at 32-36 ppm, CSiO_2) are present in the starting

PHMS precursors and their presence in the crosslinked precursor indicate the incomplete consumption of the starting Si-H bonds.

Site T (at 64 ppm, CSiO_3) indicates that the transformation of Si-H bonds into Si-O bonds during the polymer crosslinking.

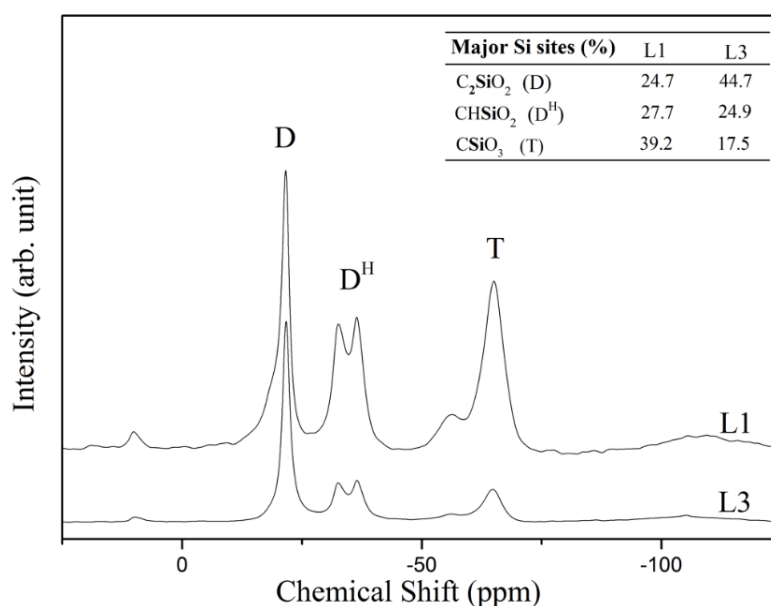


Figure 3.2 : ^{29}Si MAS-NMR spectra of L1 and L3.

L3 sample contains 4 times more PDMS compared to L1, more D unit due to the hydrosilylation reaction.

Table 3.1 : Chemical shift peaks of the sample L1 and L3.

Alan %		Chemical Shift (ppm)	Units
L1	L3		
1.9	1.7	10.3	M
8.9	-	-19.3	D
15.8	44.7	-21.7	D
12.1	14.6	-32.6	D^{H}
12.9	13.0	-36.5	D^{H}
6.7	5.2	-56.1	T2
25.5	12.3	-64.9	T3
13.7	11.2	-108.0	Q4

Weight, thickness and average diameter of SiOC samples before and after pyrolysis are given in the Table 3.2.

Table 3.2 : Data before and after pyrolysis in L series samples.

Sample	Before Py			After Py			Weight loss %
	Average d. (cm)	Average thickness (cm)	Average weight (g)	Average d. (cm)	Average thickness (cm)	Average weight (g)	
L1	5.00	1.40	9.92	3.70	1.00	6.31	36.38
L2	5.10	2.00	17.92	3.50	1.40	7.99	55.38
L3	5.80	2.80	25.85	3.80	1.60	8.05	68.86

As can be seen from the Table 3.2, with the increase in the amount of PDMS in the sample, weight loss rises. As the amount of PDMS increases, the porosity also increases. SEM images of the pyrolyzed L1 sample are given in Figure 3.3 (a-e).

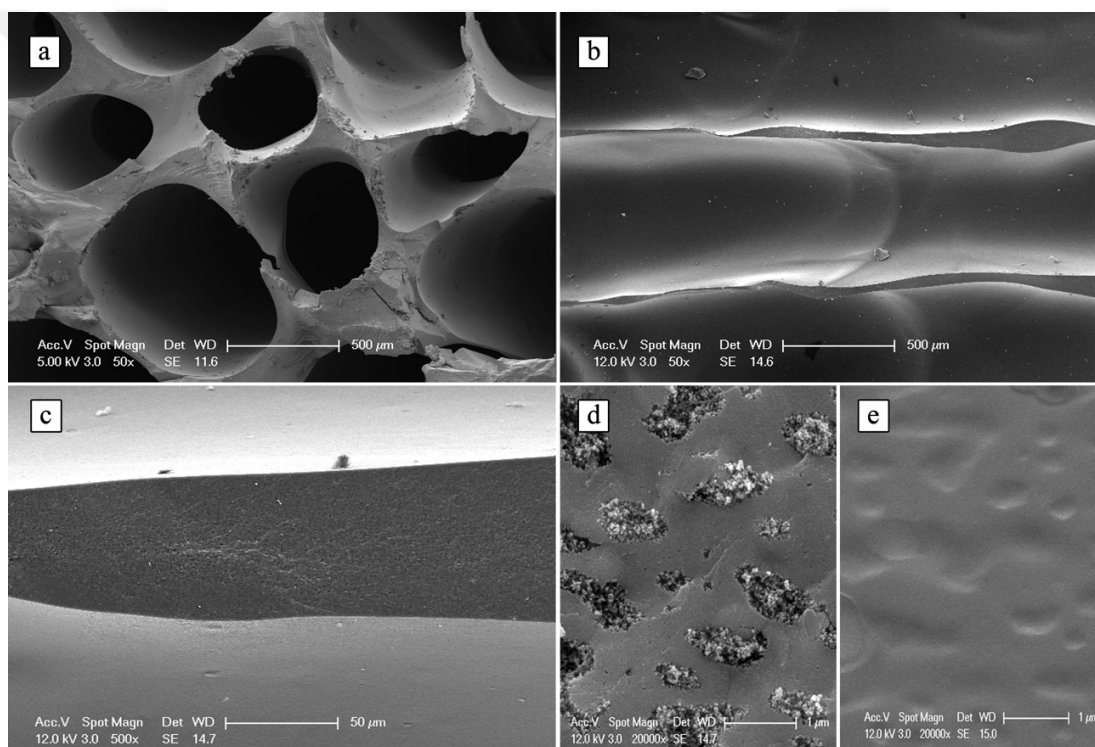


Figure 3.3 : SEM images of, **a)** pores from the upper side, **b)** cross section of channels **c)** channel strut, **d)** surface detail, and **e)** higher magnification of pore surface of the pyrolyzed L1 sample

The channels from the top of the sample were formed generally larger than 500 μm . Aligned channels were separated by struts in the 50-100 μm range (Fig. 3.3 (b,c)), have pores with around 1 μm diameter (Fig.3.3 (d)) and have dense channel surfaces (Fig. 3.3 (e)).

Tomographic two-dimensional images of L series samples are given in Figure 3.7. As can be seen in the radial (R) slices images, the channels are circular at the centre

and there are elongations to the edges. On the other hand, in the axial (A) slices images, it can be seen that the aligned channels are connected to one another at the top and bottom of the sample. It is observed that the channels are merged and their cross-sectional area increased from the bottom to top which can be the outcome of the coalescence of gas bubbles while curing.

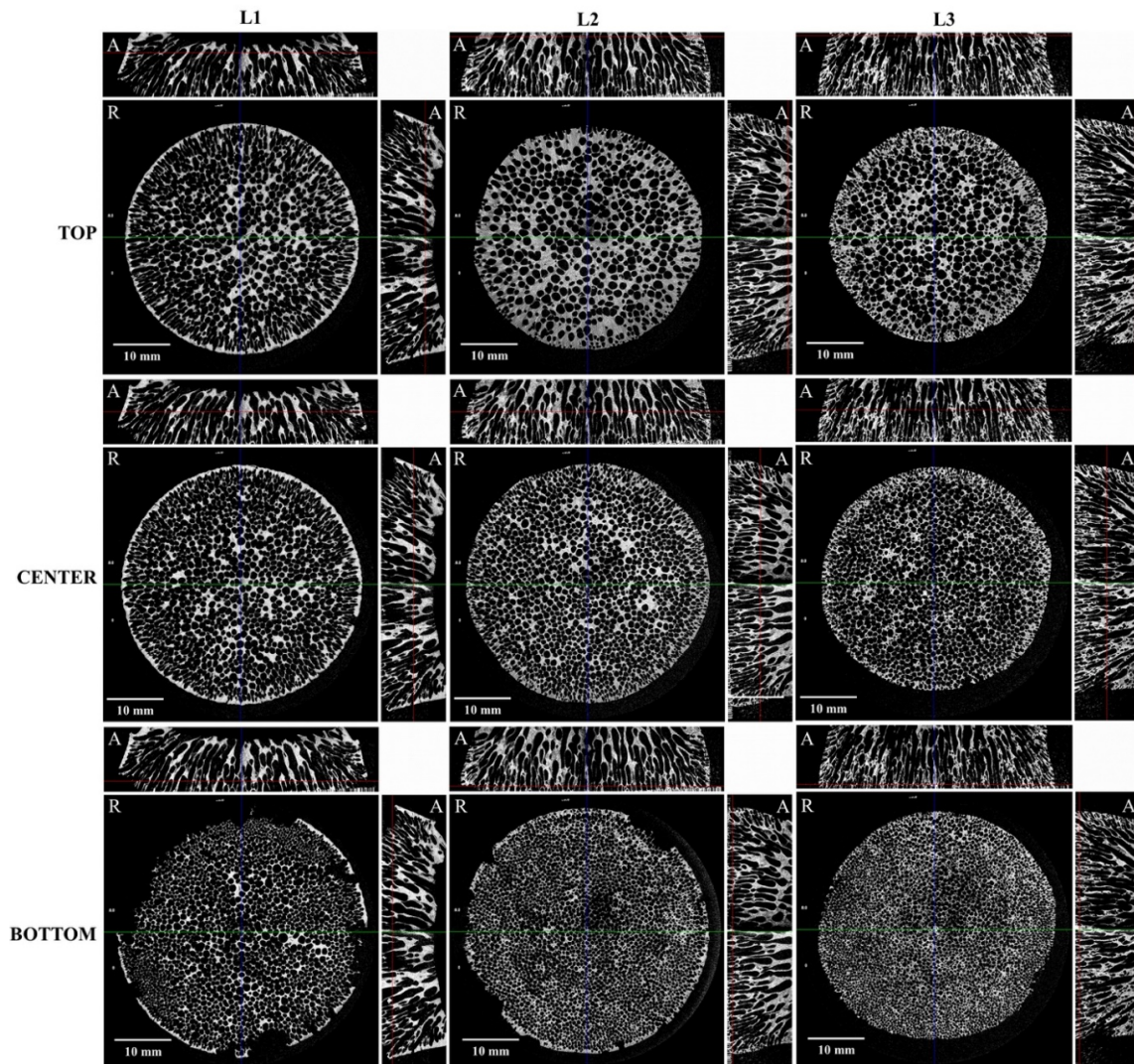


Figure 3.4 : Tomographic 2D images of radial (R) and (A) slices at the top, center and bottom of L1, L2 and L3 samples.

Pore count from radial slices for L3 sample is shown in Figure 3.5. The Feret's diameter, defined as the average distance between the tangent pairs parallel to the projected edges of the sample, was used to determine the cross-sectional channel size in the 2-D images. As for the same analysis area (1003 mm^2), the pore amount decreased from the bottom to the upper side of the sample due to merged channels from 2774 to 1079, and the channel diameter distribution reached high values.

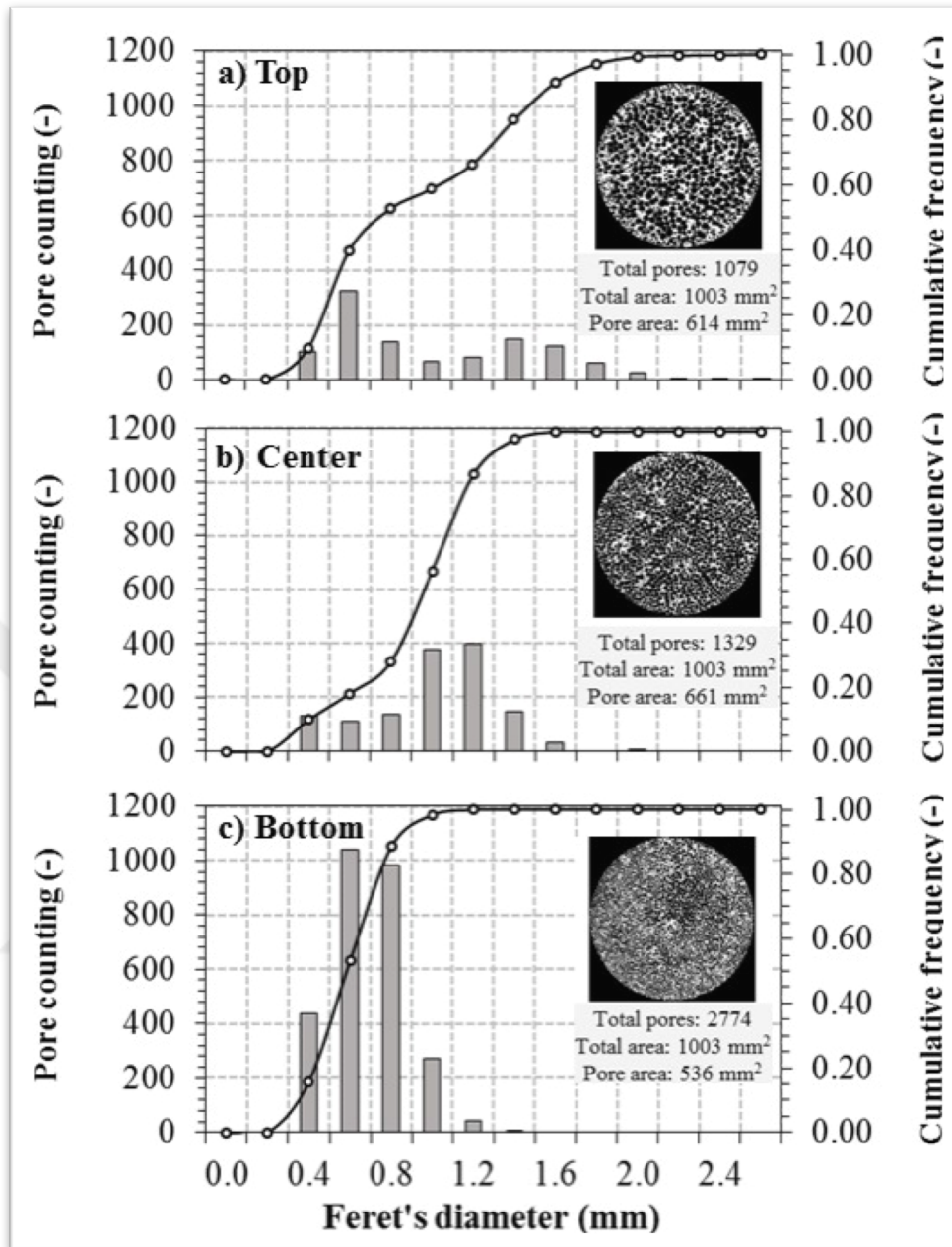


Figure 3.5 : Pore diameter distributions of radial tomographic slices of L3 sample.

From bottom to top, pore areas increased, indicating that the rising gas bubbles during curing are not only merging but also expanding at the same time. Similar results can also be mentioned for the L1 and L2 samples. In Figure 3.6 the average channel diameters of these samples are given.

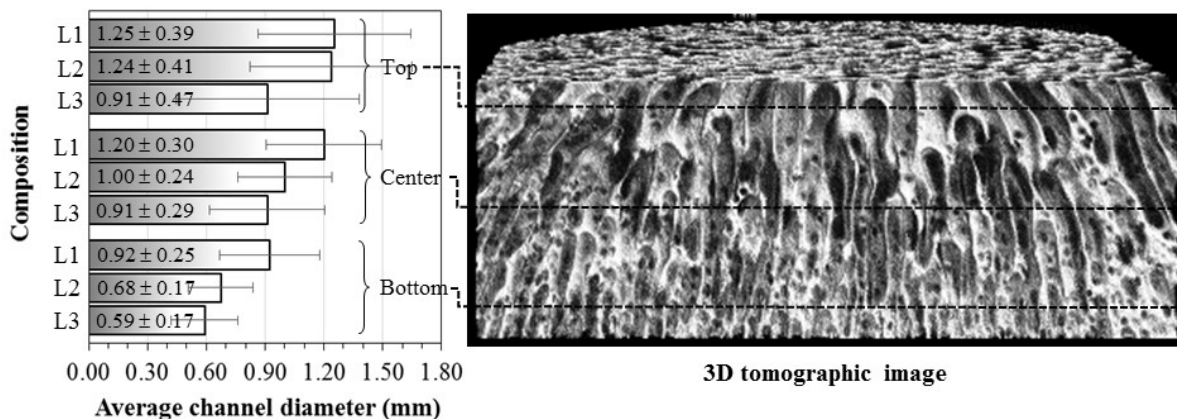


Figure 3.6 : Average channel diameters from the top, centre and bottom of samples L1-L3.

In the 3D image given in Figure 3.6, it is possible to observe a large number of small round pores connecting these channels along adjacent vertical channels.

Briefly, the L1-L3 sample series were produced by using different amounts of PDMS, PHMS and cyclic. The resulting samples have an average diameter of axial channels in between 0.59 to 1.25 mm, high surface area (before etching; 121.9 m²/g) and open pores (up to 83%).

The pore size distributions of those monolithic samples from mercury porosimetry test are given in Figure 3.7. As can be seen, the samples have different sized pores, but they are essentially bi-modal, usually being of larger than 10 μm and less than 0.1 μm.

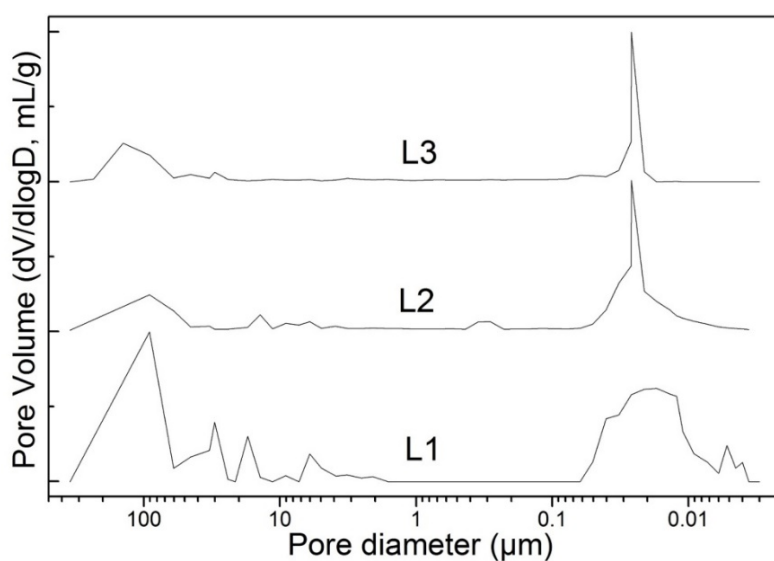


Figure 3.7 : Mercury porosimetry results of the SiOC samples.

L1-2-3 samples are macro-porous (> 50 nm). The surface area increases with PDMS and a similar situation has been observed in the literature before [65]. Table 3.3 shows N_2 adsorption results of SiOC samples.

Table 3.3 : The N_2 adsorption test results of SiOC samples.

Sample	BET (m^2/g)	Micropore volume (cm^3/g)	Pore volume (cm^3/g)	
			BJH Adsorption cumulative volume of pores	BJH Desorption cumulative volume of pores
L1	4.29	0.00	0.02	0.02
L1HF	773.66	0.36	0.43	0.44
L2	48.61	0.00	0.22	0.22
L2HF	704.39	0.23	0.65	0.66
L3	121.89	0.00	0.47	0.47
L3HF	663.11	0.14	0.57	0.58

The surface areas, average pore sizes, and the isotherms given in Figure 3.8 (a) are very similar for all etched samples. All samples showed a surface area of about $700 m^2/g$ after etching, with an average pore diameter of about 3-5 nm.

The N_2 adsorption/desorption isotherms and pore size distribution graphs of the sample before and after HF etching are given in Fig 3.8.

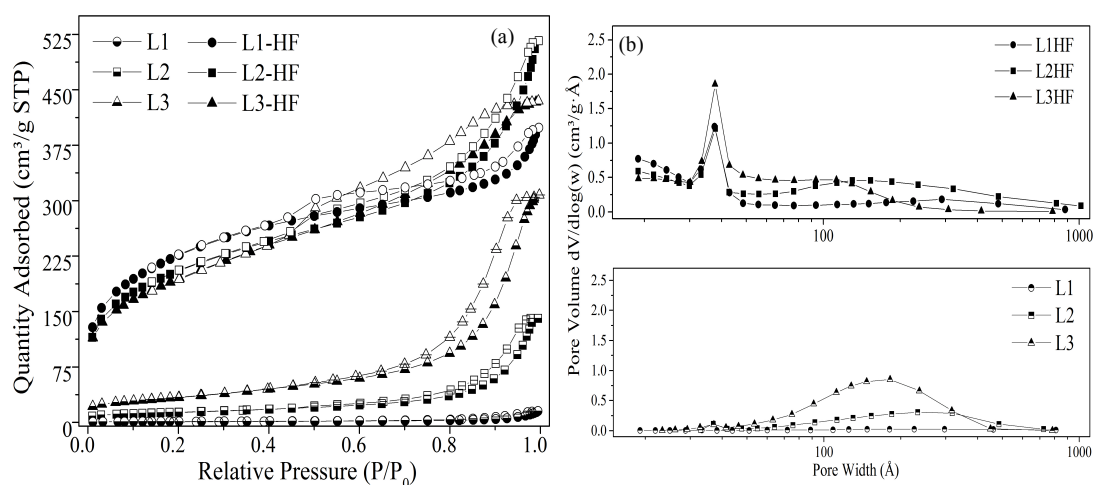


Figure 3.8. Samples L1-L3 a) N_2 adsorption/desorption isotherms and b) pore size distribution curves.

As can be seen from the isotherm graphs, while the hysteresis grows, (i.e. as the size of the meso-pore increases), the surface area is increased due to additional micropores (<2 nm). Similar results can be seen from the pore size distribution graphs before and after etching.

In addition to increasing the surface area, the morphology of the samples has also changed with the etching process. As seen in Figure 3.9 (a), approximately 10 nm of pores were formed after etching in the sample having a smooth surface prior to etching (see, Fig 3.9 (b)).

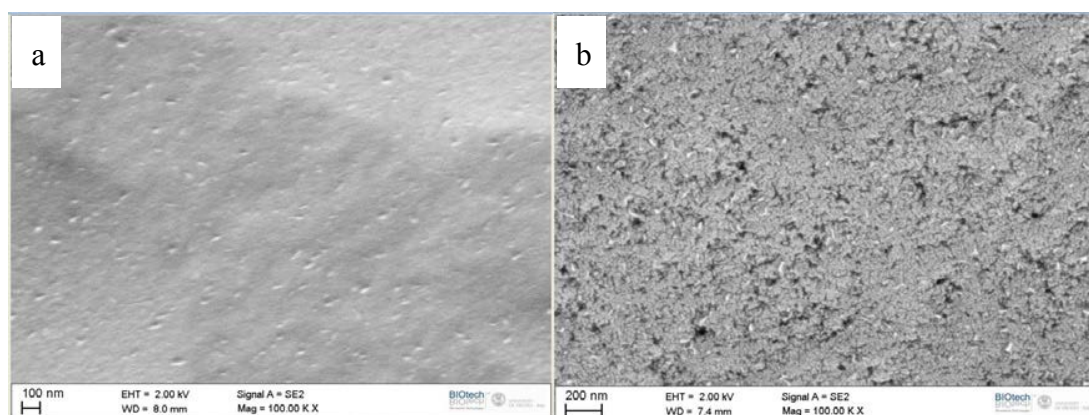


Figure 3.9 : The SEM images of sample L1 **a)** before and **b)** after HF etching.

3.1.2 SiOC beads

Approximately 100 microns diameter non-porous beads were produced with o/w emulsion while w/o/w emulsion method resulted in larger diameter (mm range) porous beads. The optical microscope image and SEM image of non-porous beads produced by o/w emulsion method are given in Figure 3.10.

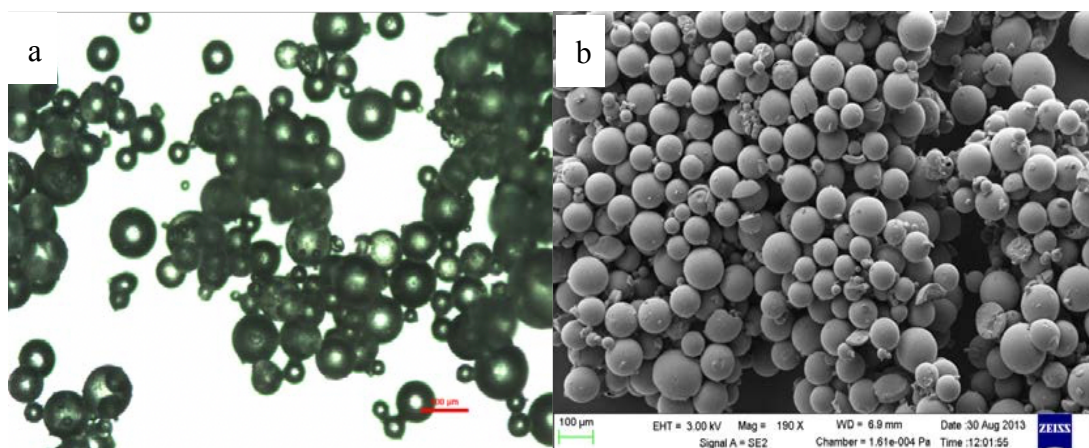


Figure 3.10 : **a)** The optical microscope image (100 µm scale), **b)** SEM image of non-porous beads produced by o/w emulsion method.

Figure 3.11 (a and b) show pre-etching structures of samples produced, while Figures 3.11 (c and d) show microstructure resulting from HF etching. As can be seen from Figures 3.11 (c and d), pore size and porosity were increased after the HF process. Although the microstructure of the sample was altered via etching, the main geometry remained the same.

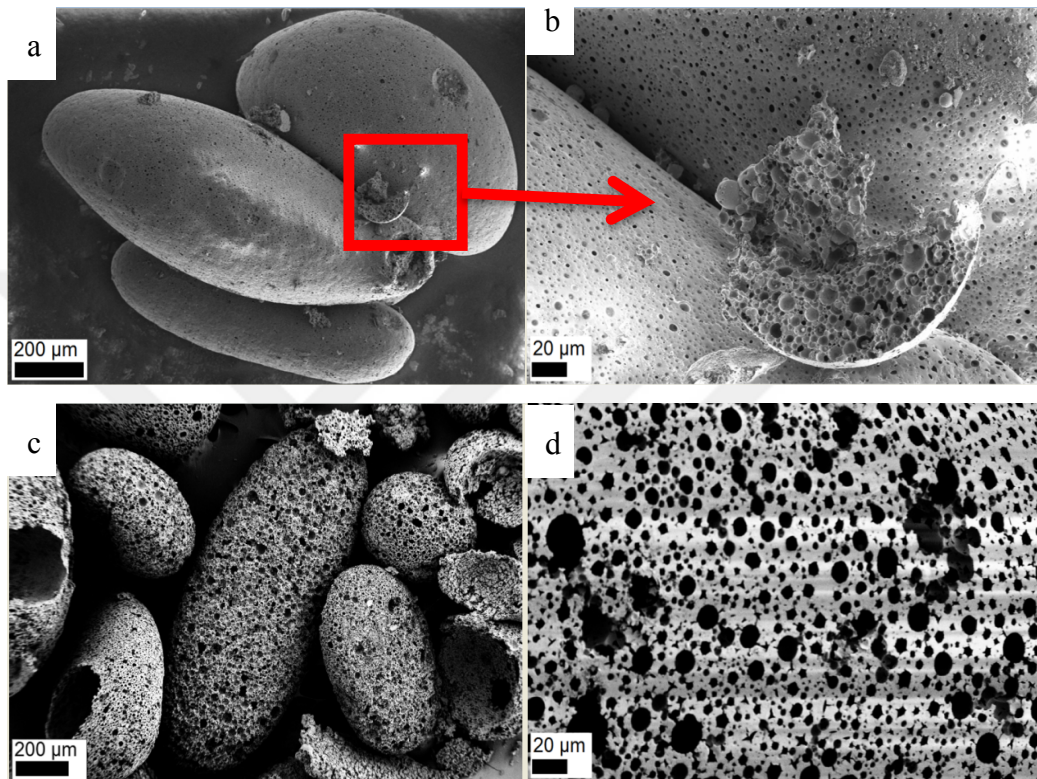


Figure 3.11 : SEM images are taken from SiOC bead sample **a-b)** before the etching and **c-d)** after the etching.

The structural changes of these samples as shown in Figure 3.12, were investigated by XRD, FTIR and RAMAN.

Figure 3.12 (a) shows that the structure before and after HF etching is amorphous.

There is no clear difference in XRD data before and after etching.

Figure 3.12 (b) in the FTIR data after HF etching 3650 cm^{-1} (Si-OH) band increased in intensity and $\sim 930\text{ cm}^{-1}$ Si-OH associated with a new band occurred (All data are normalized). Si-OH structures of HF treated SiOC ceramics were similarly observed in the literature [73]. As seen in Raman data given in Figure 3.12 (c), it is possible to state that the carbon in the SiOC matrix reached a more regular structure after etching.

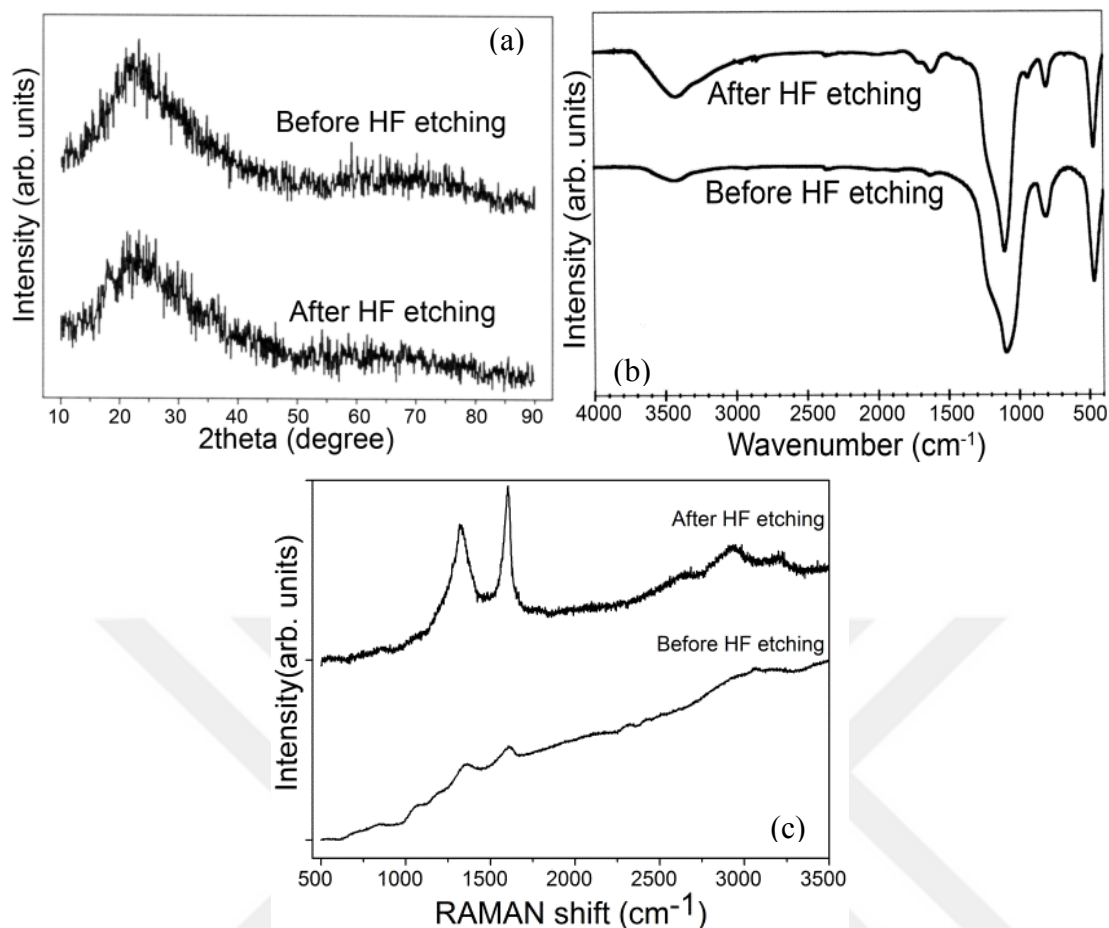


Figure 3.12 : SiOC bead samples produced with W/O/W method (before and after etching) **a)** XRD, **b)** FT-IR and, **c)** RAMAN results.

3.2 Characterization CSH/CS

3.2.1 CSH powder

XRD plots are given in Figure 3.13 for XRG 41-44 and XRG 71-74 (The data of pure CaCO₃, Ca(OH)₂ and Tobermorite (Ca₅Si₆O₁₆(OH)₂·4H₂O) are collected from The International Centre for Diffraction Data (ICDD) is given for comparison.).

While the Ca/Si ratio was increased from 0.83 to 1.13, no significant change was observed between XRG71-72 samples (ball milled) and some differences between XRG41-42 samples (without ball milling).

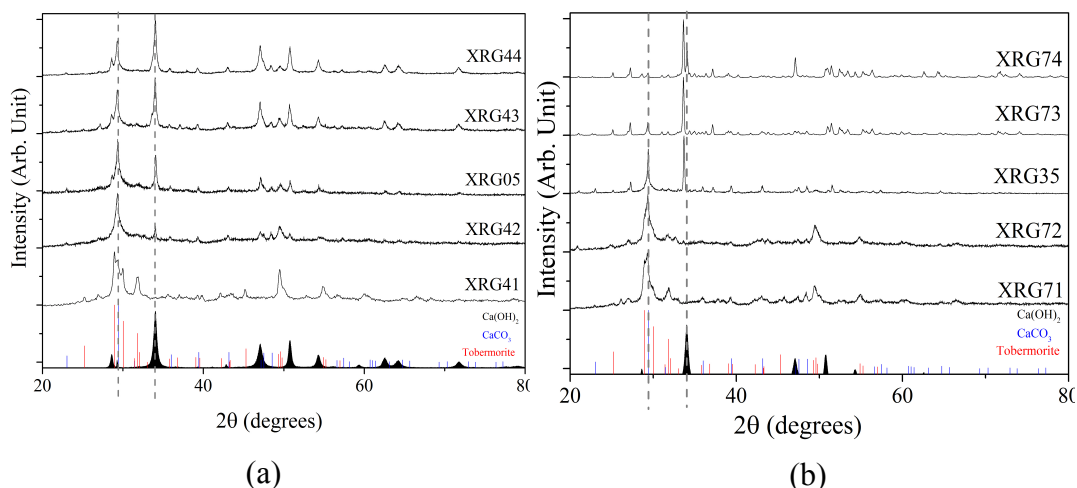


Figure 3.13 : XRD plots of the samples produced **a)** without ball mill **b)** with ball mill 10h/250 rpm.

When XRG41 and 42 samples were compared in Figure 3.13 (a), it can be seen that a peak $2\theta \sim 32$ degrees disappears and the one around 30 degrees (2θ) become single peak. However, the new peaks at 34, 47 and 50 degrees (2θ) are probably caused by portlandite ($\text{Ca}(\text{OH})_2$) crystals. In the XRG41-44 set (without ball milling), the relative intensity of the new portlandite-derived peaks was increased as the Ca/Si molar ratio increase. In the case of ball mill series (XRG71-74), new portlandite peaks were not clearly observed until the ratio of Ca/Si was increased to 3. The results of TGA/DTA analyses are shown for samples with a Ca/Si ratio of 1.5 and higher, see Figures 3.14, 3.15, and 3.16.

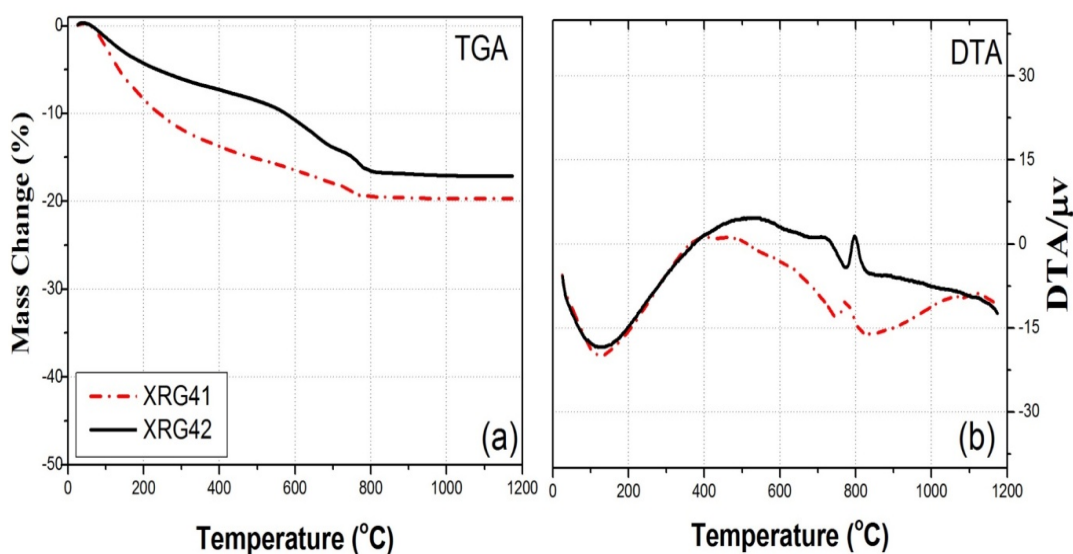


Figure 3.14 : a) TG and b) DTA plots of XRG41 and XRG42.

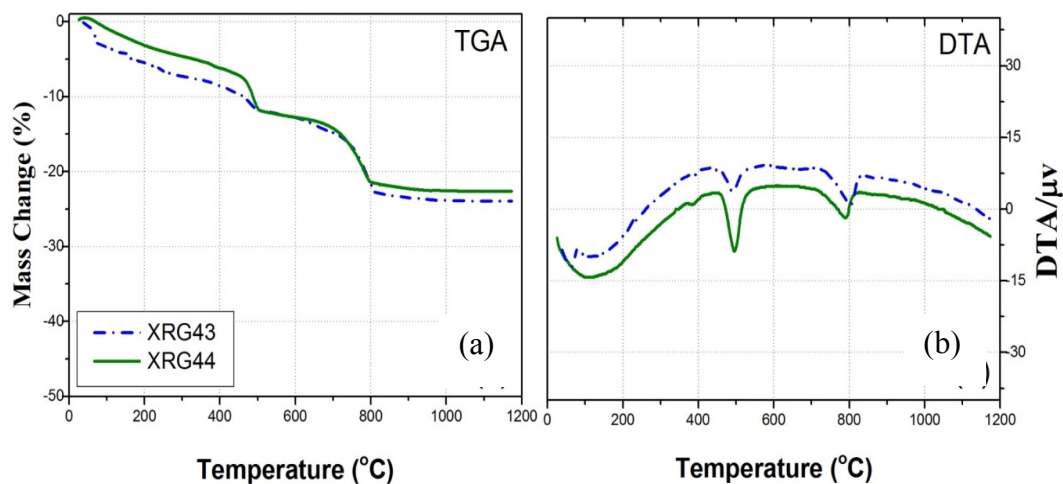


Figure 3.15 : a) TG and b) DTA plots of XRG43-44.

The TG/DTA results for XRG71-74 (Figure 3.16) are quite similar to the XRG41-44 set, shown in Figure 3.14.

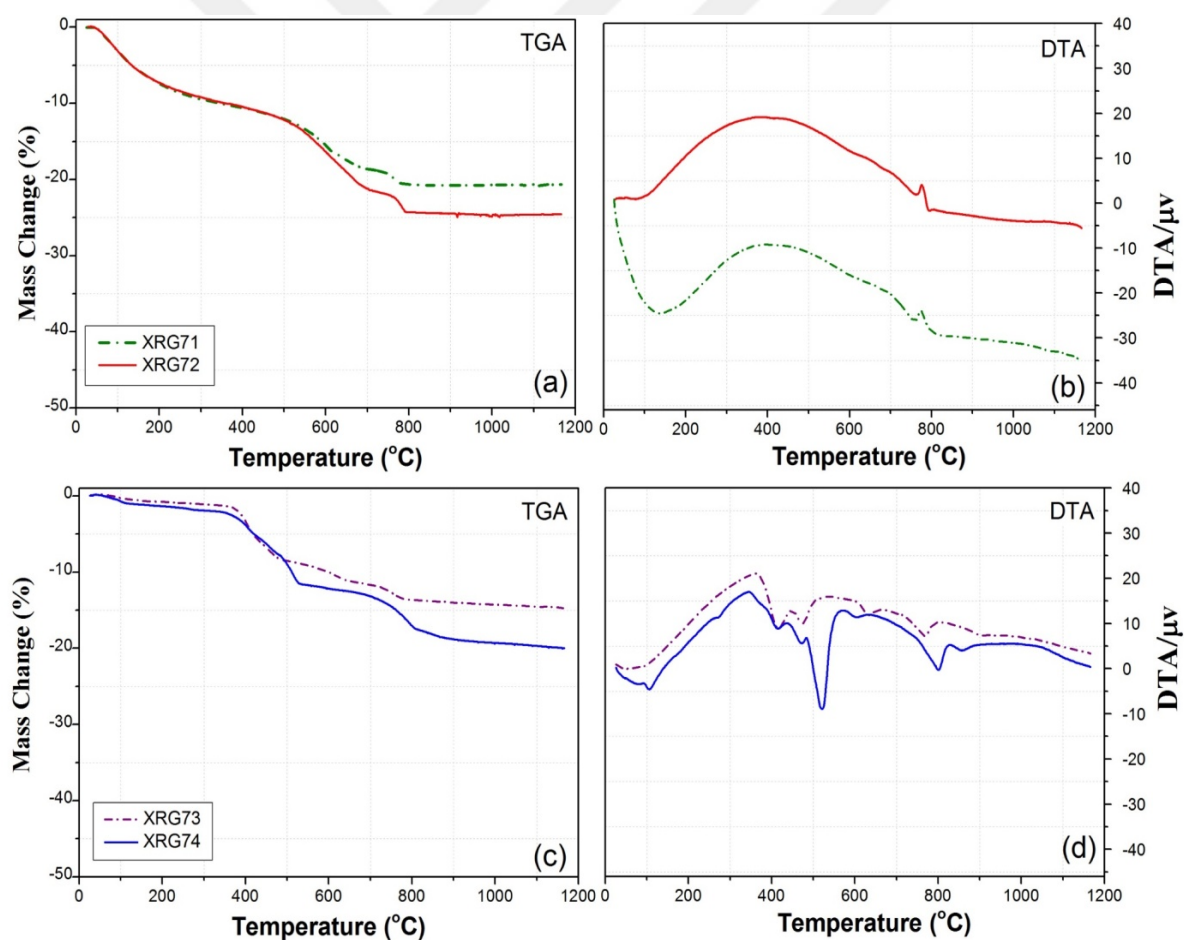


Figure 3.16 : a) TG and b) DTA plots of XRG71-74.

As can be seen from Figure 3.17 (a-d), the samples in the XRG41 (no ball-milled), where the Ca/Si ratio is 0.83, consist of two different microstructural products: (i)

nano-thick fibre structures and (ii) agglomerations around 15 microns formed by the flake-like structures.

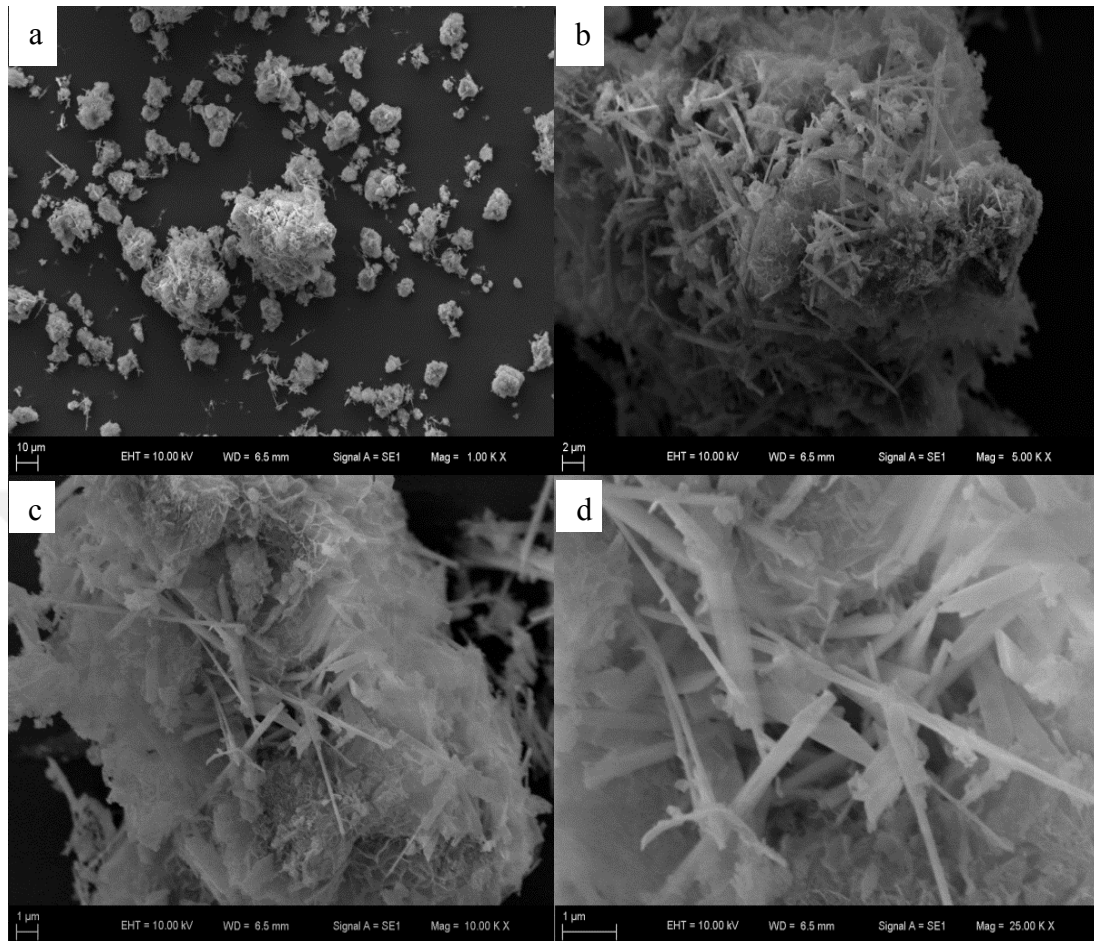


Figure 3.17 : SEM images of sample XRG41 with different magnifications.

The microstructures of XRG42 can be seen in SEM images at Figure 3.18 (a-d). At low magnification (Fig 3.18 (a)) the micro structure is similar to the previous sample (XRG41 see, Fig 3.17). However, when the magnification is further increased, some differences between the microstructures of samples XRG41 and XRG42 were observed. The fibrous structures existing in sample XRG 41 were not observed in this sample, and the sample was formed by mostly flake-like structures (see, Fig 3.18 (c,d)).

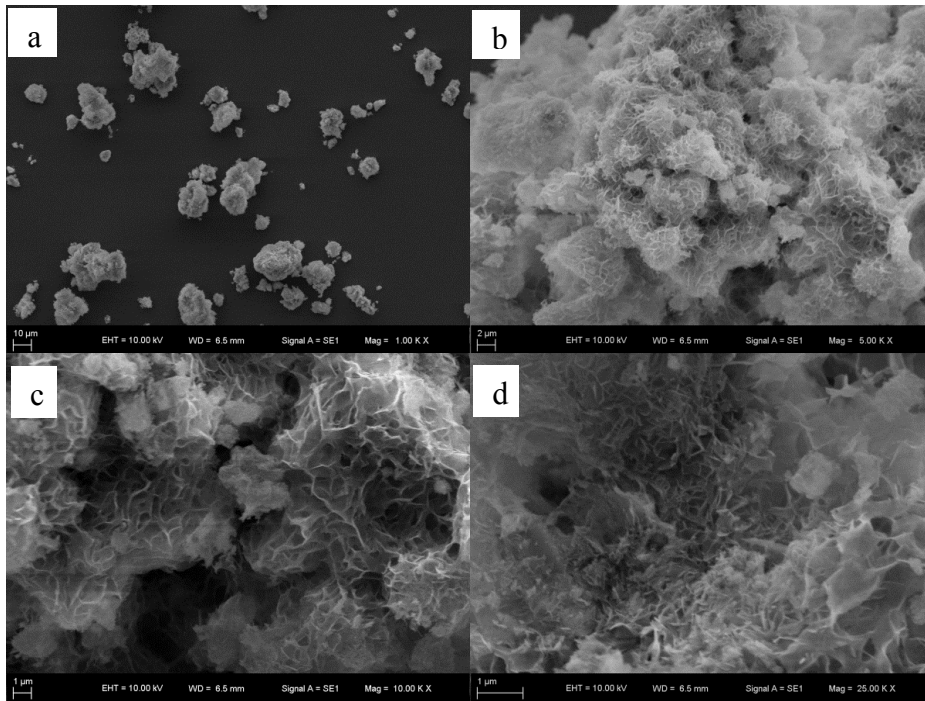


Figure 3.18 : SEM images of sample XRG42 with different magnifications.

The microstructure of the sample XRG43(Ca/Si = 2.13 and no-ball milling) is shown in Figure 3.19 (a-d). Similar microstructures can be seen from SEM images. Although in some regions, lath-shaped crystals are observed (Figure 3.19 (b)), the sample has essentially flake-like formations.

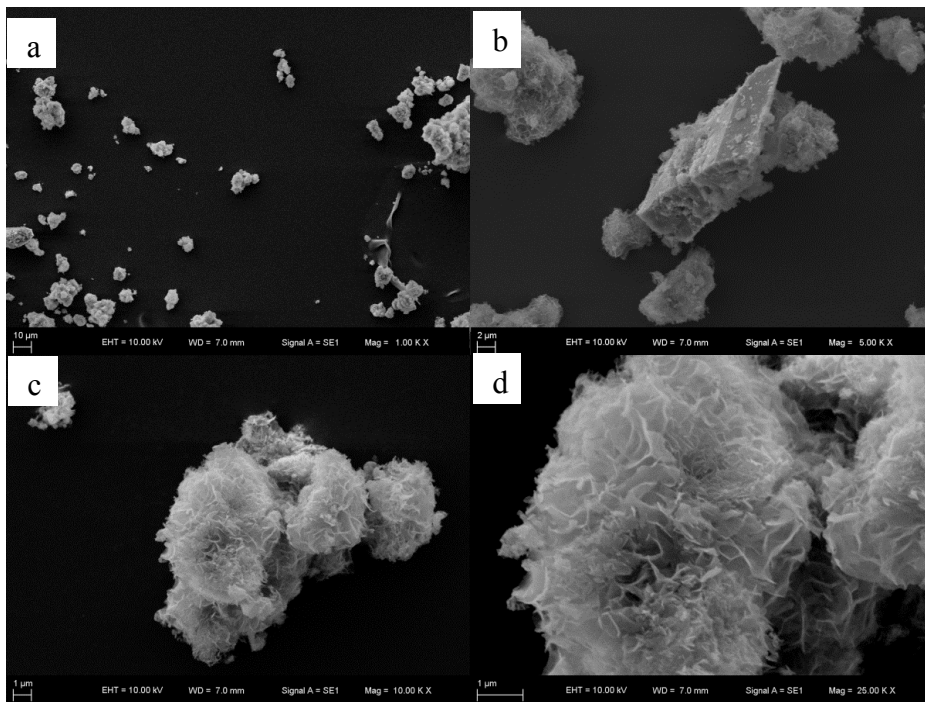


Figure 3.19 : SEM images of sample XRG43, **a)** low magnification, **b** and **c)** higher magnification **d)** flake-like structure detail.

The microstructure of the sample XRG44 (Ca/Si = 3.12 and no-ball milled) was shown in Figure 3.20 (a-d). The microstructures of XRG44 and XRG43 are very similar, which is an agglomerate formed from flake-like structures.

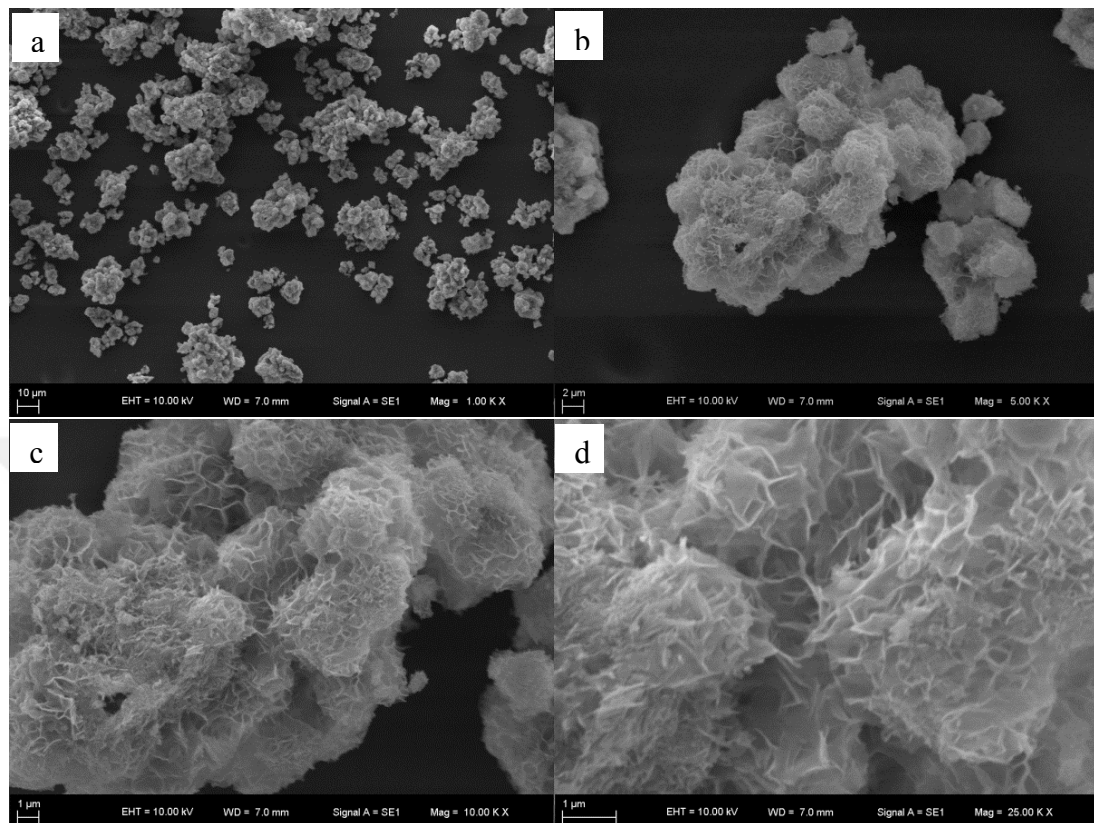
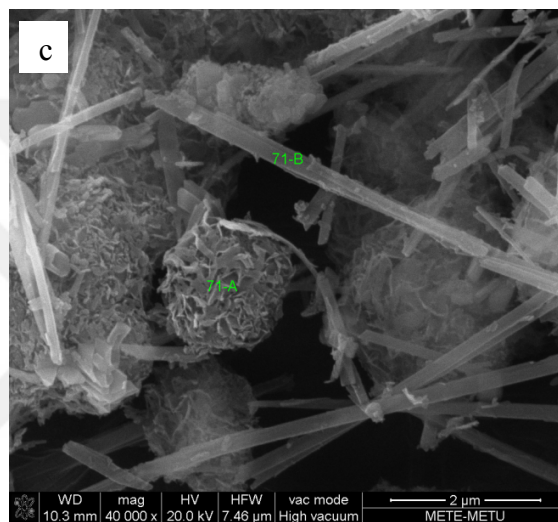
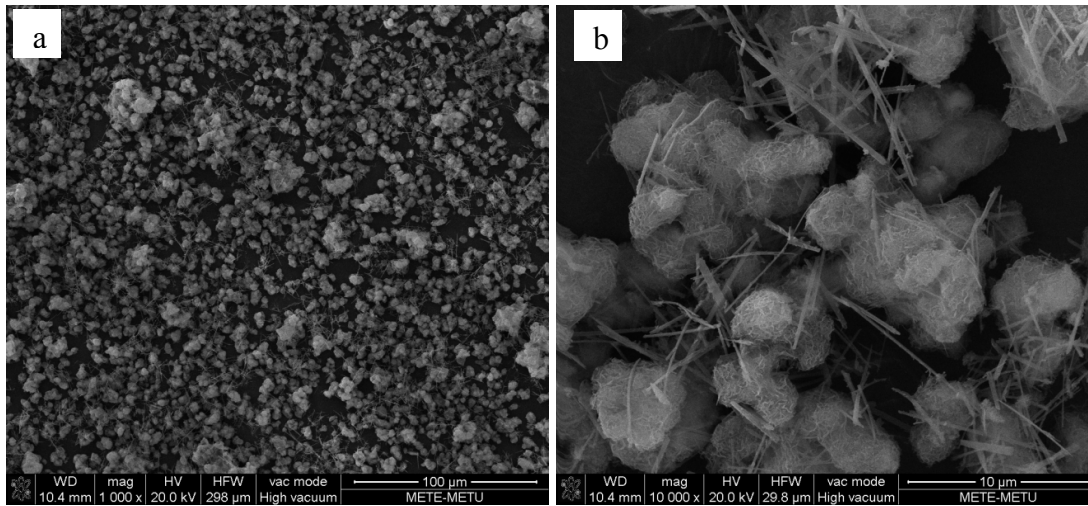


Figure 3.20 : SEM images of sample XRG44, **a)** low magnification, **b** and **c)** higher magnification **d)** flake-like structure detail.

The microstructure of the sample XRG71(Ca/Si = 0.83 and ball milled) was shown in Figure 3.21 (a-c).

The sample consists of two different microstructural products (nano-thick fibres and agglomeration of 1-15 microns formed by the flake-like structures) similar to the previous observations. EDS analyses were taken from these structures and results were given in Figure 3.21 (d).

The microstructure of the sample XRG72(Ca/Si = 1.13 and ball milled) is shown in Figure 3.22(a-c). While the fibre existing in the previous sample turned to wider lath-type structures, flake-like structures are also visible. The EDS analyses were taken from these structures and results are given in the Figure 3.22 (d).



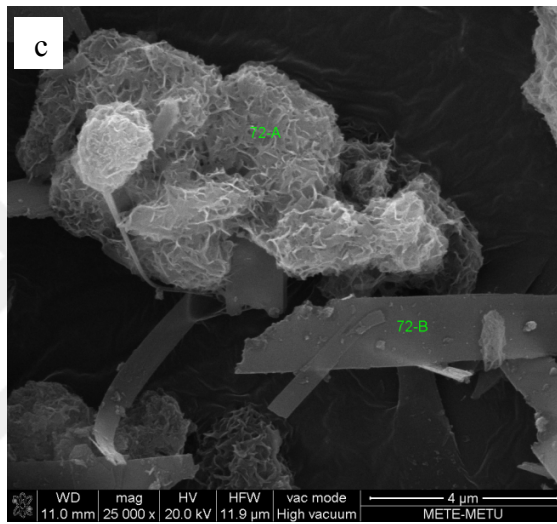
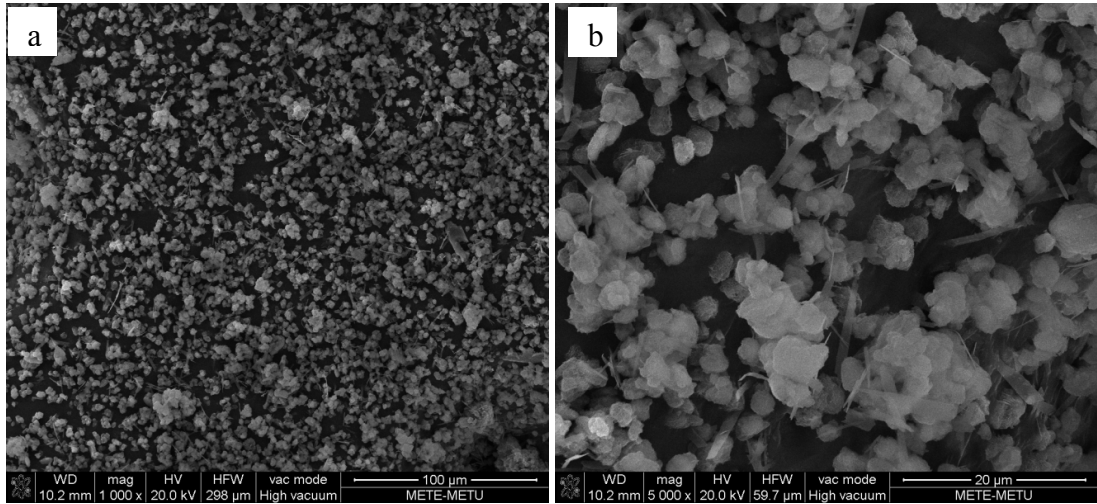
Element	Wt %	At %	K-Ratio	Z	A	F
NaK	4.57	6.21	0.0192	0.9876	0.4225	1.0066
MgK	5.55	7.14	0.0302	1.0122	0.5315	1.0113
AlK	1.26	1.46	0.0078	0.9823	0.6143	1.0206
SiK	48.13	53.60	0.3555	1.0108	0.7277	1.0043
CaK	40.49	31.59	0.3510	0.9845	0.8806	1.0000
Total	100.00	100.00				

Element	Net Inte.	Bkqd Inte.	Inte. Error	P/B
NaK	15.02	10.50	5.16	1.43
MgK	23.83	14.37	3.93	1.66
AlK	6.03	16.13	13.24	0.37
SiK	250.18	17.82	0.87	14.04
CaK	158.55	8.55	1.08	18.54

Element	Wt %	At %	K-Ratio	Z	A	F
NaK	3.96	5.48	0.0160	0.9885	0.4056	1.0061
MgK	3.36	4.39	0.0179	1.0131	0.5212	1.0113
AlK	1.80	2.12	0.0114	0.9832	0.6299	1.0207
SiK	46.73	52.95	0.3494	1.0117	0.7357	1.0047
CaK	44.15	35.06	0.3854	0.9856	0.8857	1.0000
Total	100.00	100.00				

Element	Net Inte.	Bkqd Inte.	Inte. Error	P/B
NaK	8.70	7.00	7.07	1.24
MgK	9.83	10.70	7.34	0.92
AlK	6.13	14.20	12.37	0.43
SiK	170.93	16.75	1.08	10.20
CaK	121.02	8.03	1.25	15.06

Figure 3.21 : SEM images of sample XRG71, **a)** low magnification, **b** and **c)** higher magnification **d)** EDS results from agglomerate and fibre structure.



Element	Wt %	At %	K-Ratio	Z	A	F
NaK	4.39	6.20	0.0170	0.9898	0.3900	1.0054
MgK	3.00	4.00	0.0154	1.0145	0.5022	1.0100
AlK	1.18	1.42	0.0073	0.9844	0.6170	1.0187
SiK	41.59	48.04	0.3099	1.0130	0.7314	1.0055
CaK	49.84	40.34	0.4427	0.9871	0.9000	1.0000
Total	100.00	100.00				

Element	Net Inte.	Bkgd Inte.	Inte. Error	P/B
NaK	17.90	12.35	5.05	1.45
MgK	16.33	16.58	5.97	0.98
AlK	7.58	18.09	12.09	0.42
SiK	291.41	19.91	0.87	14.63
CaK	266.43	8.21	0.87	32.45

Element	Wt %	At %	K-Ratio	Z	A	F
NaK	2.94	4.16	0.0114	0.9900	0.3899	1.0056
MgK	2.24	3.00	0.0119	1.0147	0.5158	1.0107
AlK	3.37	4.06	0.0216	0.9847	0.6380	1.0188
SiK	41.91	48.56	0.3099	1.0132	0.7258	1.0054
CaK	49.54	40.22	0.4391	0.9873	0.8978	1.0000
Total	100.00	100.00				

Element	Net Inte.	Bkgd Inte.	Inte. Error	P/B
NaK	4.30	7.40	13.12	0.58
MgK	4.50	10.38	14.42	0.43
AlK	8.03	11.77	9.03	0.68
SiK	104.54	13.65	1.42	7.66
CaK	94.82	7.42	1.43	12.78

Figure 3.22 : SEM images of sample XRG72, **a)** low magnification, **b** and **c)** higher magnification **d)** EDS results from flake-like and thin lath structures.

The microstructure of the sample XRG73 (Ca/Si = 2.12 and ball milled) is shown in Figure 3.23 (a-c). In all magnifications, microstructures are completely different from the previous samples. The lath formations around 50-100 microns, can be seen from SEM images of the sample XRG73. The EDS analyses from the laths (Figure 3.23 (d)) gave a ratio of 2.23 Ca/Si, while the analyses from the agglomerates on the plate (laths) gave a high Mg content and 1.82 Ca/Si ratio.

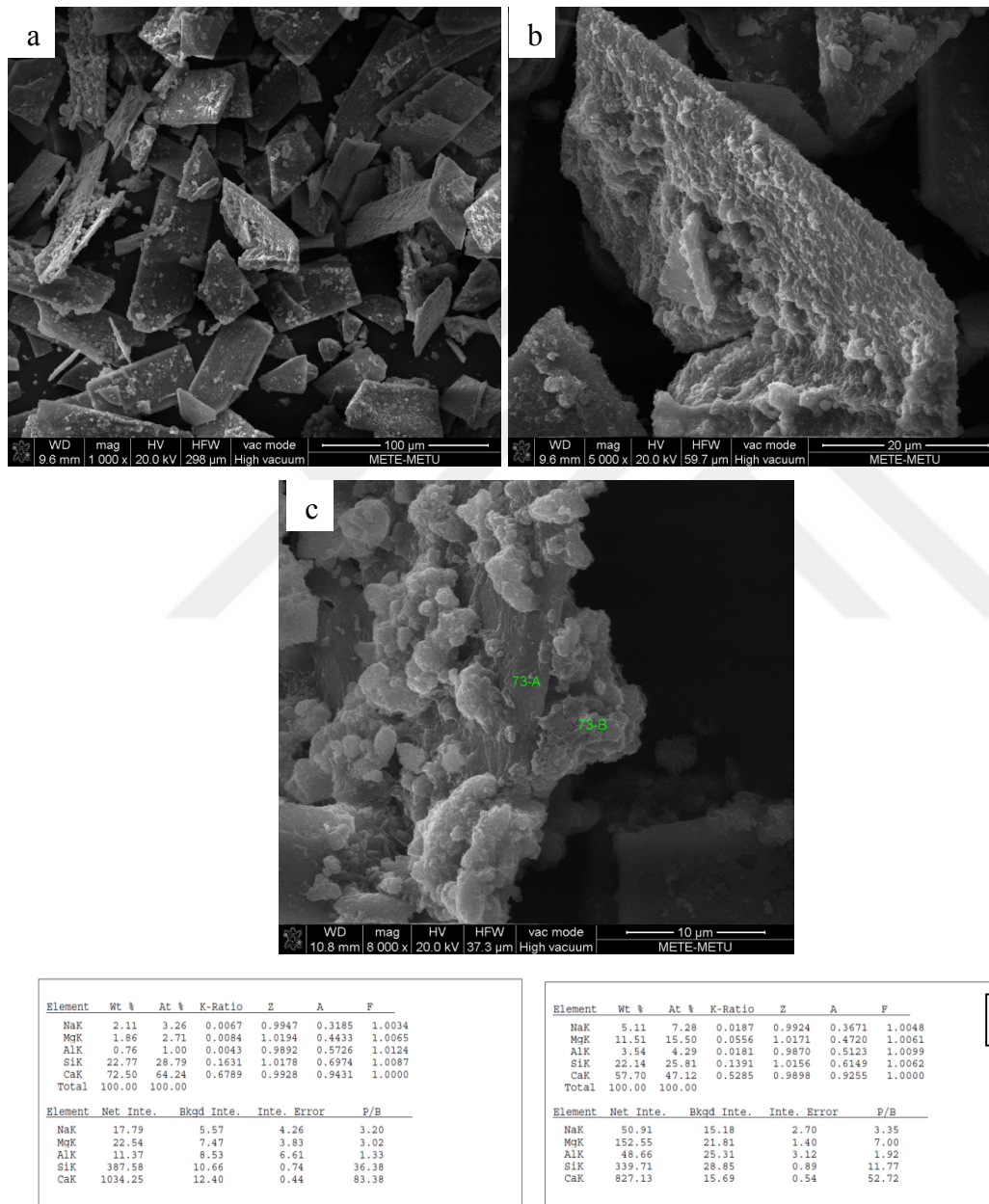


Figure 3.23: SEM images of sample XRG73, **a)** low magnification, **b** and **c)** higher magnification **d)** EDS results from laths structure.

The microstructure of the sample XRG74 (Ca/Si = 3.13 and ball milled) is shown in Figure 3.24.

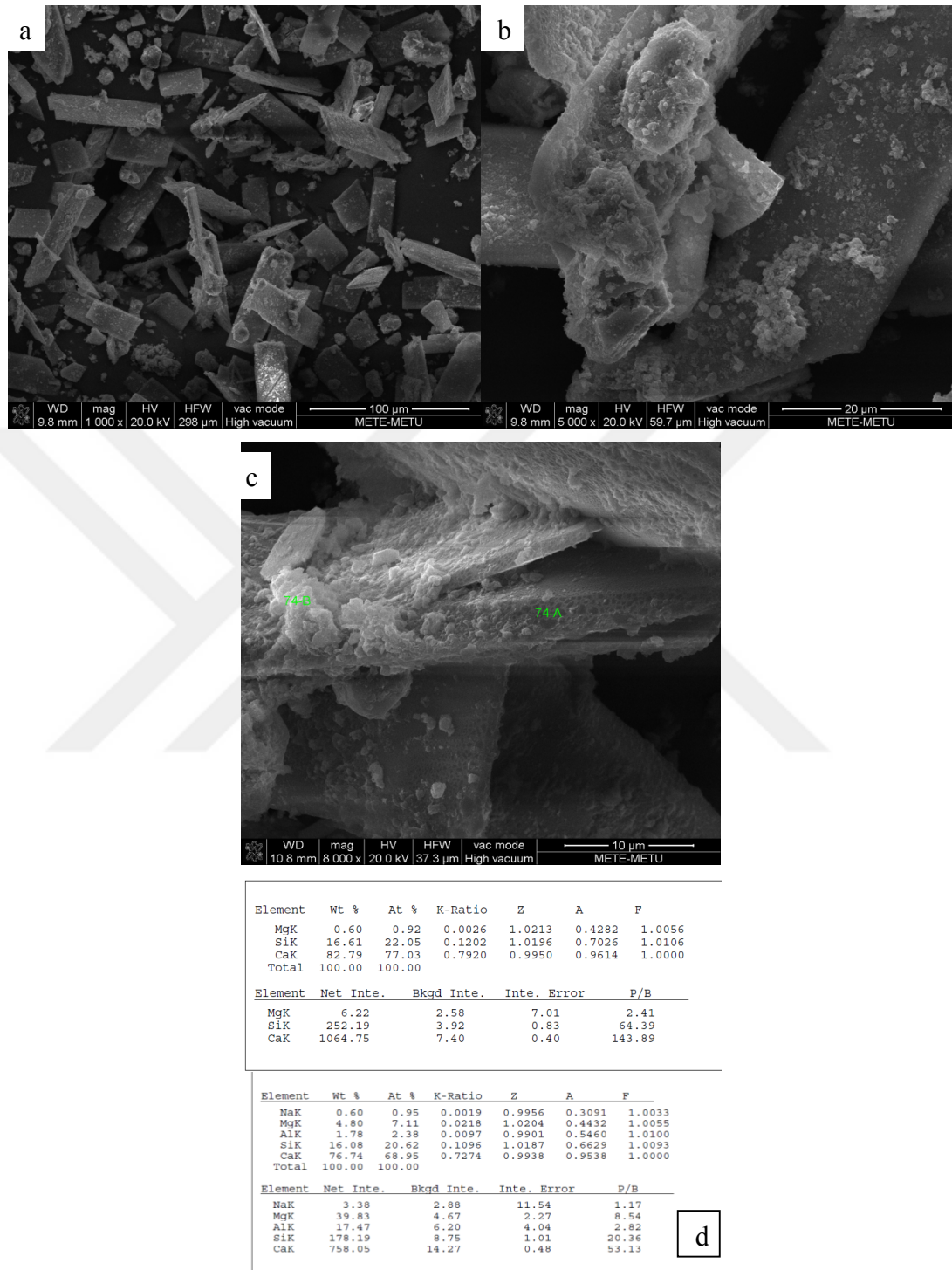


Figure 3.24 : SEM images of sample XRG74, **a)** low magnification, **b** and **c)** higher magnification **d)** EDS results from thin lath structures.

The SEM images taken from the sample XRG74 showed very similar microstructure with the previous sample (XRG73). The EDS analyses from the laths (Figure 3.24

(d)) gave a ratio of 3.49 Ca/Si while the analyses from the agglomerates on the lath gave a ratio of 3.34 Ca/Si and a higher Mg content as in the previous sample (see fig. 3.23).

3.2.2 Monolithic CSH/CS

3.2.2.1 Gelation

SEM images of Alginate1 and Alginate2 samples after the heat treatment (1000 °C/1h) are given in Figure 3.25 (a and b).

As can be seen, although the Alginate1 sample contains some porosity, a similar porous structure was not formed in the Alginate2 sample. Accordingly, these samples were not selected for further experiments.

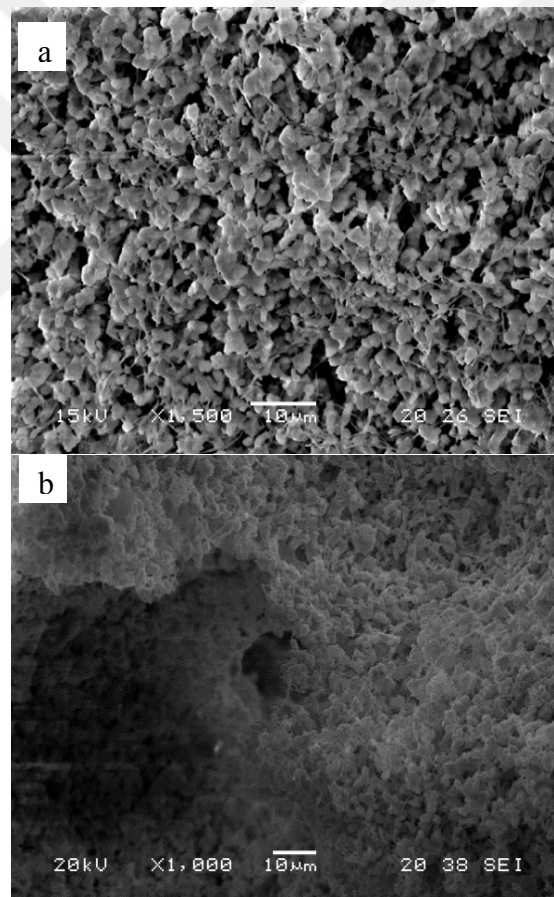


Figure 3.25 : SEM image of samples produced with XRG71 a) Alginate1 b) Alginate2.

3.2.2.2 HAPES

SEM micrographs from HAPES71 and HAPES72 samples, manufactured by using XRG71 and XRG72 synthesized powder ($\text{Ca/Si} = 0.83$ and $\text{Ca/Si} = 1.13$, both ball milled) are given in Figure 3.26.

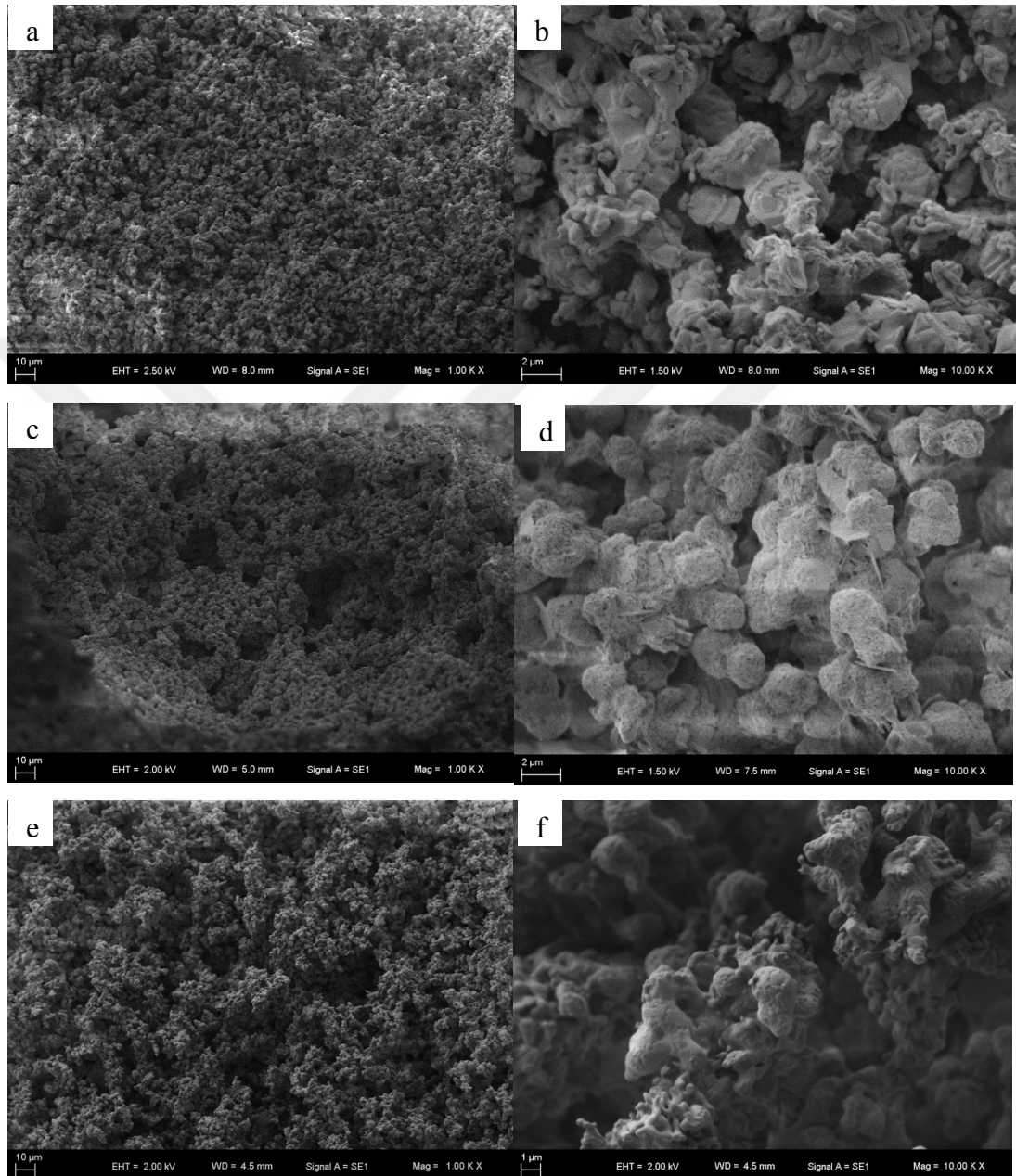


Figure 3.26 : SEM micrograph images from HAPES71-72, **a)** low magnification from green HAPES71 (produced with XRG71), **b)** higher magnification image taken from the same sample after heat treatment at 1000 °C, **c)** low magnification from HAPES72 (produced with XRG72), **d)** higher magnification from the same sample **e)** low magnification image taken from the HAPES72 after heat treatment at 1000 °C and **f)** higher magnification from the same sample.

Figure 3.27 shows microstructures of commercial xonotlite powders. It can be seen that these powders acicular structure xonotlite crystals.

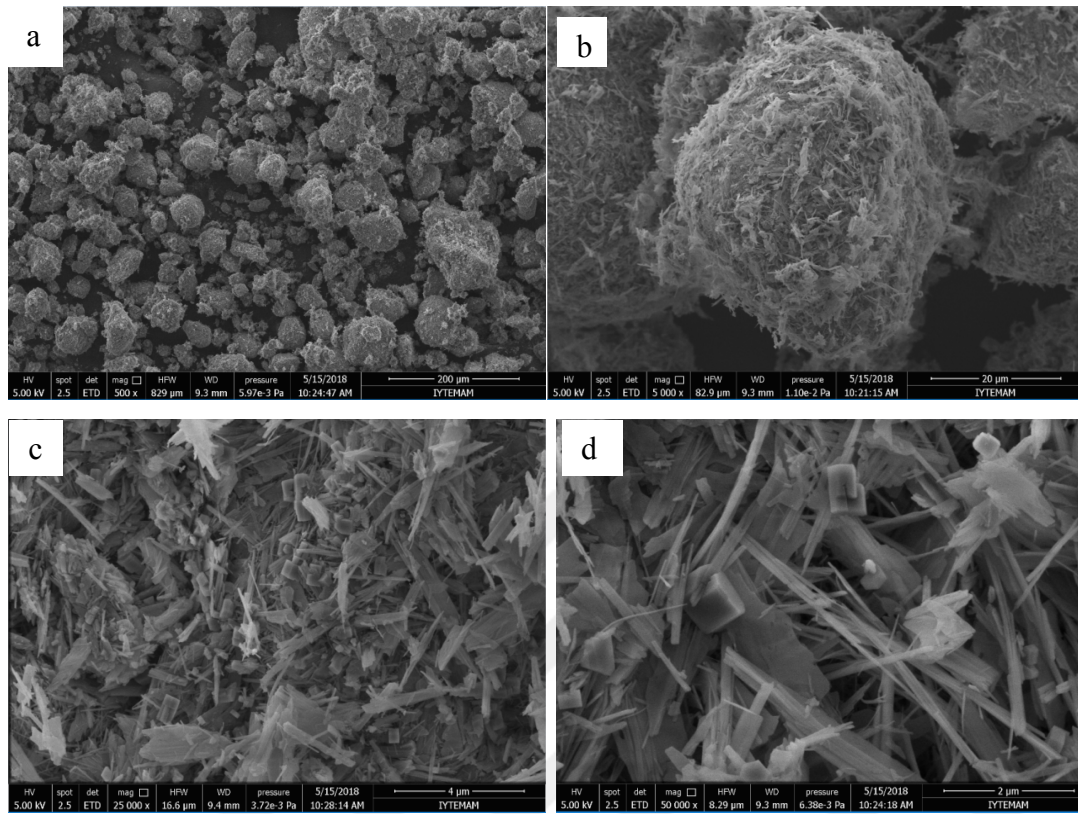


Figure 3.27 : SEM images of commercial Xonotlite powder, **a)** general view, **b)** higher magnification of pellets **c)** and **d)** higher magnification of acicular structure.

SEM images from the 25% HAPES sample made by using commercial CSH (Xonotlite) powder can be seen in Figure 3.28, where the sample has a highly porous microstructure.

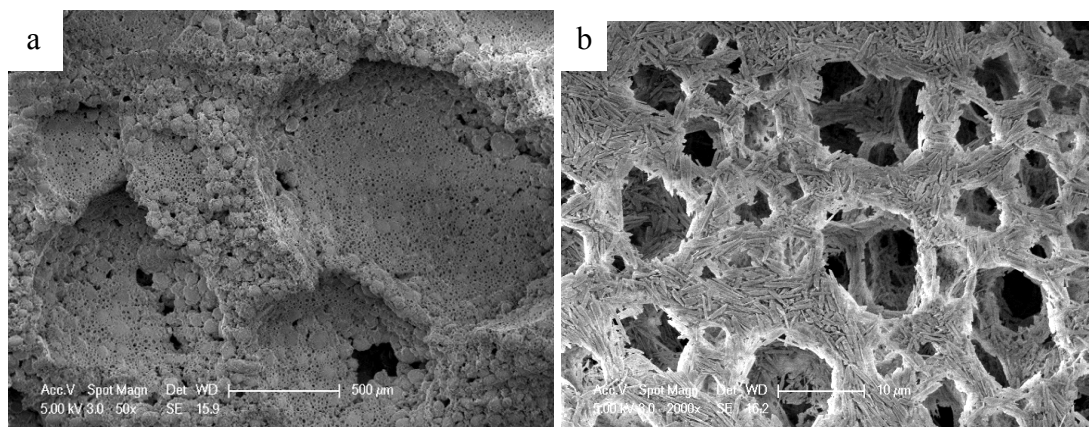


Figure 3.28 : SEM images from the 25% HAPES sample made by using commercial CSH (Xonotlite) **a)** general view, **b)** detail of pores.

Figure 3.29 shows the SEM images of the same sample (25%) with heat treatment 1200 °C/1 hr (heating rate 5°C / min). As can be seen, there is no major change in the microstructure of the sample.

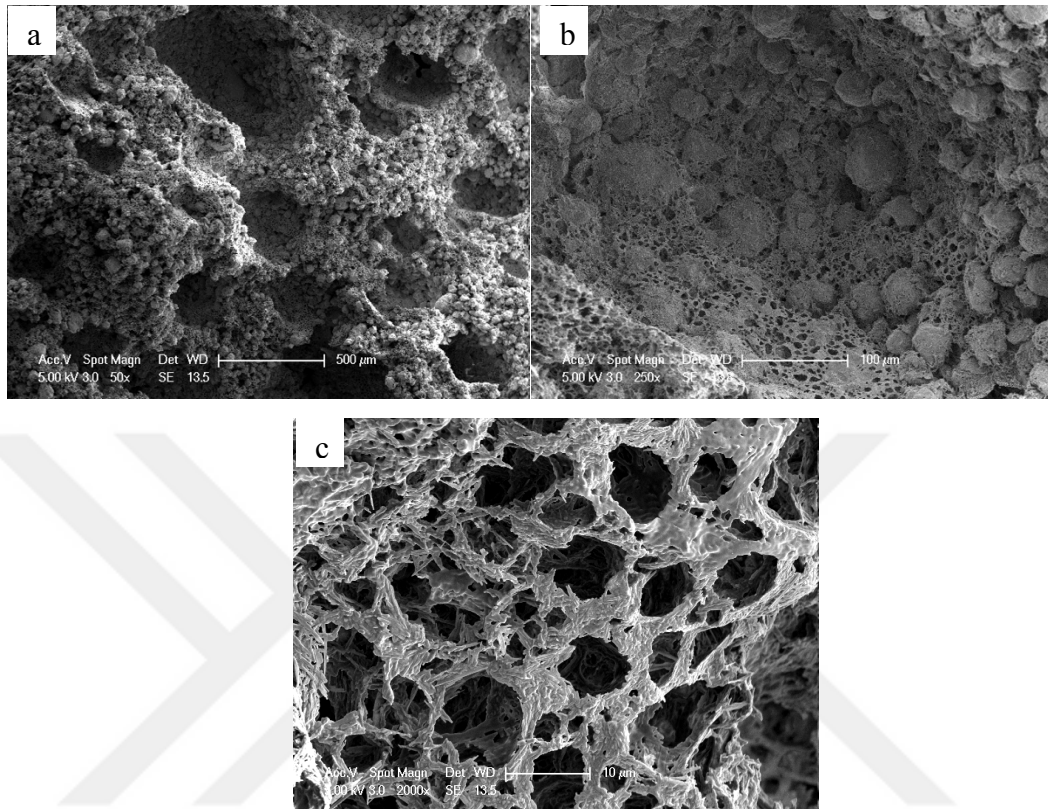


Figure 3.29 : SEM images from the 25% HAPES sample made by using commercial CSH (Xonotlite) powder after the heat treatment **a)** general view, **b)** from hollow, **c)** details of pores.

When the solid loading was increased to 30% and 35%, microstructure of the samples changes as can be seen in the Figures 3.30 (a and b).

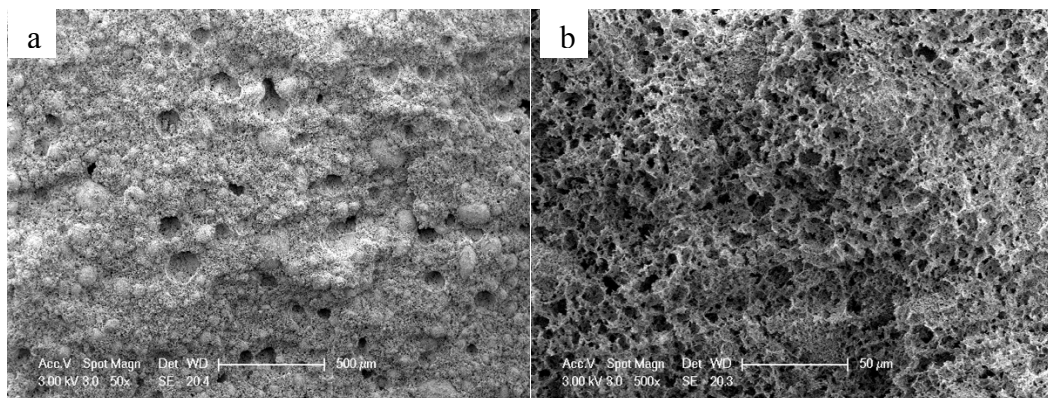


Figure 3.30 : SEM images of 35% solid loading HAPES sample made by using commercial CSH (xonotlite) **a)** general view, **b)** pore detail.

3.3 Characterization of Zeolite Coated Samples

3.3.1 Characterization of zeolite coated CSH/CH

The dried samples were calcined at 600 ° C for 1 hour in a muffle furnace and their weights before and after heat process were recorded. As can be seen from the results of mercury porosimetry in Table 3.4, the commercial CSH-zeolite used for the coating has a significant high pore content of 84% and the average pore size is around 0.65 microns. According to the results hydrothermal zeolite coating for 3 days (Sample HZC-XT-1), the pore size decreased to 0.3 microns and the total pore decreased to 78%.

Table 3.4 : The results of mercury porosimetry of zeolite coated sample CSH.

Sample	Porosity (%)	Average pore diameter (4V/A) (μm)	Bulk density 0.52 psia (g/mL)	Skeletal density (g/mL)	Reaction time (day)
CSH (commercial)	83.92	0.65	0.30	1.85	-
HZC-XT-1	77.55	0.30	0.50	2.22	3

New zeolite crystals may have caused a reduction in the porosity by narrowing or closing existing pore channels. As can be seen in Figure 3.31, the pore sizes shifted to smaller values after coating and some of the large pores were also disappeared.

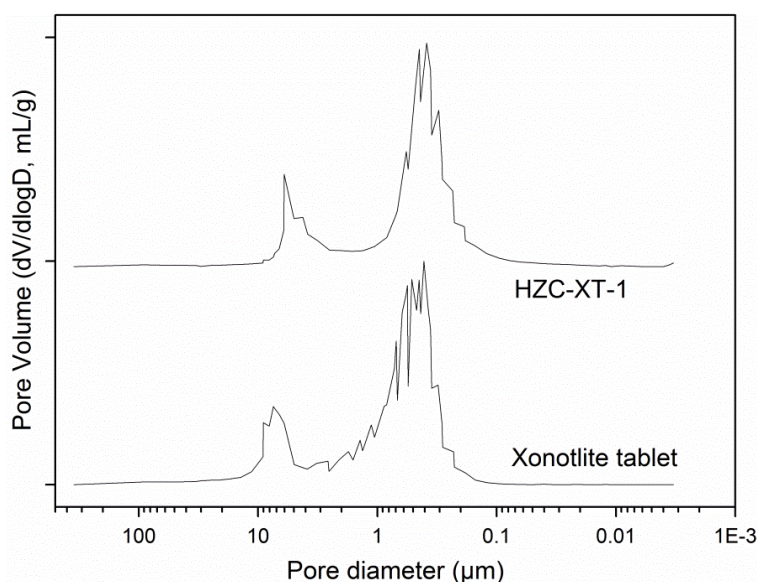


Figure 3.31 : The PSD curves results of commercial Xonotlite and sample HZC-XT-1 from the mercury porosimeter.

In order to investigate the microstructure after the coating process, SEM analysis was performed (see, Fig 3.32). In Figure 3.32(a), the overall microstructure SEM image of a broken part from the sample HZC-XT-1 can be seen. At the higher magnification, the acicular CSH crystals appear in the classical CSH agglomerate (see Fig. 3.32 (b)). As can be seen in Figures 3.32 (c and d), different types of zeolite structures can be seen adhering to the CSH agglomerate.

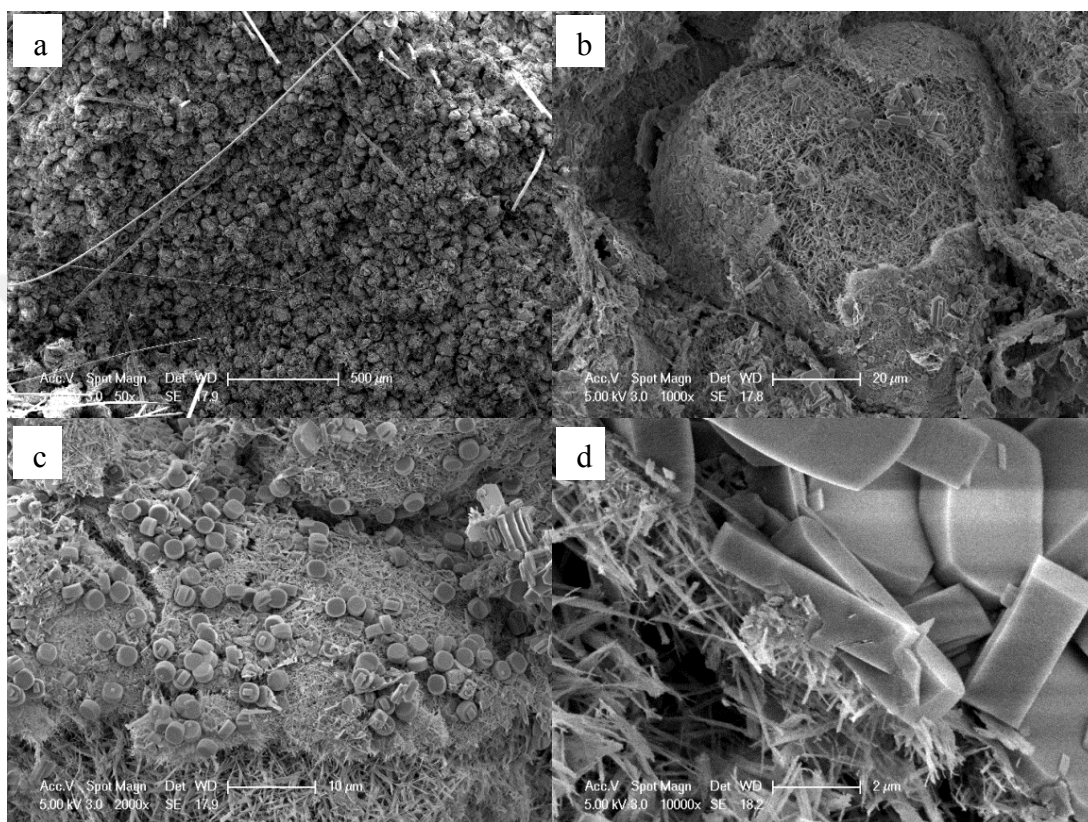


Figure 3.32 : The SEM images of sample HZC-XT-1(3 days reac. time) **a)** general view, **b)** higher magnification from the pellet, **c,** and **d)** the detail of zeolite crystals from the gap of between CSH particle

When the microstructure of the sample is examined at the lowest magnification, it can be said that the structure consists of an aggregation of Xonotlite particles (see Figure 3.27 (a and b)). The N_2 adsorption/desorption isotherms curves from the commercial CSH and HZC-XT samples are given in Figure 3.32.

As can be seen from the results of N_2 adsorption/desorption isotherms given in Table 3.5 and Fig. 3.33, the surface area of commercial xonotlite showed an increase from about $10 \text{ m}^2/\text{g}$ to $137.6 \text{ m}^2/\text{g}$ following a 3 days hydrothermal zeolite coating reaction.

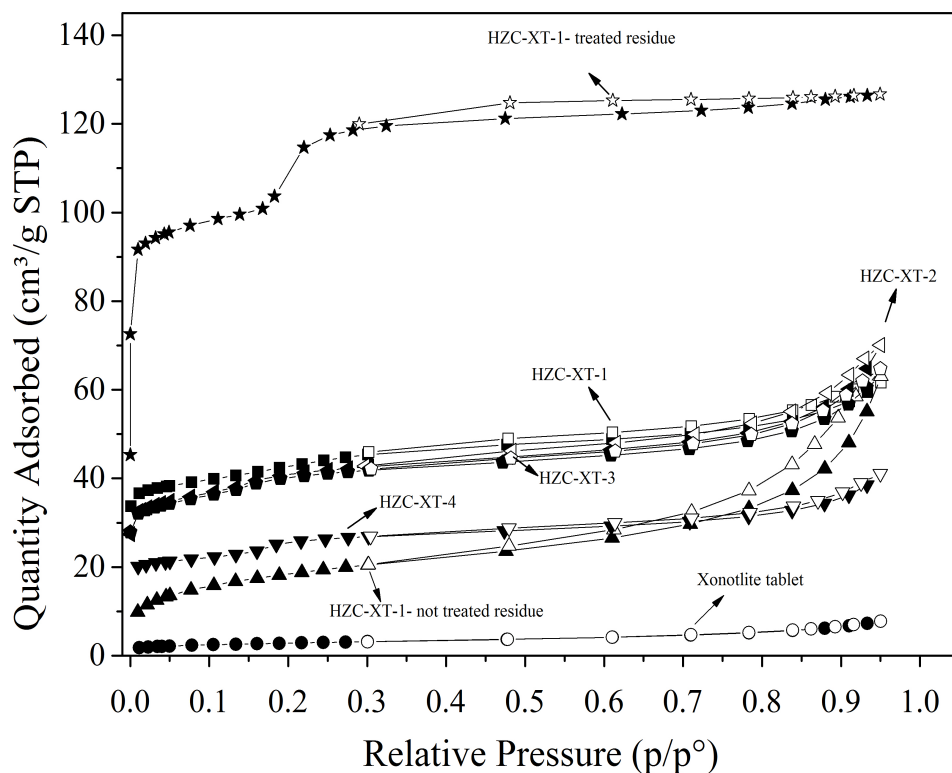


Figure 3.33 : The N₂ adsorption/desorption isotherms curves from the commercial CSH and HZC-XT samples.

Table 3.5 : The N₂ ads/des. results of commercial CSH and HZC-XT samples.

Sample	Volume of Pores (cm ³ /g)			Pore size (Å)		Reax. time (day)
	BET (m ² /g)	BJH Adsorption cumulative volume of pores (cm ³ /g)	BJH Desorption cumulative volume of pores (cm ³ /g)	BJH Adsorption average pore width (4V/A)	BJH Desorption average pore width (4V/A)	
CSH (Commercial)	9.885	0.009	0.010	78.334	74.974	
HZC-XT-1	137.560	0.033	0.034	76.387	62.764	3
HZC-XT-2	130.465	0.051	0.054	104.817	82.762	5
HZC-XT-3	127.950	0.043	0.044	100.686	87.474	7
HZC-XT-4	83.009	0.027	0.029	93.209	77.397	10

The increased reaction time did not result in an expected change, instead a negative effect was observed for periods of more than 7 days, and the specific surface area for the samples decreased.

3.3.2 Characterization of zeolite coated SiOC

The results of SEM of the HZC-PDC-7 sample obtained after 3 days of hydrothermal reaction by using L1 sample as substrate are given in Figure 3.34. The zeolite coating of SiOC samples are not homogeneous. While certain areas are completely covered with zeolite crystals, in some areas the coating is thin or even absent.

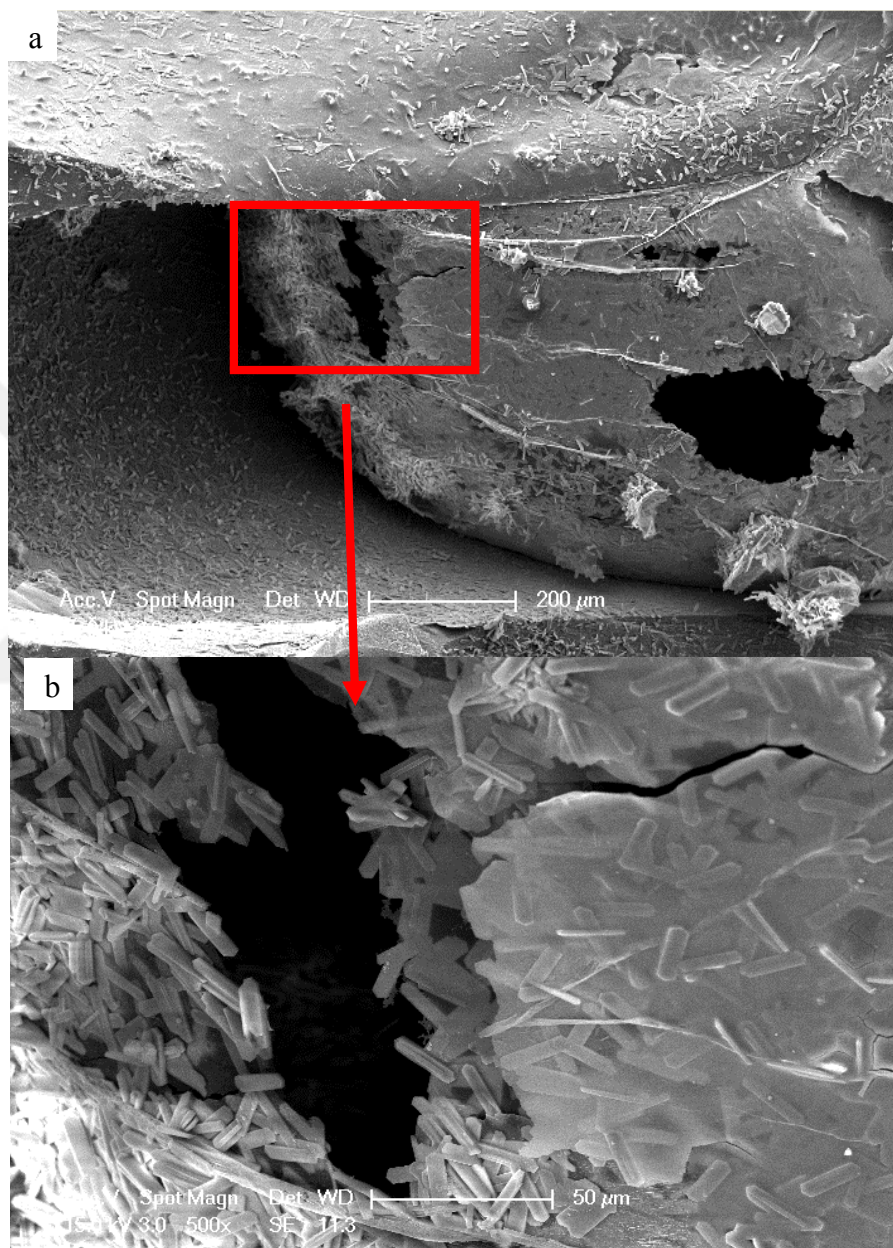


Figure 3.34 : SEM images of HZC-PDC-7 sample obtained by 3-day hydrothermal reaction using L1 sample as substrate **a)** general view **b)** higher magnification.

For HZC-PDC-1,3,4,5 samples, L3 was used as the substrate, which has a surface area of 122 m²/g. HZC-PDC-7,8,9,10 samples were produced by coating of L1

sample, which had a surface area of 4 m²/g. The results obtained after hydrothermal zeolite coating process are different for two different sets and are shown in Table 3.6.

Table 3.6 : N₂ ads./des. results of samples HZC-PDC and their substrates.

Sample	BET (m ² /g)	Pore volume (cm ³ /g)		Pore size (Å)		Substrate	Reax. time (day)
		BJH Adsorption cumulative volume of pores (cm ³ /g)	BJH Desorption cumulative volume of pores (cm ³ /g)	BJH Adsorption average pore width (4V/A)	BJH Desorption average pore width (4V/A)		
L3	121.89	0.48	0.47	151.71	129.48	-	-
HZC- PDC-1	80.56	0.20	0.21	132.63	108.78	L3	3
HZC- PDC-3	72.03	0.12	0.13	125.54	103.14	L3	5
HZC- PDC-4	109.33	0.22	0.23	121.07	92.15	L3	7
HZC- PDC-5	128.26	0.20	0.21	109.34	82.61	L3	10
L1	4.30	0.02	0.02	244.78	156.91	-	-
HZC- PDC-7	40.09	0.01	0.01	91.90	73.91	L1	3
HZC- PDC-8	31.07	0.01	0.01	104.47	73.01	L1	5
HZC- PDC-9	56.72	0.01	0.01	104.84	79.13	L1	7
HZC- PDC- 10	55.29	0.01	0.01	100.23	86.43	L1	10

The N₂ adsorption/desorption and pore size distribution curves for all HZC-PDC samples and their substrate are given in Figure 3.35.

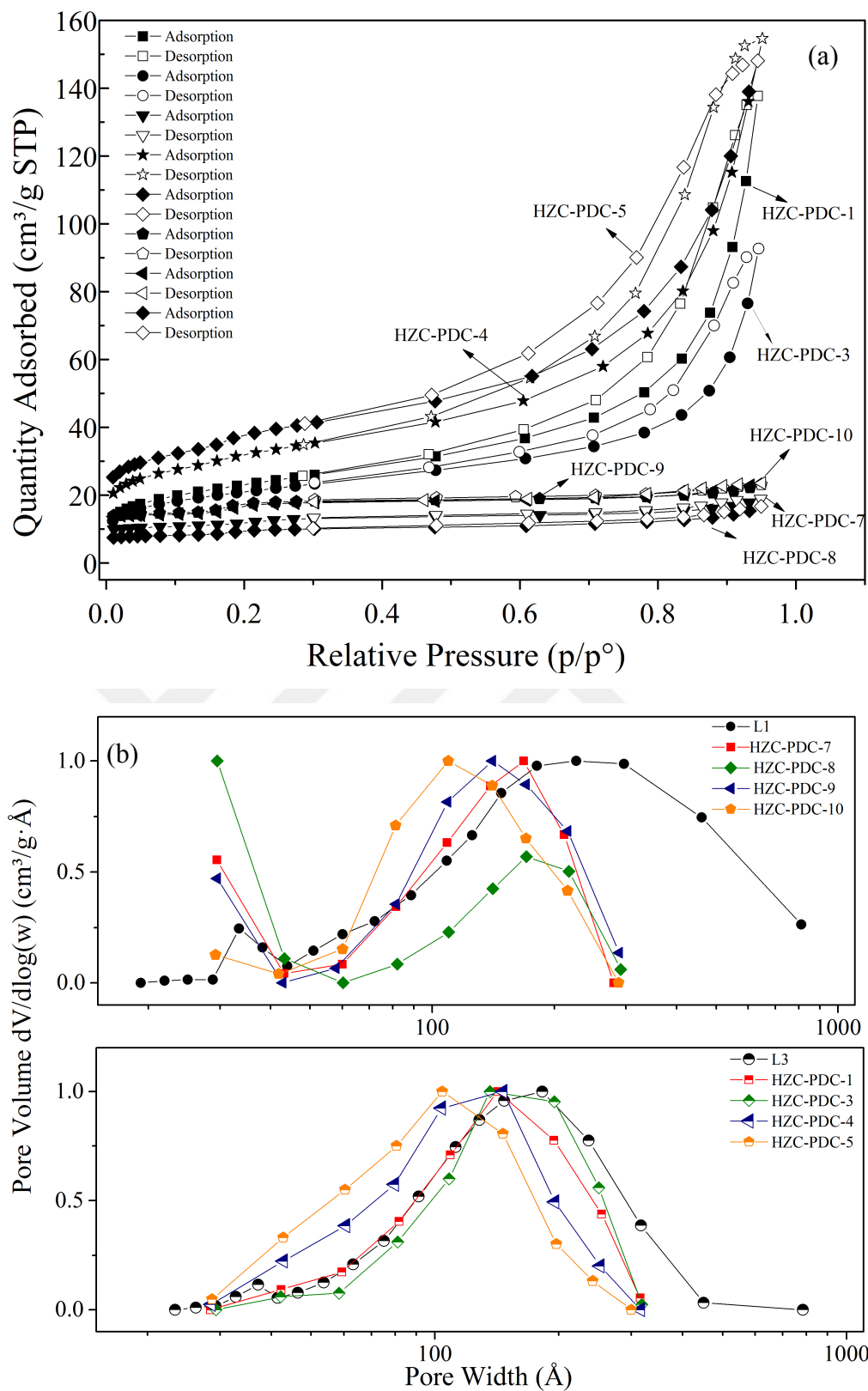


Figure 3.35 : a) The N_2 adsorption/desorption isotherms and b) pore size distribution graphs of all HZC-PDC samples.

Some of the selected samples were subjected to mercury porosimeter tests (see Table 3.7 and Figure 3.36), the results similarly show a decrease in the average pore diameter after coating.

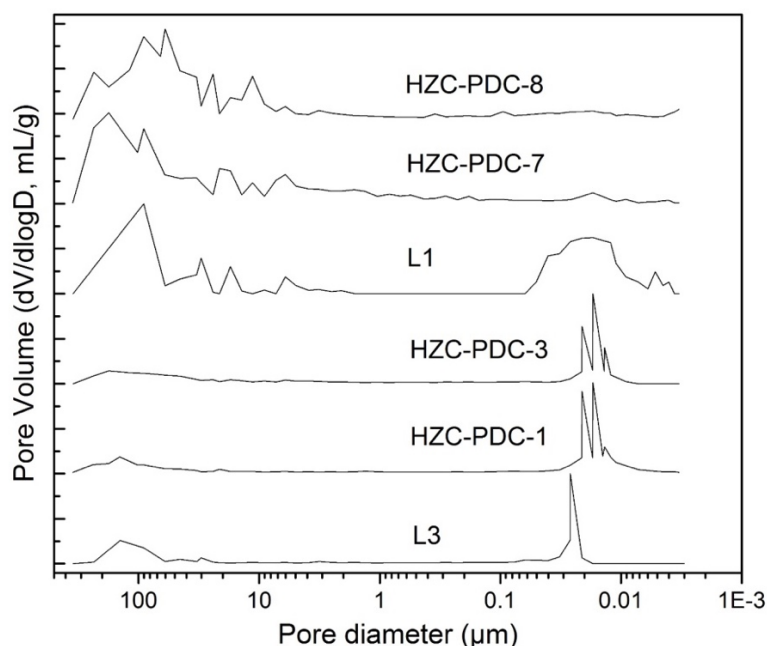


Figure 3.36 : PSD curves of HZC-PDC-1,3,7,8 and L1-3 samples, plotted using results from the mercury porosimeter.

Table 3.7 : Pore character information of HZC-PDC samples and substrates measured by mercury porosimetry.

Sample	Porosity (%)	Average pore diameter (4V/A) (μm)	Bulk density (0.52 psia) (g/mL)	Skeletal density (g/mL)	Substrate	Time (day)
HZC-PDC-1	63.0343	0.0311	0.7499	2.0286	L3	3
HZC-PDC-3	66.2648	0.0647	0.6673	1.9782	L3	5
HZC-PDC-7	44.4219	0.3008	1.034	1.8605	L1	3
HZC-PDC-8	38.0287	0.1263	1.1088	1.7892	L1	5

As a result of the zeolite coating of SiOC ceramics, roughly speaking there was a closure in the pores and not significant increase in the specific surface area was

observed. Therefore, HZC-PDC-3 sample was the only one selected for the water purification tests.

3.4 Removal of Pollutants from Aqueous Solution

3.4.1 Removal of dyes

As can be seen from Fig. 3.37, the maximum retention for RB was obtained at pH 7, whereas for MB and CV, the optimum pH was found at 8. These pH values were taken into consideration in subsequent studies.

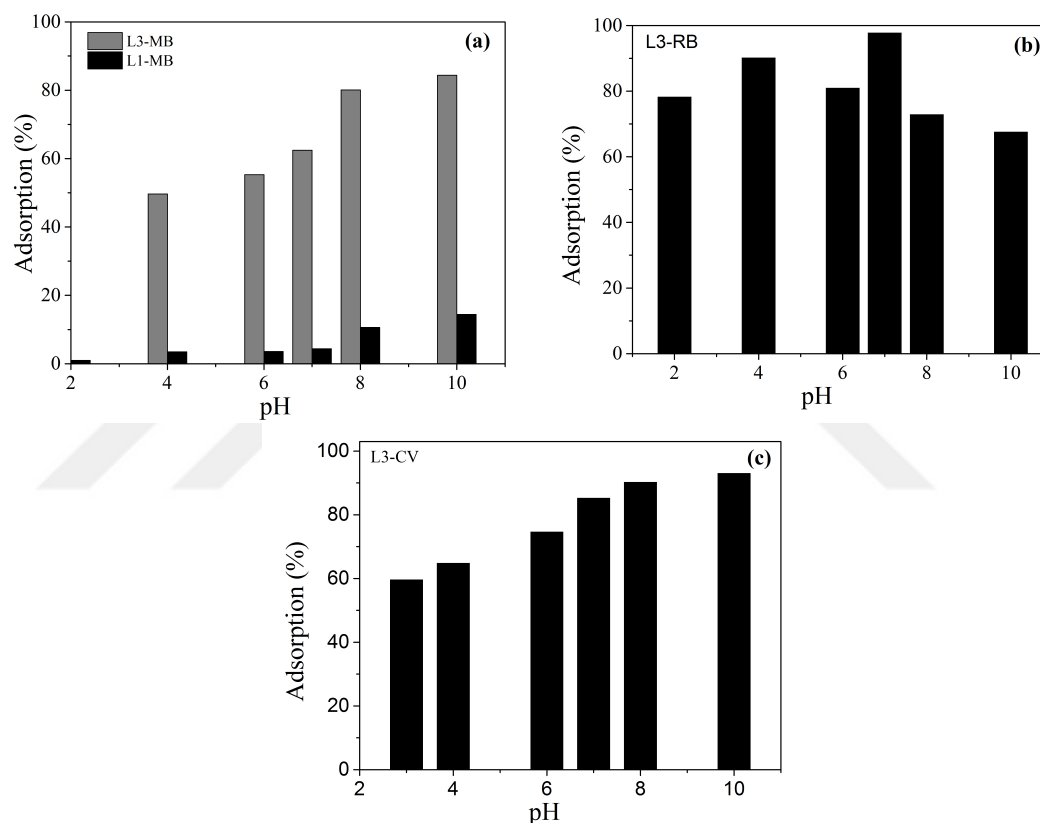


Figure 3.37 : The retention graphs at different pH values, (a) L1 ve L3, MB, (b) L3, RB ve (c) L3, CV.

Upon treatment of SiOC with HF, the adsorption capacities increased at least 2 times.

The capacity of the L1 sample for MB was increased from about 16 mg/g to 96 mg/g, showing the highest increase after etched by HF. Similar results were obtained when the adsorption capacities of L1HF and L3HF samples with approximate surface area values were compared. These samples showed adsorption capacities of about 96 and 104 mg/g MB. The adsorption capacity Q_e (mg/g) graphs of the three

dyes onto L1-L3 are given in Figure 3.38 (C_e (mg/L) refers to the concentration of the adsorbate at the equilibrium).

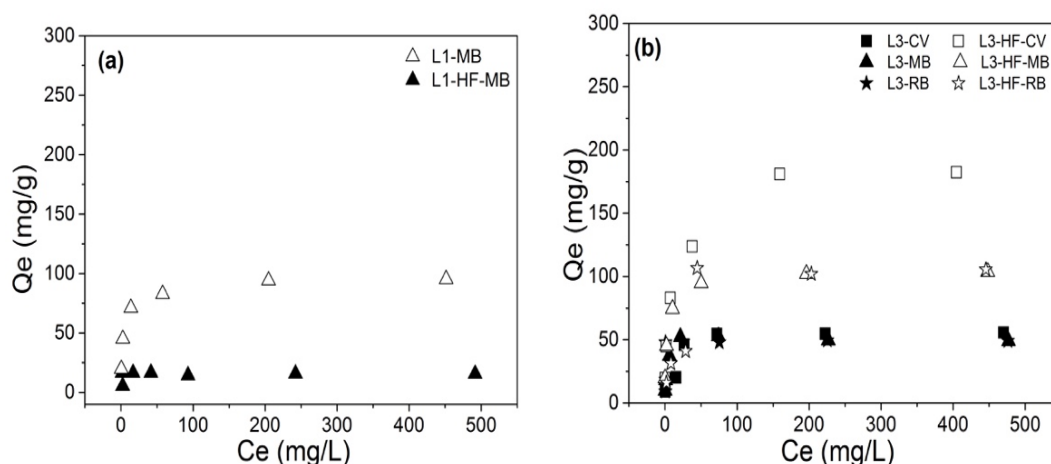


Figure 3.38 : MB, CV, RB adsorption for samples; **(a)** L1 and L1HF, **(b)** L3 and L3HF.

In Table 3.8, the results for both isotherm models were given. The Langmuir isotherm model was found to be more appropriate by taking the R^2 values into consideration. The obtained values show that SiOC samples, especially HF etched ones are successful candidates for the removal of dyes from water.

The results obtained from the adsorption experiments for MB, RB and, CV tested by zeolite coated samples HZC-XT-3, HZC-PDC-3, and substrates are shown in Figure 3.39 (a and b). The adsorption capacity of the dyes onto Alginate1 sample was compared with the concentration of the adsorbate at the time of equilibrium (mg/L), and the adsorption capacity of the adsorbent Q_e (mg/g) graph is given in Figure 3.39 (c). The HZC-PDC-3 sample was gave approximately 35% to 85% lower than commercial Xonotlite when dye adsorption is considered. In the case of the HZC-XT-3 sample, it was found that zeolite coated sample adsorbed about 40% less MB than its substrate. In the adsorption of tested dyes by Alginate1 sample, with the adsorption capacity of 19 mg/g, the best results for MB was obtained.

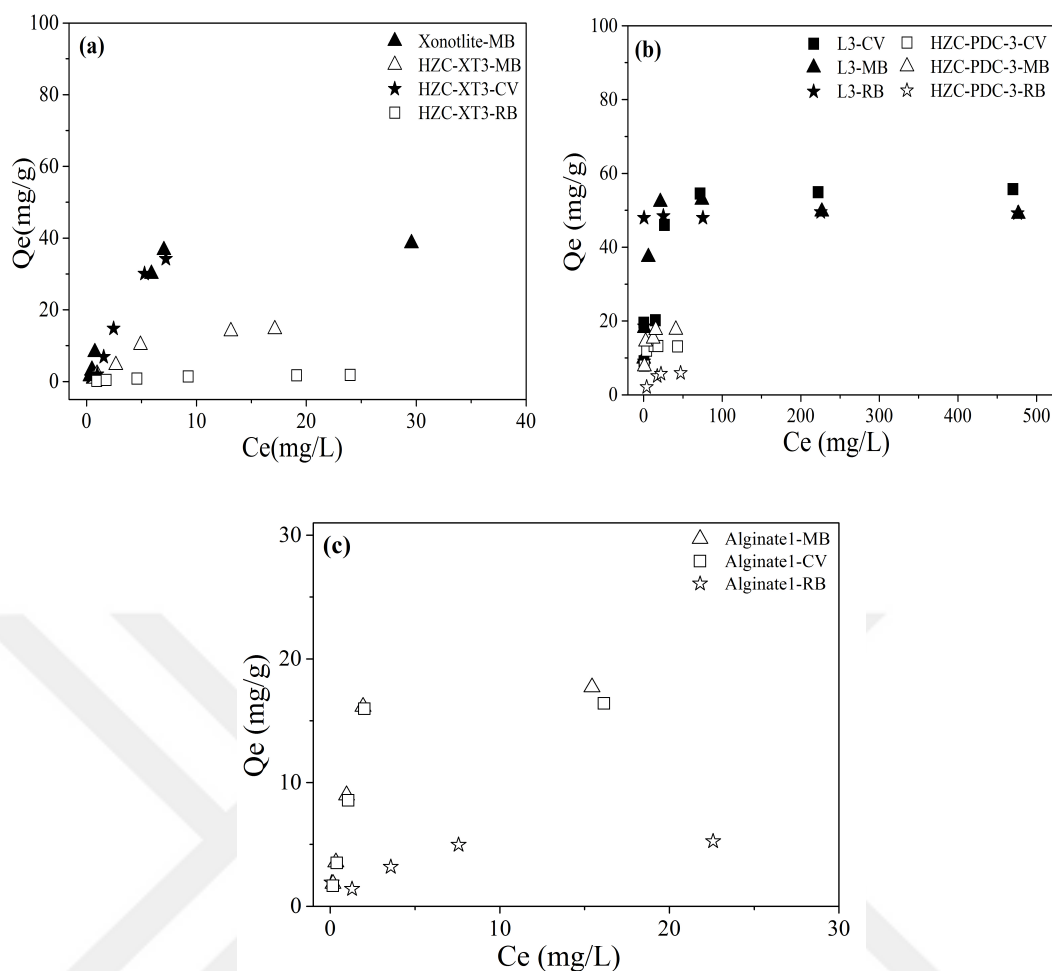


Figure 3.39 : The adsorption capacities of the sample **a)** HZC-XT-3 and Xonotlite (commercial CSH) **b)** HZC-PDC and its substrate L3, and **c)** Alginat1.

In adsorption experiments to remove dyes from water, the etched SiOC samples were exhibited much higher adsorption results compared to the non-etched samples. The adsorption capacity of the SiOC sample with a surface area of $4 \text{ m}^2/\text{g}$ increased from 16 mg/g to 96 mg/g by etching. Two different SiOC samples with similar SSA areas ($L1\text{HF} = 774 \text{ m}^2/\text{g}$) ($L3\text{HF} = 663 \text{ m}^2/\text{g}$) showed similar adsorption capacities (96 and 104 mg/g MB).

The obtained values show that SiOC samples which especially HF etched ones are successful candidates for the removal of dyes from water.

All dye experiments were investigated for their suitability to Langmuir and Freundlich isotherm. The results for both isotherm models are given in Table 3.8.

Table 3.8 : Results of Langmuir and Freundlich isotherms for all samples.

Sample Code	Dyes	Langmuir Isotherm			Freundlich Isotherm		
		q _m (mg/g)	K _L (L/mg)	R ²	n	K _f (mg/g)	R ²
L1	MB	15.68	0.84	0.999	2.17	0.22	0.885
L1HF	MB	96.06	0.23	0.999	4.83	32.67	0.884
L3	MB	49.26	1.70	0.999	5.08	19.91	0.810
	CV	49.47	0.14	0.997	4.78	17.39	0.720
L3HF	RB	49.38	1.05	0.999	6.60	22.98	0.681
	MB	104.27	0.05	0.999	5.25	39.06	0.936
	CV	185.87	0.13	0.998	3.90	43.22	0.982
Commercial CSH	RB	110.74	0.31	0.990	2.74	14.62	0.810
	MB	46.93	0.19	0.925	1.38	5.98	0.843
	MB	28.05	0.07	0.694	1.21	1.81	0.917
HZC-XT-3	CV	51.33	0.09	0.615	0.79	3.40	0.947
	RB	2.82	0.08	0.917	1.38	0.22	0.920
HZC-PDC-3	MB	18.11	0.85	0.997	5.06	9.44	0.668
	CV	13.29	2.70	0.999	7.48	8.80	0.719
	RB	6.97	0.14	0.986	2.25	1.27	0.856
Alginate1	MB	19.09	0.89	0.993	1.98	6.70	0.755
	CV	17.62	0.90	0.992	1.98	6.20	0.742
	RB	5.76	0.48	0.997	4.82	2.49	0.455

3.4.1.1 Regeneration of SiOC

The results of the regeneration studies using both temperature rise (medium temperature heat treatment) ethanol are shown in Table 3.9 and Figure 3.40. The values in zero (0) cycles indicate the first MB adsorption rate of the sample, and it can be seen that it is almost 100%. When ethanol was used to extract dye molecules, retention efficiency decreased to 97% in the third cycle of the desorption-adsorption process. In heat treatment experiments, re-adsorption rate was 99% even at the end of the third cycle.

Table 3.9 : The results of regeneration studies with heat treatment (400 °C) and EtOH.

Sample	Regeneration with EtOH				Regeneration with heat treatment			
	Adsorbed MB (% , avr)				Adsorbed MB (% , avr.)			
	0.	I.	II.	III.	0.	I.	II.	III.
L3HF	cycle	cycle	cycle	cycle	cycle	cycle	cycle	cycle
	99.88	98.87	98.06	97.17	99.88	99.56	99.44	99.38

In regeneration with ethanol, even though 97% MB adsorbed after the 3rd cycle, the pH value of this process is low as around 2, such high acidity is likely to affect the structure of the sample. In this context, the application of thermal regeneration showing an adsorption rate of 99% after the third cycle is more suitable for the materials produced in this study.

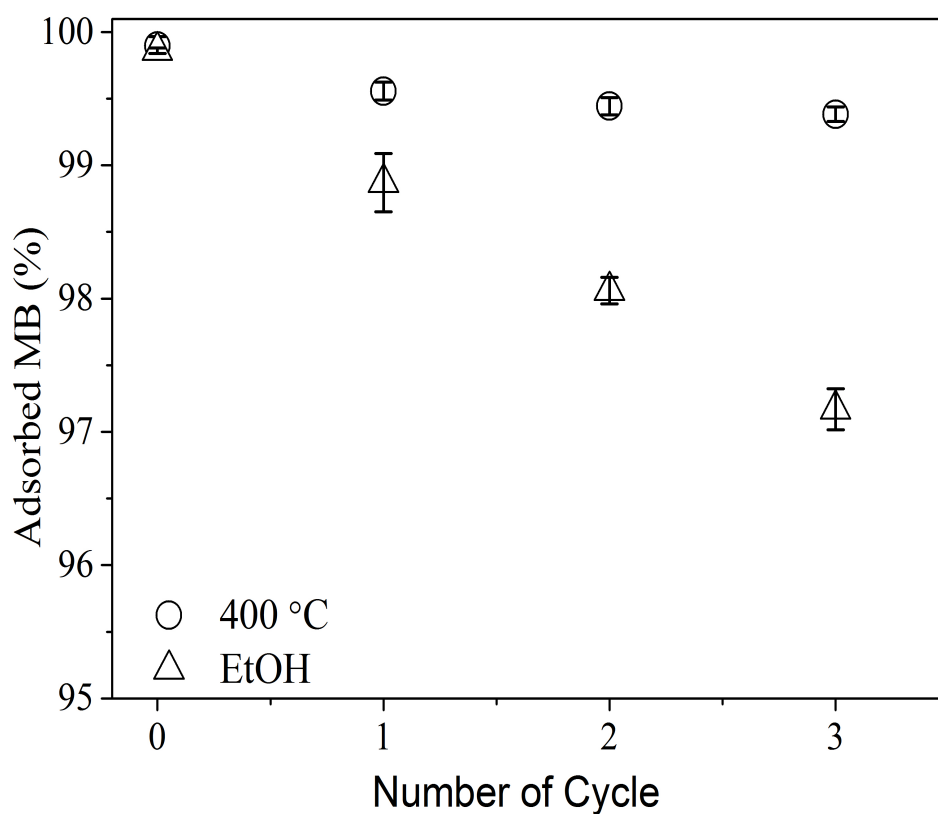


Figure 3.40 : The re-sorption yield for sample L3HF.

3.4.1.2 Adsorption of dye mixture

In Figure 3.41, the image shows the decolourization of the mixture of three dyes with different contact time.

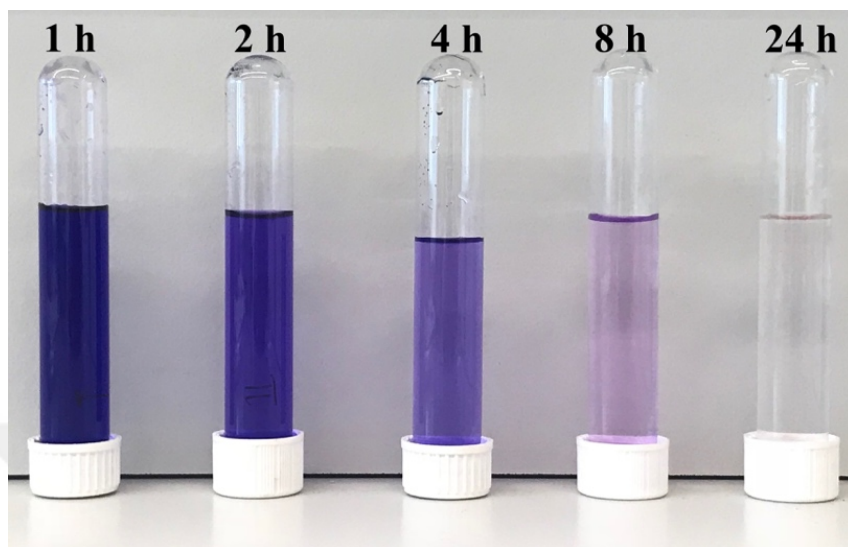


Figure 3.41 : The decolourization of three dyes mixture after 1-24 h contact time with sample L3-HF.

The adsorption percentages of these three dyes showed similarity. At the end of eight hours, 98% retention was observed in all three dyes. The calculated results are given in Table 3.10. The sample tested has no specific affinity for any of these dyes. The sample has the capacity to adsorb all three dyes at a rate of more than 99% simultaneously.

Table 3.10 : Adsorption percentage of the mixture of three dyes onto sample L3-HF at different contact time.

Sample	Contact time (hour)	Adsorption (%)		
		MB (668 nm)	CV (589 nm)	RB (555 nm)
L3HF	1	58.02	55.02	59.48
	2	83.63	82.26	77.16
	4	94.37	91.63	91.90
	8	98.02	98.16	98.24
	24	99.75	99.36	99.41

3.4.1.3 Characterization of the saturated SiOC

Figure 3.42 (a) shows the FTIR data of the pure dye molecules, while the data obtained from the etched SiOC sample is also shown at the bottom of the Figure 3.42 (b), the data obtained from same sample saturated with dyes can be seen the top of it. In the FTIR data of the L3HF sample, a shoulder can be seen at 1010 cm^{-1} is caused by Si-O stress vibration from the Si-O-Si or the Si-O-C units. Another distinct band at 800 cm^{-1} as seen previously in HF etched SiOC samples[73, 74], indicating the Si-C stress vibration. The aromatic C=C and CN bands in MB, CV, and RB are known to occur in the $1000\text{-}1600\text{ cm}^{-1}$ range and this "signature" is clearly visible in Figure 3.42(a) [75, 76]. In the FTIR data of the etched SiOC sample, there is no peak in this region, but when the same sample was saturated with dyes, it is clear that the new peaks are formed in between $1000\text{-}1600\text{ cm}^{-1}$. These new peaks can be proof of those dyes attached to the sample.

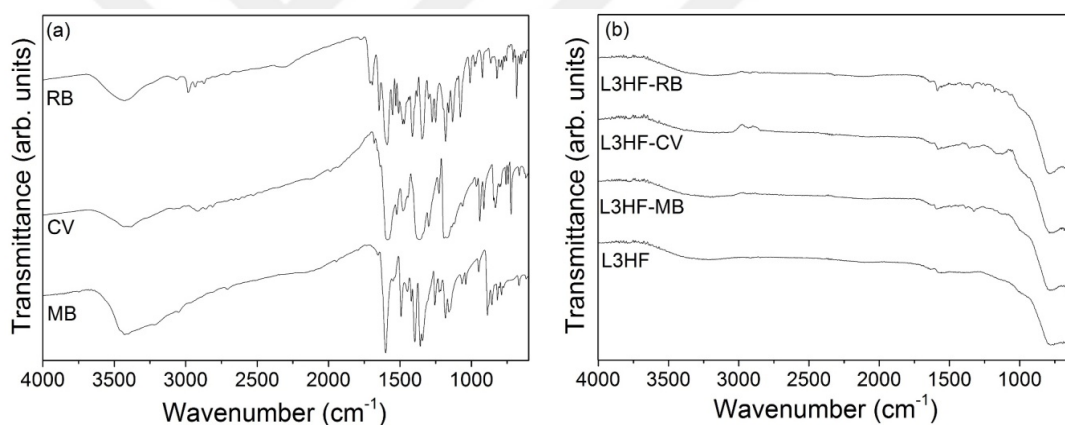


Figure 3.42 : FTIR data of **a)** pure MB, CV and RB molecules, **b)** etched SiOC sample and after the dye loaded of sample.

SEM images taken from SiOC fracture surface, and TEM analysis of the sample prior to coating can be seen in the inset of Figure 3.43 (a). In the TEM image given in Figure 3.43 (a), both the macro ($> 50\text{ nm}$) and meso ($2\text{-}50\text{ nm}$) porous structure of the sample are seen, and the SEM image shows surface roughness. This type of microstructure is commonly found in etched ceramics. The SEM images of the MB-saturated L3HF show that the surface pores were closed. The surface forms a relatively smooth layer after the dye molecules coated the sample surface (see Fig. 43 (b-d)).

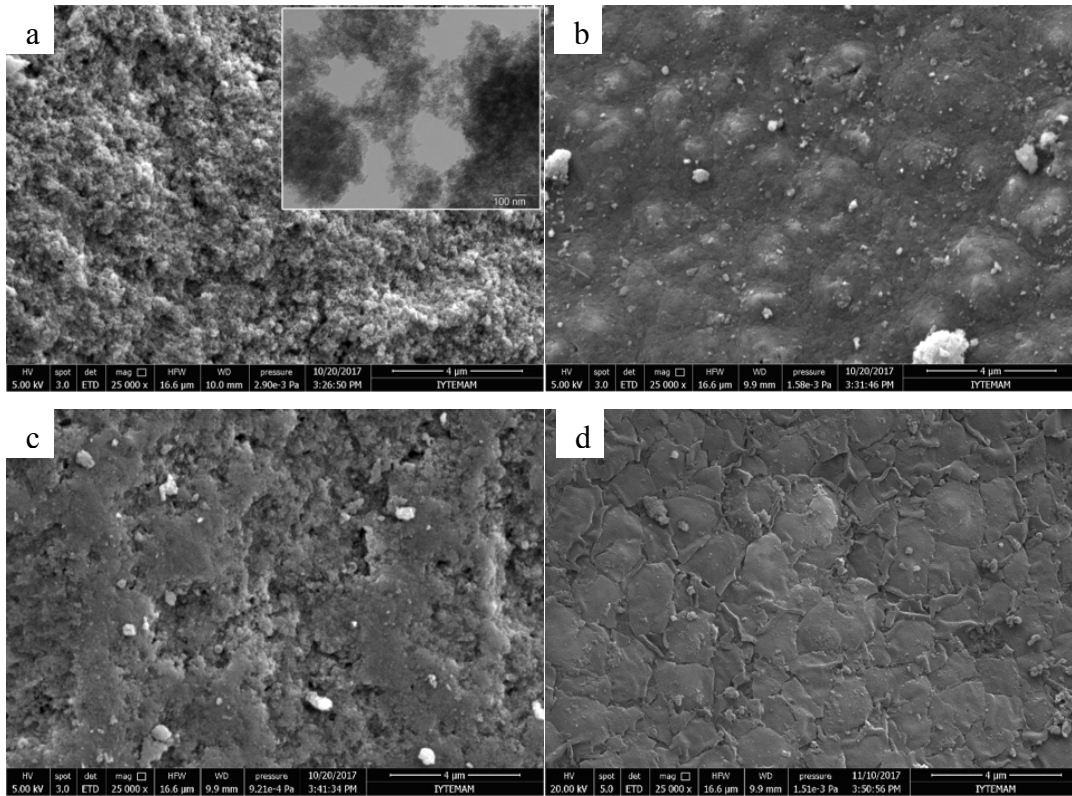


Figure 3.43 : a) The SEM and TEM figure of L3HF sample before the loaded with dye, the SEM images of L3HF loaded with b) MB, c) RB and, d) CV.

The EDX analyses taken from base L3HF sample and the MB loaded sample are given in Figures 44 (a and b), and Table 3.11.

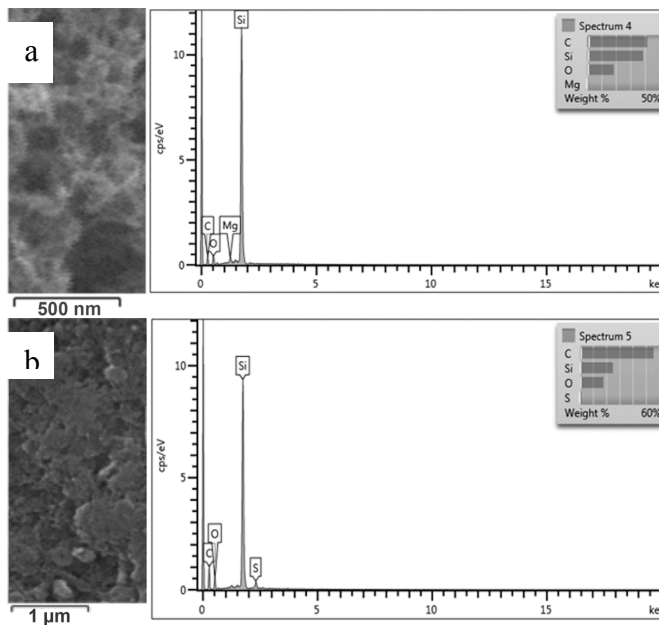


Figure 3.44 . The EDX results from the a) sample L3HF , b) MB loaded L3HF.

The Sulphur signals obtained from the MB coated sample can be seen. It is known that MB molecule contains S element. This is another clue showing that the dye molecule is attached to the surface of the material.

Table 3.11 : The elemental ratio from the EDX analysis of L3HF and after the dye loaded the same sample.

Element	L3HF	L3HF-MB
	EDX data (% Weight)	EDX data (% Weight)
C	41.77	55.75
O	18.52	17.88
Mg	0.95	0.00
Si	38.75	25.00
S	0.00	1.37
Total	100.00	100.00

The BET N₂ adsorption/desorption analysis was performed both before and after the L3HF sample was saturated separately with MB, CV or RB. The BET surface area was approximately 700 m² g in the L3HF sample and after dye loading, this value was found to be approximately 500 m²/g. The reduction in the surface area also showed that, like the previous findings, dyes were attached to the surface of the sample and covered a certain part of the pores. The analysis indicates that the pores in the meso size are closed, as can be seen from the pore size distribution graphs. The N₂ adsorption/desorption and pore size distribution graphs can be seen in Figure 3.45 comparatively with the sample L3HF and after loaded with MB, CV, and RB.

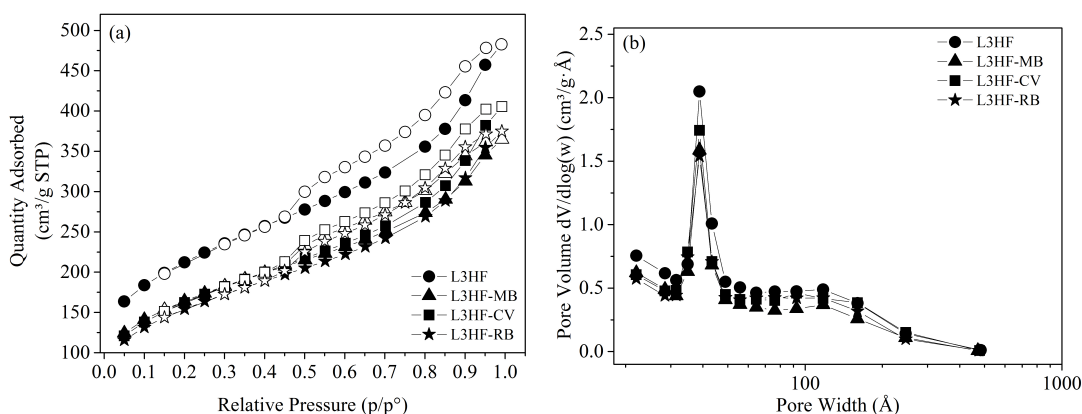


Figure 3.45 : L3HF sample before and after dye adsorption, **a)** N₂ adsorption/desorption isotherms, **b)** pore size distribution graph.

3.4.2 Removal of metals

There is no significant difference in the adsorption values for L1-L3 samples (Figure 3.46) in between pH of 5-7. In order to avoid possible metal oxide precipitation, the pH was adjusted to 6 ± 0.15 for the following studies.

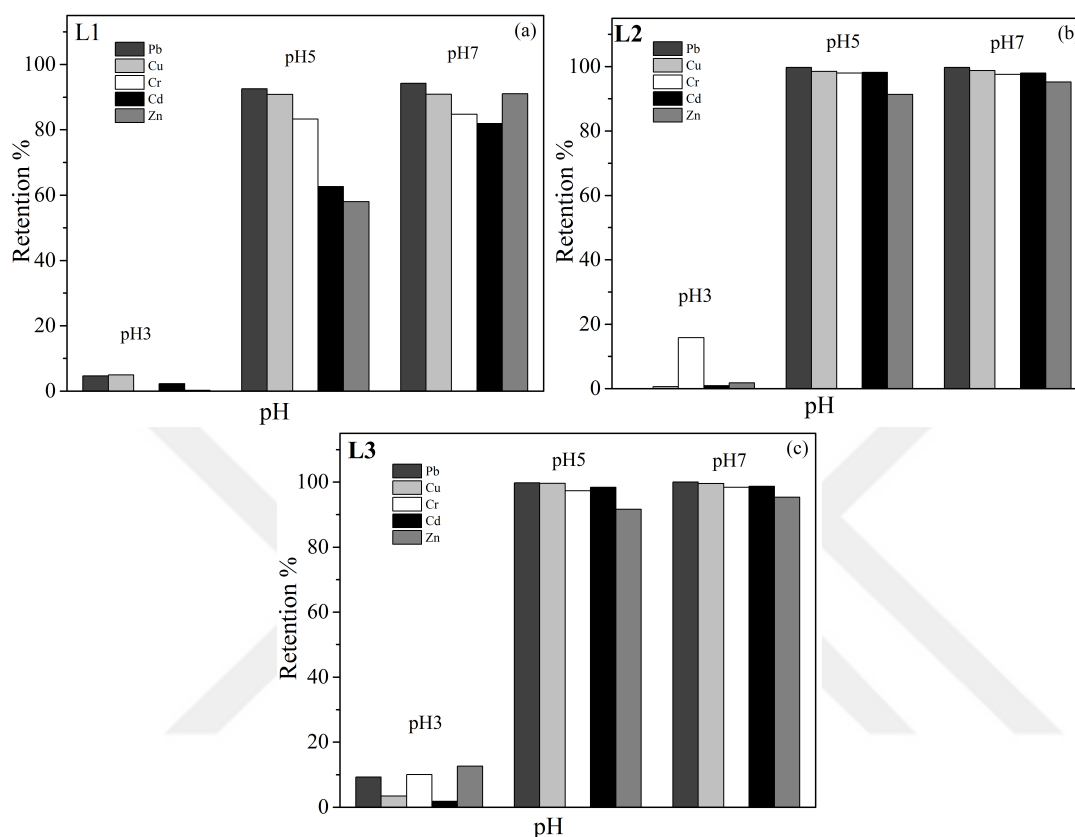


Figure 3.46 : The retention percentage graphs taken at different pH values for samples, (a) L1, (b) L2, and (c) L3.

The adsorption capacity of the L1-L3 samples for metal ions are compared with the concentration of the adsorbate at the time of equilibrium C_e (mg/L).

In the L1-L3 samples, a correlation is observed between the surface area of the sample and the maximum adsorption capacity. The L1 sample with a SSA of $4 \text{ m}^2/\text{g}$, the adsorption of Zinc ions was 0.6 mg/g . When the sample was HF etched (L1-HF) the SSA enhanced to $773 \text{ m}^2/\text{g}$ and so the adsorption value become 7.7 mg/g .

The adsorption capacity of the adsorbent Q_e (mg/g) versus the concentration of the adsorbate at the time of equilibrium C_e (mg/L) graphs for L1-L3 samples are given in Figure 3.47.

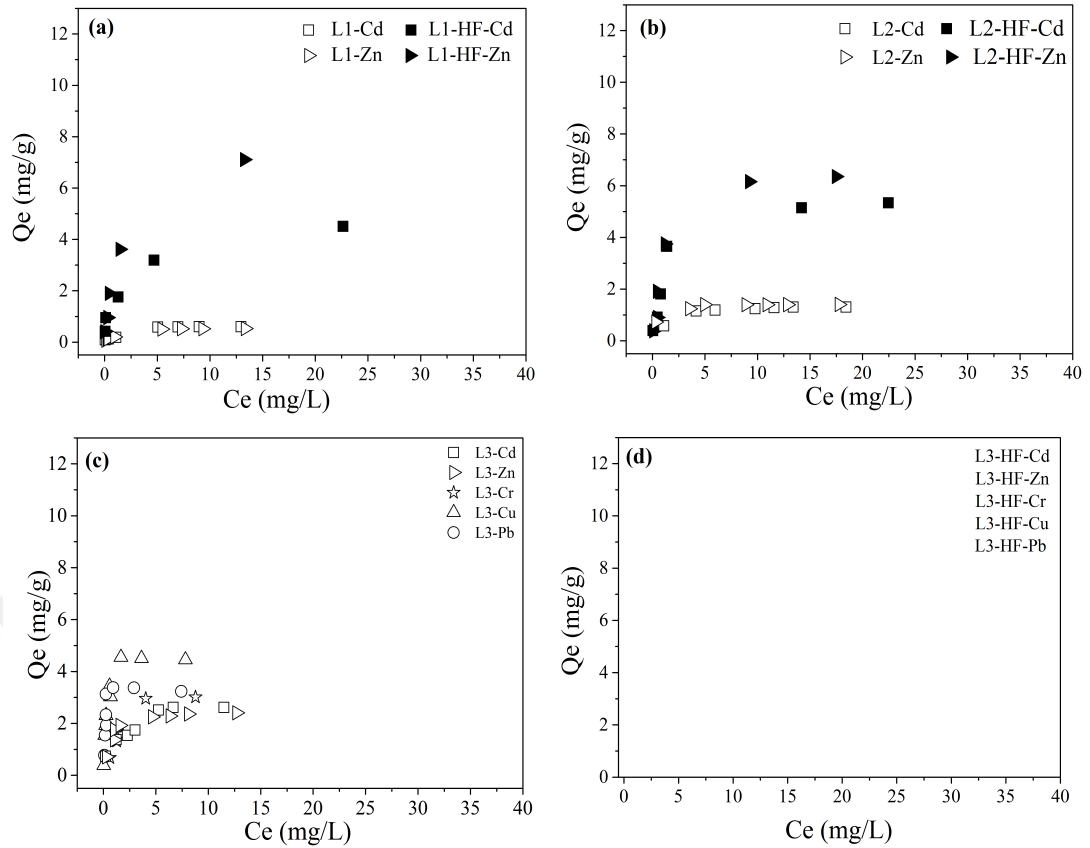


Figure 3.47 : Adsorption results for, **a)** L1 and L1HF **b)** L2 and L2HF (Cd(II), and Zn(II)), **c)** L3, **d)** L3HF samples (Cd(II), Zn(II), Cr(III), Pb(II), and Cu(II)).

The adsorption rates of the zeolite coated samples and their substrate are shown together in the same graph (Figure 3.48 (a and b)).

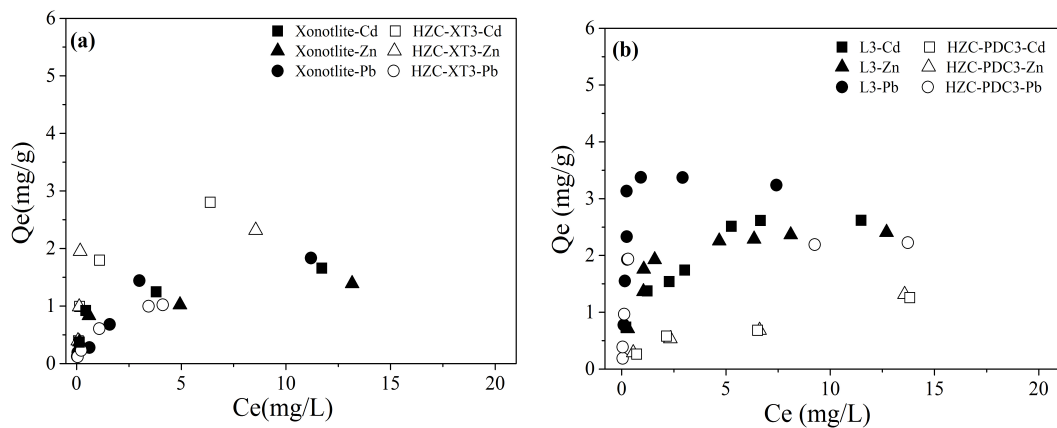


Figure 3.48 : Adsorption results of the sample **a)** HZC-XT-3 and xonotlite (commercial CSH) and **b)** HZC-PDC and its substrate L3

The results obtained for the HZC-XT3 which is the sample prepared by using this substrate with commercial Xonotlite in Fig. 3.48 (a). In Figure 3.48 (b), the results

are given for the HZC-PDC3 sample which was produced by zeolite coating of with a hierarchical and aligned porous SiOC sample (L3).

The results for the Alginate1 sample, which is also porous CSH monolith obtained from the synthesized CSH powders using XRG71, is given in Figure 3.49.

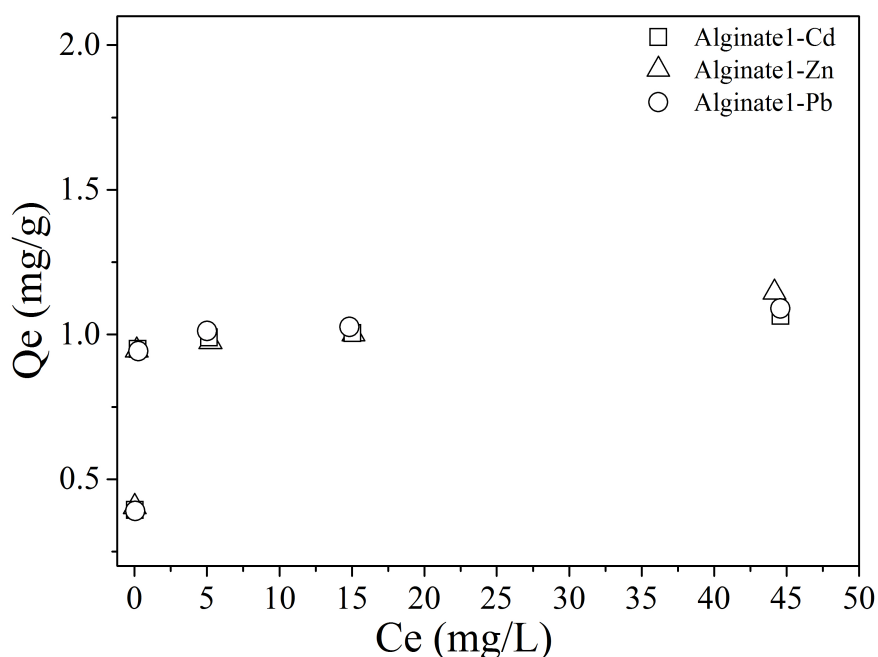


Figure 3.49 : Adsorption results for Alginate 1.

For the Cd(II), Zn(II), and Pb(II), the zeolite coated samples showed approximately 50% lower adsorption capacities than their substrates. This is most probably due to pore closure/narrowing.

The Langmuir isotherm model is more suitable than the Freundlich isotherm model considering the R^2 values.

Even though the metal adsorption values of the SiOC sample increased after the HF etching process, results were insufficient when compared with commercial adsorbents.

The results of all adsorption capacity determination experiments were fit by Langmuir and Freundlich isotherm and given in Table 3.13.

Table 3.12 : The results of Langmuir and Freundlich isotherms for all samples

Sample Code	Metal	Langmuir Isotherm			Freundlich Isotherm		
		q _m (mg/g)	K _L (L/mg)	R ²	n	K _f (mg/g)	R ²
L1	Zn(II)	0.57	1.06	0.994	3.74	0.29	0.629
	Cd(II)	0.62	2.83	0.994	2.55	0.28	0.983
L1HF	Zn(II)	7.78	0.77	0.983	2.28	2.43	0.941
	Cd(II)	3.81	1.32	0.996	2.86	1.61	0.928
L2	Zn(II)	1.43	2.97	0.999	4.14	0.93	0.970
	Cd(II)	1.39	1.01	0.998	6.24	0.69	0.592
L2HF	Zn(II)	7.06	0.58	0.985	1.90	1.91	0.832
	Cd(II)	5.65	0.74	0.994	2.32	1.75	0.873
L3	Zn(II)	2.54	1.49	0.996	3.75	1.38	0.779
	Cd(II)	2.67	1.66	0.972	2.84	1.30	0.965
	Pb(II)	3.42	6.31	0.983	5.00	1.67	0.109
	Cr(III)	4.04	0.39	0.958	1.43	1.03	0.948
	Cu(II)	4.54	5.45	0.995	3.02	1.75	0.802
L3HF	Zn(II)	14.84	0.27	0.933	1.24	2.71	0.973
	Cd(II)	5.59	1.44	0.991	2.69	2.16	0.717
	Pb(II)	5.59	3.39	0.999	2.86	2.50	0.874
	Cr(III)	3.73	0.11	0.959	1.85	0.49	0.845
	Cu(II)	7.17	1.20	0.906	2.49	3.56	0.685
Commercial CSH	Zn(II)	1.43	1.11	0.998	4.43	0.70	0.868
	Cd(II)	1.73	1.41	0.999	4.09	0.83	0.792
	Pb(II)	2.25	0.39	0.868	2.19	0.60	0.832
HZC-XT-3	Zn(II)	2.46	3.89	0.999	4.89	1.39	0.430
	Cd(II)	3.10	1.69	0.999	3.27	1.34	0.770
	Pb(II)	4.47	1.22	0.927	1.82	1.84	0.983
HZC-PDC-3	Zn(II)	1.43	0.27	0.978	2.69	0.38	0.906
	Cd(II)	1.39	0.27	0.984	2.57	0.35	0.866
	Pb(II)	2.26	4.30	0.999	3.05	9.60	0.589
Alginate1	Zn(II)	1.07	1.51	0.997	9.33	0.80	0.618
	Cd(II)	1.15	3.48	0.999	9.08	0.78	0.581
	Pb(II)	1.09	3.13	0.999	8.04	0.76	0.539

3.4.3 Industrial wastewater purification

All of the above-mentioned experiments were performed by aqueous solutions containing impurities deliberately added. The industrial wastewater contains many

different scale and variety of impurities and also suspended solids. This very complex matrix in real wastewater can lead to different interferences in the water purification process that are difficult to predict. For this reason, wastewater from the industrial wastewater treatment center was collected and subjected to batch adsorption tests with L3HF.

Table 3.15 shows that the results from the samples tested as described in the batch adsorption tests of the impurities studied.

Table 3.13 : Adsorption of pollutant tested onto L3HF from actual wastewater.

	Initial concent. (mg/L)	Final concent. (mg/L)	Adsorbed (mg/L)	Adsorbed (mg/g L3HF)	Adsorbed (%)
Zn	79.17	53.68	25.48	5.10	32.18
Cd	20.75	19.92	0.82	0.16	3.95
Pb	4.48	4.07	0.41	0.08	9.15
Cr	14.95	11.77	3.18	0.64	21.27
Cu	15.71	11.90	3.81	0.76	24.25
MB	50.00	11.34	38.66	77.32	77.32
CV	50.00	9.53	40.47	80.94	80.94
RB	50.00	13.18	36.82	73.64	73.64

Similarly, to the test results obtained from synthetic wastewater (which have only one pollutant added in it), we have observed the highest adsorption rate for Zn(II). One gram of L3HF sample removed more than 30% of the Zn(II) from the wastewater while this value was found around 20% for Cr(III) and Cu(II).

Similar to the results in aqueous solutions, dyes were better adsorbed than the metals and the samples showed adsorption capacity over 70% for each dye.

4. DISCUSSION

4.1 Silicon Oxy-Carbide Samples

The porosity of pyrolyzed SiOC samples were directly proportional to the PDMS amount in the pre-ceramic mixture. This can be explained by the formation of pores by complete decomposition of the PDMS polymer at about 400 °C [77]. The silica content was removed by HF etching of SiOC samples resulting the C-rich high surface area ceramics.

After zeolite coating of SiOC samples, certain regions were completely covered with zeolite crystals. In other areas, the coating was thin or not available at all. With the increase in the reaction time, the surface area showed slight reduction. This is probably due to pore blockings by the formed zeolite coating.

4.2 Calcium Silicate Samples

By using recycled glass, CSH powders were produced in high purity and different crystalline structures. Those products were used to manufacture monolithic CSH samples. The pore average size of the monolithic samples CSH/CS was found to be around 0.65 microns. This size is very limited for the nucleation and growth of zeolites. Micro-meso porosity was achieved by the heat treatment applied after the Zeolite coating reaction. According to the results, both average pore size and total pore volume of the samples decreased after the reactions. The zeolite coating treatment in these samples may then be considered as the reason for the decrease in the average pore size and the total pore content resulting in the formation of new zeolites resulting in closure in the existing pore inner walls.

4.3 Adsorption Studies

The maximum adsorption values of the etched SiOC sample increased by around six times. In SiOC ceramics, the etching increases the amount of Si-OH on the surface, and the resulting new silanol groups may bond with the metal or dye ions in aqueous solutions, which is probably the main reason for increased absorption for almost all

tested pollutants after etching. In addition, with the increase of surface area, the amount of active adsorption surface sites increased and all adsorption values increased as a result. The adsorption capacities of some commonly used adsorbents for metal ions are given in Table 4.1.

Table 4.1 : Comparison of samples produced and common adsorbent material studied in the literature.

Adsorbent	SSA (m ² /g)	Max. Adsorption Capacities (mg/g)					Ref.
		Cd (II)	Zn (II)	Cu (II)	Pb (II)	Cr (III)	
Activated Carbon	325	2.45	1.8	2.7	-	-	[38]
	566	33.6	-	24.1	22.9	29.5	[78]
	-	-	-	6.7	13.1	-	[79]
	1398	-	-	-	98.4	-	[80]
Carbon Aerogel	419	244.6	-	126.8	-	-	[81]
	426	400.8	1.8	561.7	0.8	-	[82]
	700	15.5	-	-	34.7	-	[83]
Clay	272	-	-	-	0.1	-	[33]
	-	-	-	30.7	62.1	-	[84]
	-	210.0	-	-	365.0	-	[85]
	-	44.8	80.6	-	-	-	[86]
	79	4.2	-	25.8	27.7	-	[87]
Zeolite	304-436	-	-	-	-	8.0-63.0	[34]
	-	-	133.9	141.1	-	-	[35]
Meso-porous Silica	550	14.6	-	-	-	-	[88]
	48-790	-	-	15.3-52.7	-	-	[89]
Cation exchange resin	-	101.1	5*104	3*103	84.1	-	[90]
Biosorbent	-	-	29.6	32.7	-	45.1	[91]
	-	-	-	-	75.8	52.1	[92]
	-	-	1.8-	-	-	-	[93]
	-	-	22.2	-	-	-	[94]
	-	-	9.6	7.6	-	-	[95]
	-	-	1.2	1.2	-	-	[96]
	-	-	25.7	35.8	25.1	-	[97]
	-	14.7	31.4	21.7	-	-	[98]
	-	-	-	25.4-50.3	-	27.9	[99, 100]
	CSH	-	1.2-3.1	1.1-2.5	-	1.1-2.3	-
SiOC	4-774	0.6-5.7	0.6-14.8	4.5-7.2	3.4-5.6	3.7-4.0	*

*Results collected from this study.

Adsorption of metal ions with porous materials is a highly complex process depending on various parameters such as pore structure, specific surface area, surface chemistry, surface charge, metal ion diameter and chemistry, etc.. Since these properties are not always analyzed well and given, comparison of the sorbents is difficult, and so there are anomalies and suspicious records in the literature [101]. In addition, the adsorption of metals by the samples produced is complex because the

samples produced are not pure and single-phase materials such as commercially available materials.

Hokura et al.[102] studied the absorption of Ni, Co, Cu and Zn using mesoporous silica which could be considered a material similar to the SiOC samples. The adsorption was achieved in the order of Ni <Co <Cu <Zn. They did not explain why Zinc was adsorbed much higher than other metals.

The maximum adsorption capacities of the CSH samples produced are insufficient for the remove both metal or dye ions when compared with the SiOC samples.

SiOC samples, especially HF etched ones are successful candidates for the removal of dyes from water. The adsorption capacities of some commonly used adsorbents for dyes are given in Table 4.2.

Table 4.2 : Comparison of samples produced and common adsorbent material studied in the literature.

Adsorbent	SSA (m ² /g)	Max. Adsorption Capacities (mg/g)			References
		MB	CV	RB	
	28-945	1.3-8.8	-	-	[103]
	180	594	-	-	[104]
Activated Carbon	328-556	-	60.4-885.8	-	[105]
	720	-	-	307.2	[106]
	1060	89	140	-	[107]
	1083	294.1	-	-	[108]
	1354	277.8	-	-	[109]
Carbon Aerogel	435	190.9	-	145.9	[110]
	62	300.3	-	-	[31]
Clay	30	58.2	-	-	[111]
	-	-	142.8-228.5	-	[112]
Meso-porous silica	659	49.3	-	-	[113]
	757	113	-	-	[114]
CSH	-	18.1-28.1	13.3-51.3	4.5-7.0	*
SiOC	4-774	15.7-104.3	49.5-185.9	49.5-110.7	[115]*

*Results from this study.

As could be seen in Table 4.2, very different results can be obtained in studies with activated carbon, one of the most commonly used adsorbent materials. The activated

carbon adsorbents were reported having SSA values ranging from 28 to 1335 m²/g [103, 104, 109], with a wide range of dye adsorption capacities from 1.3 to 886 mg/g [105, 106]. The ceramic system closest to the L series samples, SiOC with a surface area of 163 m²/g and SiC aerogel with 102 m²/g were produced by *Bruzzoniti et al.* [69]. These ceramic materials were treated with an aqueous solution of MB and RB dyes separately. SiOC aerogels adsorbed 44.2 mg MB per g material. In another study to investigate the RB adsorption from aqueous solution, *Yu et al.* [116] with 88 m²/g surface for mesoporous SiOC samples produced by a very difficult and non-economical process. These samples removed 90% of RB at very low concentrations from aqueous media, the adsorption capacity was not mentioned in the study.

Composite materials are also commonly used in removing dyes from aqueous media [117-119]. Pre-ceramic polymers and wood were combined to produce composites with a surface area of 463 m²/g by *Pan et al.* [68]. The MB adsorption capacity of this composite material was found 173.5 mg/g. It can be said that the dye adsorption capacities of SiOC samples showed consistent results with literature but CS/CSH produced are insufficient compared to similar type of adsorbents.

In experiments with dye mixtures, it was found that although the sample tested did not show selective adsorption for any specific dye, it simultaneously adsorbed all 3 dyes (Methylene blue, Crystal violet, and Rhodamine B) with a retention value of over 99% after 24 hours.

4.4 Regeneration

Regeneration experiments were tested by two different procedures. In the first system, it was tried to be removed the dyes from the loaded sample by chemical extraction. In the second system, thermal regeneration was applied to decompose the dyes. Thermal regeneration experiments resulted in a yield more than 99% even after the 3rd cycle of the adsorption-desorption process.

4.5 Industrial Wastewater

Industrial wastewater was obtained from the water treatment centre and tested with produced porous materials. Various contaminants are present in the actual wastewater. The results from this complex contaminated water are not comparable to

the tests that was conducted since there was only one pollutant. Nevertheless, the rate up to 80% was recorded in the adsorption of dyes, while the highest adsorption in metal ions was seen in 32% versus Zn ion, similar to previous experiments.



5. CONCLUSION AND RECOMMENDATIONS

The aim of this work was to produce porous ceramics in a practical and economical ways. The produced porous ceramics were tested to remove metal ions and dyes from wastewater simultaneously. For this purpose, the samples with macro pores were produced, then by acid etching or zeolite coating, the materials containing both macro and micro/meso porosity structure were formed. The structural properties of the materials produced were compared with the other adsorbents in the literature. Finally, water purification experiments were carried out with some of the selected samples.

The produced samples can be divided into two groups according to their manufacturing process; silicon-oxy-carbide samples and calcium-silicate samples. While pre-ceramic polymers are used to obtain SiOC, CSH samples are produced starting from recycled glass.

Batch adsorption technique was used to investigate the filtering efficiency of the tested samples.

Another important aspect of this work is to characterize the properties of the produced samples such as porosity, surface chemistry, and surface area can be altered according to applications. Since contaminated waters have a complex matrix, it is an important advantage that the materials produced can be used to simultaneously remove metal ions and dyes. The samples produced in this study can eliminate the lack of application in porous ceramics, especially in the field of water treatment for removing dyes.

The results obtained from this study can be improved to produce samples with a specific pore structure that will create selective affinity for certain pollutants. Selective adsorption can be important factor for filtering of industrial wastewater.

A practical and economical prototype filter can also be developed with these adsorbent materials. In addition, these materials can be used in other applications such as space and biotechnology by controlling their structural and chemical properties.



REFERENCES

- [1] Liu, J., Dorjderem, A., Fu, J., Lei, X. and Macer, D. (2011). *Water Ethics and Water Resource Management*. UNESCO Bangkok Asia.
- [2] Zorba, S. *Half the World to Face Severe Water Stress by 2030 unless Water Use is "Decoupled" from Economic Growth*, International Resource Panel. (2018) United Nations Environment Programme. Retrieved May 15, 2018, from <https://www.unenvironment.org/news-and-stories/press-release/half-world-face-severe-water-stress-2030-unless-water-use-decoupled>
- [3] Kumar, M. and Puri, A. (2012). A review of permissible limits of drinking water, *Indian Journal of Occupational and Environmental Medicine*, 16(1), 40.
- [4] Tchounwou, P.B., Yedjou, C.G., Patlolla, A.K. and Sutton, D.J. (2012). Heavy metal toxicity and the environment. *Molecular, Clinical and Environmental Toxicology* (Vol. 1 pp.133-164). Basel : Springer.
- [5] Hayes, R.B., (1997). The carcinogenicity of metals in humans, *Cancer Causes & Control*, 8(3), 371-385.
- [6] Oyaró, N., Juddy, O., Murago, E.N. and Gitonga, E. (2007). The contents of Pb, Cu, Zn and Cd in meat in Nairobi, *Journal of Food, Agriculture & Environment*, 5(3), 119-121.
- [7] Lanphear, B.P., Matte, T.D., Rogers, J., Clickner, R.P., Dietz, B., Bornschein, R.L., Succop, P., Mahaffey, K.R, Dixon, S. and Galke, W. (1998). The contribution of lead-contaminated house dust and residential soil to children's blood lead levels: a pooled analysis of 12 epidemiologic studies, *Environmental Research*, 79(1), 51-68.
- [8] Patrick, L., (2006). Lead Toxicity, a review of the literature. Part I: Exposure, Evaluation, and treatment, *Alternative Medicine Review*, 11(1).
- [9] Crini, G., (2006). Non-conventional low-cost adsorbents for dye removal: A review, *Bioresource Technology*, 97(9), 1061-1085.
- [10] Alyüz, B. and Veli, S. (2009). Kinetics and equilibrium studies for the removal of nickel and zinc from aqueous solutions by ion exchange resins, *Journal of Hazardous Materials*, 167(1), 482-488.
- [11] Huang, H., Zhang, J., Jiang, L. and Zang, Z. (2017). Preparation of cubic Cu₂O nanoparticles wrapped by reduced graphene oxide for the efficient removal of rhodamine B, *Journal of Alloys and Compounds*, 718, 112-115.
- [12] Hojamberdiev, M., Prasad, R.M., Morita, K., Schiavon, M.A. and Riedel, R. (2012). Polymer-derived mesoporous SiOC/ZnO nanocomposite

for the purification of water contaminated with organic dyes, *Microporous and Mesoporous Materials*, 151, 330-338.

- [13] **Chen, Q., Luo, Z., Hills, C., Xue, G. and Tyrer, M.** (2009). Precipitation of heavy metals from waste water using simulated flue gas: Sequent additions of fly ash, lime and carbon dioxide, *Water Research*, 43(10), 2605-2614.
- [14] **Ahmad, A.L. and Ooi, B.S.** (2010). A study on acid reclamation and copper recovery using low pressure nanofiltration membrane, *Chemical Engineering Journal*, 156(2), 257-263.
- [15] **Baysal, A., Ozbek, N. and Akman, S.** (2013). *Determination of Trace Metals in Waste Water and Their Removal Processes*, Waste Water - Treatment Technologies and Recent Analytical Developments.
- [16] **Charerntanyarak, L.**, (1999). Heavy metals removal by chemical coagulation and precipitation, *Water Science and Technology*, 39(10), 135-138.
- [17] **Barakat, M.A. and Schmidt, E.** (2010). Polymer-enhanced ultrafiltration process for heavy metals removal from industrial wastewater, *Desalination*, 256(1), 90-93.
- [18] **Emamjomeh, M.M. and Sivakumar, M.** (2009). Review of pollutants removed by electrocoagulation and electrocoagulation/flotation processes, *Journal of Environmental Management*, 90(5), 1663-1679.
- [19] **Fu, F. and Wang, Q.** (2011). Removal of heavy metal ions from wastewaters: A review, *Journal of Environmental Management*, 92(3), 407-418.
- [20] **Sudilovskiy, P.S., Kagramanov, G.G. and Kolesnikov, V.A.** (2008). Use of RO and NF for treatment of copper containing wastewaters in combination with flotation, *Desalination*, 221(1), 192-201.
- [21] **Grassi, M., Kaykioglu, G., V. Belgiorno, V. and Lofrano, G.** (2012). Removal of emerging contaminants from water and wastewater by adsorption process. *Emerging compounds removal from wastewater*. Springer. 15-37.
- [22] **Gupta, V.K., Kumar, R., Nayak, A., Saleh, T.A. and Barakat, M.A.** (2013). Adsorptive removal of dyes from aqueous solution onto carbon nanotubes: A review, *Advances in Colloid and Interface Science*, 193-194.
- [23] **Gupta, V.K. and Suhas**, (2009). Application of low-cost adsorbents for dye removal – A review, *Journal of Environmental Management*, 90(8), 2313-2342.
- [24] **Wan Ngah, W.S., Teong, L.C. and Hanafiah, M.A.K.M.** (2011). Adsorption of dyes and heavy metal ions by chitosan composites: A review, *Carbohydrate Polymers*, 83(4), 1446-1456.
- [25] **Ali, I. and Gupta, V.** (2006). Advances in water treatment by adsorption technology, *Nature Protocols*, 1(6), 2661.
- [26] **Sawyer, C. and McCarty, P.** (1978). *Chemistry for environmental engineers*, New York, Mc Graw-Hill Book Company.

- [27] **Dąbrowski, A.**, (2001). Adsorption from theory to practice, *Advances in Colloid and Interface Science*, 93(1), 135-224.
- [28] **Chen, J.-C., Wey, M.-Y. and Liu, Z.-S.** (2001). Adsorption mechanism of heavy metals on sorbents during incineration, *Journal of Environmental Engineering*, 127(1), 63-69.
- [29] **Burakov, A.E., Galunin, E.V., Burakova, I.V., Kucherova, A.E., Agarwal, S., Tkachev, A.G. and Gupta, V.K.** (2018). Adsorption of heavy metals on conventional and nanostructured materials for wastewater treatment purposes: A review, *Ecotoxicology and Environmental Safety*, 148, 702-712.
- [30] **Wu, Y., Chen, L., Long, X., Zhang, X., Pan, B. and Qian, J.** (2018). Multi-functional magnetic water purifier for disinfection and removal of dyes and metal ions with superior reusability, *Journal of Hazardous Materials*, 347, 160-167.
- [31] **Almeida, C., Debacher, N., Downs, A., Cottet, L. and Mello, C.** (2009). Removal of methylene blue from colored effluents by adsorption on montmorillonite clay, *Journal of Colloid and Interface Science*, 332(1), 46-53.
- [32] **Boonamnuayvitaya, V., Chaiya, C., Tanthapanichakoon, W. and Jarudilokkul, S.** (2004). Removal of heavy metals by adsorbent prepared from pyrolyzed coffee residues and clay, *Separation and Purification Technology*, 35(1), 11-22.
- [33] **Celis, R., Hermosin, M.C. and Cornejo, J.** (2000). Heavy metal adsorption by functionalized clays, *Environmental Science & Technology*, 34(21), 4593-4599.
- [34] **Covarrubias, C., García, R., Arriagada, R., Yáñez, J. and Garland, M.T.** (2006). Cr(III) exchange on zeolites obtained from kaolin and natural mordenite, *Microporous and Mesoporous Materials*, 88(1-3), 220-231.
- [35] **Erdem, E., Karapinar, N. and Donat, R.** (2004). The removal of heavy metal cations by natural zeolites, *Journal of Colloid and Interface Science*, 280(2), 309-314.
- [36] **Pehlivan, E., Cetin, S. and Yanık, B.** (2006). Equilibrium studies for the sorption of zinc and copper from aqueous solutions using sugar beet pulp and fly ash, *Journal of Hazardous Materials*, 135(1-3), 193-199.
- [37] **Mohan, D. and Singh, K.P.** (2002). Single- and multi-component adsorption of cadmium and zinc using activated carbon derived from bagasse—an agricultural waste, *Water Research*, 36(9), 2304-2318.
- [38] **Üçer, A., Uyanık, A. and Aygün, Ş.** (2006). Adsorption of Cu (II), Cd (II), Zn (II), Mn (II) and Fe (III) ions by tannic acid immobilised activated carbon, *Separation and Purification Technology*, 47(3), 113-118.
- [39] **Zhang, S., Shao, T., Karanfil, T. and Pan, B.** (2012). The correlation between structural characteristics of activated carbons and their adsorption of organic solutes from aqueous solutions, *Adsorption*, 18(3-4), 229-238.

- [40] **Qu, J.**, (2008). Research progress of novel adsorption processes in water purification: A review, *Journal of Environmental Sciences*, 20(1), 1-13.
- [41] **Gonzalez-Serrano, E., Cordero, T., Rodriguez-Mirasol, J., Cotoruelo, L. and Rodriguez, J.J.** (2004). Removal of water pollutants with activated carbons prepared from H₃PO₄ activation of lignin from kraft black liquors, *Water Research*, 38(13), 3043-3050.
- [42] **Sekar, M., Sakthi, V. and Rengaraj, S.** (2004). Kinetics and equilibrium adsorption study of lead (II) onto activated carbon prepared from coconut shell, *Journal of Colloid and Interface Science*, 279(2), 307-313.
- [43] **Laine, J. and Yunes, S.** (1992). Effect of the preparation method on the pore size distribution of activated carbon from coconut shell, *Carbon*, 30(4), 601-604.
- [44] **El Nemr, A., Khaled, A., Abdelwahab, O. and El-Sikaily, A.** (2008). Treatment of wastewater containing toxic chromium using new activated carbon developed from date palm seed, *Journal of Hazardous Materials*, 152(1), 263-275.
- [45] **Thinakaran, N., Baskaralingam, P., Pulikesi, M., Panneerselvam, P. and Sivanesan, S.** (2008). Removal of Acid Violet 17 from aqueous solutions by adsorption onto activated carbon prepared from sunflower seed hull, *Journal of Hazardous Materials*, 151(2-3), 316-322.
- [46] **Sahu, J., Acharya, J. and Meikap, B.** (2009). Response surface modeling and optimization of chromium (VI) removal from aqueous solution using Tamarind wood activated carbon in batch process, *Journal of Hazardous Materials*, 172(2-3), 818-825.
- [47] **Acharya, J., Sahu, J., Mohanty, C. and Meikap, B.** (2009). Removal of lead (II) from wastewater by activated carbon developed from Tamarind wood by zinc chloride activation, *Chemical Engineering Journal*, 149(1-3), 249-262.
- [48] **Yeon, S.-H., Reddington, P., Gogotsi, Y., Fischer, J.E., Vakifahmetoglu, C. and Colombo, P.** (2010). Carbide-derived-carbons with hierarchical porosity from a preceramic polymer, *Carbon*, 48(1), 201-210.
- [49] **Vakifahmetoglu, C., Presser, V., Yeon, S.-H., Colombo, P. and Gogotsi, Y.** (2011). Enhanced hydrogen and methane gas storage of silicon oxycarbide derived carbon, *Microporous and Mesoporous Materials*, 144(1-3), 105-112.
- [50] **Oschatz, M., Borchardt, L., Thommes, M., Cychosz, K.A., Senkowska, I., Klein, N., Frind, R., Leistner, M., Presser, V., Gogotsi, Y. and Kaskel, S.** (2012). Carbide-Derived Carbon Monoliths with Hierarchical Pore Architectures, *Angewandte Chemie International Edition*, 51(30), 7577-7580.

- [51] **Sepulveda, P. and Binner, J.G.** (1999). Processing of cellular ceramics by foaming and in situ polymerisation of organic monomers, *Journal of European Ceramic Society*, 19, 2059-2066.
- [52] **Colombo, P., and Hellmann, J.** (2002). Ceramic foams from preceramic polymers, *Materials Research Innovations*, 6(5), 260-272.
- [53] **Studart, A.R., Gonzenbach, U.T., Tervoort, E. and Gauckler, L.J.** (2006). Processing Routes to Macroporous Ceramics: A Review, *Journal of the American Ceramic Society*, 89(6), 1771-1789.
- [54] **Kim, Y.-W., Jin, Y.-J., Eom, J.-H., Song, I.-H. and Kim, H.-D.** (2010). Engineering porosity in silicon carbide ceramics, *Journal of Materials Science*, 45, 2808-2815.
- [55] **Vakifahmetoglu, C., Pippel, E., Woltersdorf, J. and Colombo, P.** (2010). Growth of 1D-Nanostructures in Porous Polymer Derived Ceramics by Catalyst-Assisted-Pyrolysis. Part I: Iron Catalyst, *Journal of the American Ceramic Society*, 93(4), 959-968.
- [56] **Vakifahmetoglu, C., Colombo, P., Carturan, S., Pippel, E. and Woltersdorf, J.** (2010). Growth of 1D-Nanostructures in Porous Polymer Derived Ceramics by Catalyst-Assisted-Pyrolysis. Part II: Cobalt Catalyst, *Journal of the American Ceramic Society*, 93(11), 3709-3719.
- [57] **Yang, Y., Guo, Q., X. He, X., J. Shi, J., L. Liu, L. and Zhai, G.** (2010). Effect of nano-AlN content on the microstructure and mechanical properties of SiC foam prepared by siliconization of carbon foam, *Journal of European Ceramic Society*, 30, 113-118.
- [58] **Shoumkova, A.** (2011). Zeolites for water and wastewater treatment: An overview, *Research Bulletin of the Australian Institute of High Energetic Materials. Special Issue on Global Fresh Water Shortage 2*, 10-70.
- [59] **Mori, H., Aotani, K., Sano, N. and Tamon, H.** (2011). Synthesis of a hierarchically micro-macroporous structured zeolite monolith by ice-templating, *Journal of Materials Chemistry*, 21(15), 5677-5681.
- [60] **Kuwahara, Y., Tamagawa, S., Fujitani, T. and Yamashita, H.** (2013). A novel conversion process for waste slag: synthesis of calcium silicate hydrate from blast furnace slag and its application as a versatile adsorbent for water purification, *Journal of Materials Chemistry A*, 1(24), 7199-7210.
- [61] **Sharma, Y.C., Uma, J., Srivastava, V., Srivastava, J. and Mahto, M.** (2007). Reclamation of Cr(VI) rich water and wastewater by wollastonite, *Chemical Engineering Journal*, 127(1), 151-156.
- [62] **Muthutantri, A., Huang, J. and Edirisinghe, M.** (2008). Novel preparation of graded porous structures for medical engineering, *Journal of Royal Society Interface*, 5(29), 1459-1467.
- [63] **Vakifahmetoglu, C. and Colombo, P.** (2008). A Direct Method for the Fabrication of Macro-Porous SiOC Ceramics from Preceramic Polymers, *Advanced Engineering Materials*, 10(3), 256-259.

- [64] **Vakifahmetoglu, C., Colombo, P., Pauletti, A., Martin, C.F. and Babonneau, F.** (2009). SiOC Ceramic Monoliths with Hierarchical Porosity, *International Journal of Applied Ceramic Technology*, (7), 528-535.
- [65] **Blum, Y., Sorarù, G.D., Ramaswamy, A.P., Hui, D. and Carturan, S.M.** (2013). Controlled Mesoporosity in SiOC via Chemically Bonded Polymeric “Spacers”, *Journal of the American Ceramic Society*, 96(9), 2785-2792.
- [66] **Tolosa, A., Krüner, B., Jackel, N., Aslan, M., Vakifahmetoglu, C. and Presser, V.** (2016). Electrospinning and electrospraying of silicon oxycarbide-derived nanoporous carbon for supercapacitor electrodes, *Journal of Power Sources*, 313, 178-188.
- [67] **Presser, V., Yeon, S.-H., Vakifahmetoglu, C., Howell, C.A., Sandeman, S.R., Colombo, P., Mikhailovsky, S. and Gogotsi, Y.** (2012). Hierarchical Porous Carbide-Derived Carbons for the Removal of Cytokines from Blood Plasma, *Advanced Healthcare Materials*, 1(6), 796-800.
- [68] **Pan, J., Ren, J., Xie, Y., Wei, X., Guan, Y., Yan, X., Tang, H. and Cheng, X.** (2017). Porous SiOC composites fabricated from preceramic polymers and wood powders for efficient dye adsorption and removal, *Research on Chemical Intermediates*, 43(7), 3813-3832.
- [69] **Bruzzoniti, M.C., Appendini, M., Rivoira, L., Onida, B., Bubba, M. Del, Jana, P. and Sorarù, G.D.** (2018). Polymer-derived ceramic aerogels as sorbent materials for the removal of organic dyes from aqueous solutions, *Journal of the American Ceramic Society*, 101(2), 821-830.
- [70] **Barg, S., de Moraes, E.G., Koch, D. and Grathwohl G.** (2009). New cellular ceramics from high alkane phase emulsified suspensions (HAPES), *Journal of the American Ceramic Society*, 29, 2439-2446.
- [71] **Foo, K.Y. and Hameed, B.H.** (2010). Insights into the modeling of adsorption isotherm systems, *Chemical Engineering Journal*, 156(1), 2-10.
- [72] **Url-1.** <<https://pubchem.ncbi.nlm.nih.gov/>>, date retrieved 01.02.2019.
- [73] **Vakifahmetoglu, C., Buldu, M., Karakuscu, A., Ponzoni, A., Assefa, D. and Soraru, G.D.** (2015). High surface area carbonous components from emulsion derived SiOC and their gas sensing behavior, *Journal of the European Ceramic Society*, 35(16), 4447-4452.
- [74] **Assefa, D., Zera, E., Campostrini, R., Soraru, G.D. and Vakifahmetoglu, C.** (2016). Polymer-derived SiOC aerogel with hierarchical porosity through HF etching, *Ceramics International*, 42(10), 11805-11809.
- [75] **Mohammadi, M., Hassani, A.J., Mohamed, A.R. and Najafpour, G.D.** (2010). Removal of rhodamine B from aqueous solution using palm shell-based activated carbon: adsorption and kinetic studies, *Journal of Chemical & Engineering Data*, 55(12), 5777-5785.

- [76] **Monash, P. and Pugazhenth, G.** (2009). Adsorption of crystal violet dye from aqueous solution using mesoporous materials synthesized at room temperature, *Adsorption*, 15(4), 390-405.
- [77] **Vakifahmetoglu, C. and Colombo, P.** (2008). A Direct Method for the Fabrication of Macro-Porous SiOC Ceramics from Pre-ceramic Polymers, *Advanced Engineering Materials*, 10(3), 256-259.
- [78] **Koby, M., Demirbas, E., Senturk, E. and Ince, M.** (2005). Adsorption of heavy metal ions from aqueous solutions by activated carbon prepared from apricot stone, *Bioresource Technology*, 96(13), 1518-1521.
- [79] **Imamoglu, M. and Tekir, O.** (2008). Removal of copper (II) and lead (II) ions from aqueous solutions by adsorption on activated carbon from a new precursor hazelnut husks, *Desalination*, 228(1), 108-113.
- [80] **Wang, L., Zhang, J., Zhao, R., Li, Y., Li, C. and Zhang, C.** (2010). Adsorption of Pb(II) on activated carbon prepared from *Polygonum orientale* Linn.: Kinetics, isotherms, pH, and ionic strength studies, *Bioresource Technology*, 101(15), 5808-5814.
- [81] **Deze, E.G., Papageorgiou, S.K., Favvas, E.P. and Katsaros, F.K.** (2012). Porous alginate aerogel beads for effective and rapid heavy metal sorption from aqueous solutions: Effect of porosity in Cu²⁺ and Cd²⁺ ion sorption, *Chemical Engineering Journal*, 209, 537-546.
- [82] **Meena, A.K., Mishra, G.K., Rai, P.K., Rajagopal, C. and Nagar, P.N.** (2005). Removal of heavy metal ions from aqueous solutions using carbon aerogel as an adsorbent, *Journal of Hazardous Materials*, 122(1), 161-170.
- [83] **Aygün, A., Yenisoay-Karakaş, S. and Duman, I.** (2003). Production of granular activated carbon from fruit stones and nutshells and evaluation of their physical, chemical and adsorption properties, *Microporous and Mesoporous Materials*, 66(2), 189-195.
- [84] **Potgieter, J.H., Potgieter-Vermaak, S.S. and Kalibantonga, P.D.** (2006). Heavy metals removal from solution by palygorskite clay, *Minerals Engineering*, 19(5), 463-470.
- [85] **Lagadic, I.L., Mitchell, M.K. and Payne, B.D.** (2001). Highly Effective Adsorption of Heavy Metal Ions by a Thiol-Functionalized Magnesium Phyllosilicate Clay, *Environmental Science & Technology*, 35(5), 984-990.
- [86] **Veli, S. and Alyüz, B.** (2007). Adsorption of copper and zinc from aqueous solutions by using natural clay, *Journal of Hazardous Materials*, 149(1), 226-233.
- [87] **Sprynskyy, M., Buszewski, B., Terzyk, A.P. and Namieśnik, J.** (2006). Study of the selection mechanism of heavy metal (Pb²⁺, Cu²⁺, Ni²⁺, and Cd²⁺) adsorption on clinoptilolite, *Journal of Colloid and Interface Science*, 304(1), 21-28.
- [88] **Machida, M., Fotoohi, B., Y. Amamo, Y., Ohba, T., Kanoh, H. and Mercier, L.** (2012). Cadmium (II) adsorption using functional mesoporous

silica and activated carbon, *Journal of Hazardous Materials*, 221, 220-227.

- [89] **Aguado, J., Arsuaga, J.M., Arencibia, A., Lindo, M. and Gascón, V.** (2009). Aqueous heavy metals removal by adsorption on amine-functionalized mesoporous silica, *Journal of Hazardous Materials*, 163(1), 213-221.
- [90] **Demirbas, A., Pehlivan, E., Gode, F., Altun, T. and Arslan, G.** (2005). Adsorption of Cu(II), Zn(II), Ni(II), Pb(II), and Cd(II) from aqueous solution on Amberlite IR-120 synthetic resin, *Journal of Colloid and Interface Science*, 282(1), 20-25.
- [91] **Nasernejad, B., Zadeh, T.E., Pour, B.B., Bygi, M.E. and Zamani, A.** (2005). Comparison for biosorption modeling of heavy metals (Cr (III), Cu (II), Zn (II)) adsorption from wastewater by carrot residues, *Process Biochemistry*, 40(3), 1319-1322.
- [92] **Uluozlu, O.D., Sari, A.M., Tuzen, M. and Soylak, M.** (2008). Biosorption of Pb(II) and Cr(III) from aqueous solution by lichen (*Parmelina tiliaceae*) biomass, *Bioresource Technology*, 99(8), 2972-2980.
- [93] **Shukla, S.R., Pai, R.S. and Shendarkar, A.D.** (2006). Adsorption of Ni(II), Zn(II) and Fe(II) on modified coir fibres, *Separation and Purification Technology*, 47(3), 141-147.
- [94] **Chubar, N., Carvalho, J.R. and Correia, M.J.N.** (2003). Cork biomass as biosorbent for Cu(II), Zn(II) and Ni(II), *Colloids and Surfaces A: Physicochemical and Engineering Aspects*, 230(1), 57-65.
- [95] **Shukla, S.R. and Pai, R.S.** (2005). Adsorption of Cu(II), Ni(II) and Zn(II) on dye loaded groundnut shells and sawdust, *Separation and Purification Technology*, 43(1), 1-8.
- [96] **Manios, T., Stentiford, E. and Millner, P.** (2003). Removal of heavy metals from a metaliferous water solution by *Typha latifolia* plants and sewage sludge compost, *Chemosphere*, 53(5), 487-494.
- [97] **Amer, M.W., Ahmad, R.A. and Awwad, A.M.** (2015). Biosorption of Cu(II), Ni(II), Zn(II) and Pb(II) ions from aqueous solution by *Sophora japonica* pods powder, *International Journal of Industrial Chemistry*, 6(1), 67-75.
- [98] **Farhan, A.M., Salem, N.M., Ahmad, A.L. and A.M. Awwad,** (2012). Kinetic, equilibrium and thermodynamic studies of the biosorption of heavy metals by *Ceratonia siliqua* bark, *American Journal of Chemistry*, 2(6), 335-342.
- [99] **Feng, N., Guo, X.Y. and Liang, S.** (2010). Enhanced Cu(II) adsorption by orange peel modified with sodium hydroxide, *Transactions of Nonferrous Metals Society of China*, 20, 146-152.
- [100] **Witek-Krowiak, A., Szafran, R.G. and Modelski, S.** (2011). Biosorption of heavy metals from aqueous solutions onto peanut shell as a low-cost biosorbent, *Desalination*, 265(1), 126-134.
- [101] **Bailey, S.E., Olin, T.J., Bricka, R.M. and Adrian, D.D.** (1999). A review of potentially low-cost sorbents for heavy metals, *Water Research*, 33(11), 2469-2479.

- [102] **Hokura, A., Nakai, I., Yamada, H., O'CONNOR, A.J., Perera, J.M., Stevens, G.W. and Komatsu, Y.** (2003). Primary study on capturing behavior for transition metal ions on mesoporous silicate (MCM-41), *Journal of Ion Exchange*, 14(Supplement), 173-176.
- [103] **Girgis, B.S. and El-Hendawy, A.-N.A.** (2002). Porosity development in activated carbons obtained from date pits under chemical activation with phosphoric acid, *Microporous and Mesoporous Materials*, 52(2), 105-117.
- [104] **Girgis, B.S., Smith, E., Louis, M.M. and El-Hendawy, A.-N.A.** (2009). Pilot production of activated carbon from cotton stalks using H₃PO₄, *Journal of Analytical and Applied Pyrolysis*, 86(1), 180-184.
- [105] **Senthilkumaar, S., Kalaamani, P. and Subburaam, C.** (2006). Liquid phase adsorption of crystal violet onto activated carbons derived from male flowers of coconut tree, *Journal of Hazardous Materials*, 136(3), 800-808.
- [106] **Li, L., Liu, S. and Zhu, T.** (2010). Application of activated carbon derived from scrap tires for adsorption of Rhodamine B, *Journal of Environmental Sciences(China)*, 22(8), 1273-1280.
- [107] **Başar, C.A.**, (2006). Applicability of the various adsorption models of three dyes adsorption onto activated carbon prepared waste apricot, *Journal of Hazardous Materials*, 135(1), 232-241.
- [108] **Hameed, B.H., Ahmad, A.L. and Latiff, K.N.A.** (2007). Adsorption of basic dye (methylene blue) onto activated carbon prepared from rattan sawdust, *Dyes and Pigments*, 75(1), 143-149.
- [109] **Tan, I.A.W., Hameed, B.H. and Ahmad, A.L.** (2007). Equilibrium and kinetic studies on basic dye adsorption by oil palm fibre activated carbon, *Chemical Engineering Journal*, 127(1), 111-119.
- [110] **Sui, Z., Meng, Q., Zhang, X., Ma, R. and Cao, B.** (2012). Green synthesis of carbon nanotube–graphene hybrid aerogels and their use as versatile agents for water purification, *Journal of Materials Chemistry*, 22(18), 8767-8771.
- [111] **Gürses, A., Doğar, Ç., Yalçın, M., Açıkyıldız, M., Bayrak, R. and Karaca, S.** (2006). The adsorption kinetics of the cationic dye, methylene blue, onto clay, *Journal of Hazardous Materials*, 131(1), 217-228.
- [112] **Eren, E. and Afsin, B.** (2008). Investigation of a basic dye adsorption from aqueous solution onto raw and pre-treated bentonite surfaces, *Dyes and Pigments*, 76(1), 220-225.
- [113] **Huang, C.-H., Chang, K.-P., Ou, H.-D., Chiang, Y.-C. and Wang, C.F.** (2011). Adsorption of cationic dyes onto mesoporous silica, *Microporous and Mesoporous Materials*, 141(1), 102-109.
- [114] **Ho, K.Y., McKay, G. and Yeung, K.L.** (2003). Selective adsorbents from ordered mesoporous silica, *Langmuir*, 19(7), 3019-3024.
- [115] **Zeydanli, D., Akman, S. and Vakifahmetoglu, C.** (2018). Polymer-derived ceramic adsorbent for pollutant removal from water, *Journal of the American Ceramic Society*, 101(6), 2258-2265.

- [116] **Yu, Z., Feng, Y., Li, S. and Pei, Y.** (2016). Influence of the polymer–polymer miscibility on the formation of mesoporous SiC(O) ceramics for highly efficient adsorption of organic dyes, *Journal of the European Ceramic Society*, 36(15), 3627-3635.
- [117] **Li, Y., Du, Q., Liu, T., Sun, J., Wang, Y., Wu, S., Wang, Z., Xia, Y. and Xia, L.** (2013). Methylene blue adsorption on graphene oxide/calcium alginate composites, *Carbohydrate Polymers*, 95(1), 501-507.
- [118] **Auta, M. and Hameed, B.** (2014). Chitosan–clay composite as highly effective and low-cost adsorbent for batch and fixed-bed adsorption of methylene blue, *Chemical Engineering Journal*, 237, 352-361.
- [119] **Vilar, V.J., Botelho, C.M. and Boaventura, R.A.** (2007). Methylene blue adsorption by algal biomass based materials: biosorbents characterization and process behaviour, *Journal of Hazardous Materials*, 147(1-2), 120-132.

CURRICULUM VITAE

Name Surname : Damla ZEYDANLI
Place and Date of Birth : Istanbul/1985
E-Mail : damlazeydanli@gmail.com

EDUCATION

- **B.Sc.** : 2010, Kocaeli University, Chemistry
- **M.Sc.** : 2013, Istanbul Technical University, Chemistry

PROFESSIONAL EXPERIENCES:

- 2015-2018- TUBITAK, Research Assistant
- 2009-2010- Kocaeli University, Internship
- 2009- Middle East Technical University, Internship

PUBLICATIONS AND PRESENTATIONS ON THE THESIS:

- **Zeydanli D.,** Vakifahmetoglu, C.. 2018 : SiOC Ceramics for Water Purification, 19th International Metallurgy and Materials Congress October 25-27, 2018 Istanbul, Turkey.
- **Zeydanli D.,** Akman S., Vakifahmetoglu, C.. 2018. Polymer-derived ceramic adsorbent for pollutant removal from water, *Journal of the American Ceramic Society*, 101 (6), 2258-2265.

OTHER PUBLICATIONS AND PRESENTATIONS:

- Vakifahmetoglu C., **Zeydanli D.**, Innocentini M. D. d. M., Ribeiro F. d. S., Lasso P. R. O. and Soraru G. D.. 2017. Gradient-Hierarchic-Aligned Porosity SiOC Ceramics, *Scientific Reports*, 7, 41049
- Vakifahmetoglu C., **Zeydanli D.**, Ozalp V. C., Borsa B. A., and Soraru G. D. 2018. Hierarchically porous polymer derived ceramics: A promising platform for multidrug delivery systems, *Materials & Design*, 140, 37-44.
- Vakifahmetoglu, C., **Zeydanli D.**, Colombo P.. 2016. Porous polymer derived ceramic, *Materials Science and Engineering R: Reports*, 106, 1-30.
- Destanoglu O., **Zeydanli D.**, Cansever M. Ş., Yılmaz G. G.. P.. 2018. Ion chromatographic method for determination of orotic acid in urine. *Analytical Biochemistry*, 563, 9-14.
- **Zeydanli D.**, Destanoglu O., Yılmaz G. G.. 2012. Ion chromatographic determination of orotic acid in urine samples after elimination of matrix effects, 29th International Symposium on Chromatography, Poland, September 9-13 2012.